Modeling and Numerical Studies of Laser-Based Terahertz Generation

Dissertation
zur Erlangung des Doktorgrades
an der Fakultät für Mathematik, Informatik und
Naturwissenschaften
Fachbereich Physik
der Universität Hamburg

vorgelegt von

Lu Wang

Hamburg
2019

Gutachter/innen der Dissertation:	Prof. Franz Kärtner Dr. Arya Fallahi
Zusammensetzung der Prüfungskommission:	Prof. Franz Kärtner Dr. Arya Fallahi Prof. Robin Santra Dr. Steve Aplin Prof. Daniela Pfannkuche
Vorsitzende/r der Prüfungskommission:	Prof. Robin Santra
Datum der Disputation:	21.02.2020
Vorsitzender Fach-Promotionsausschusses PHYSIK:	Prof. Dr. Günter Hans Walter Sigl
Leiter des Fachbereichs PHYSIK:	Prof. Dr. Wolfgang Hansen
Dekan der Fakultät MIN:	Prof. Dr. Heinrich Graener

Eidesstattliche Versicherung

Hiermit versichere ich an Eides statt, dass ich die vorliegende Arbeit im Studiengang Physik selbstständig verfasst und keine anderen als die angegebenen Hilfsmittel – insbesondere keine im Quellenverzeichnis nicht benannten Internet-Quellen – benutzt habe. Alle Stellen, die wörtlich oder sinngemäß aus Veröffentlichungen entnommen wurden, sind als solche kenntlich gemacht. Ich versichere weiterhin, dass ich die Arbeit vorher nicht in einem anderen Prüfungsverfahren eingereicht habe und die eingereichte schriftliche Fassung der auf dem elektronischen Speichermedium entspricht.

Hamburg, den ____________________ Unterschrift: ________________________

The author would like to name this thesis "The best terahertz generation ever". However, she is afraid that the readers would roll their eyes and refuse to read further. As a result, she refrains from doing so.

To my parents. 致亲爱的爸爸妈妈.

Acknowledgments

Here, I would like to thank my parents (Wang Bin, Li Shou) for supporting me regardless of what decision I make. Because of them, I am aware that home is a place where I am safe and can go back at any time. I would also like to thank all my friends that supported me during the period of my Ph.D. Without you, my life would be far less meaningful.

In addition, I would like to mention my gratitude to Prof. Franz Kärtner for bringing challenges to my life. Besides, Dr. Arya Fallahi helped me out when I was stuck with the research. He is clever and kind. When I needed guidance, he took time to explain to me the physics in detail. Prof. János Hebling was dedicated to our collaboration and gave enlightening suggestions. Prof. Michael Doser encouraged me to pursue my dream of becoming a professor. Whenever I am at the edge of giving up, I think of his words. The discussions with Prof. Robin Santra were delightful. He could explain physics in a simple and understandable way. Dr. Bernd Klein gave a very comprehensive course in Python. This brought me the hope that among all the bad lecturers, there could still be the possibility of a good one. Dr. Steve Aplin, Dr. Luca Gelisio, Tim Gerhardt and Adrian Pagel have helped me in terms of the cluster, numerical problems, and computer hardware problems. Without them, I would have had a hard time dealing with my computer and might have lost my passion for programming. Dr. György Tóth is a very pleasant person. I was very happy to collaborate with him. Tobias Kroh has actively contributed to our work and he gave nice suggestions to the manuscript. Wenlong Tian had constant discussions with me related to the multi-cycle terahertz generation. This enhanced my understanding of the experiments.

The following acknowledgments are for my friends. I know that you probably will read this section line by line and try to figure out whose name shows up first, since generally the name order is connected to importance. Consequently, the following part follows the alphabetic order. This would save me great trouble in finding excuses in the future to explain why someone is more important than someone else.

Anchita Addhya gave me the best birthday gift that I will never forget. I know her as a cheering and caring person, always. Dorothea Geyken is my lovely German teacher. I was very happy to attend her course. Apart from learning German happily, I also felt relaxed and entertained during the course. Dongfang Zhang is a kind and considerate person. Our discussions are very enlightening. I am glad to have his advice as the experience from a senior researcher. Erwin Cano Vargas has filled my Ph.D with many cheesy songs and extracurricular knowledge. Elias Kueny was by my side during the entire Ph.D. study. I would like to show my heartfelt gratitude: "Dear Kueny, I appreciate every version of you". Fabian Scheiba has impressed everyone by stably remaining at his adiabatic state. It is reassuring to be teaching assistants with him. He is and will be the standard of "responsible". Giulio Maria Rossi is a very inspiring person. I enjoy talking to him and he always brings me a different perspective during the discussion. Halil Olgun has cheered me up on the raining days and chased my blues away with his positive personality. However, this doesn’t stop me from thinking of choking him to death due to the delay of our collaboration from time to time. Igor Tyulnev is unlucky enough to be my first student. He trained me to be more patient against my own will. Sometimes (yes, "sometimes", not "always". If you want me to use the word "always", more hard work is required!) he asks good questions. Julia Quante has helped me and gave me good suggestions during my first period of Ph.D. These suggestions turned out to be very crucial at the end of the Ph.D.. Nicolai Klemke has read and corrected my important papers and letters. His help largely enhanced my English writing skills. The small gossips with him also served as a nice break throughout the long working days. Neda Lotfiomran gave me support for my Ph.D. and I gained energy from the conversations we had. Yi Hua has accepted my forced cuddles and accompanied me when I was bored with my research.

Special acknowledgement: I would like to thank Igor Tyulnev, Elias Kueny, Dongfang Zhang and Wenlong Tian for reading and correcting this thesis. The German version of the abstract is translated by Fabian Scheiba, which I highly appreciate.

Abstract

Regardless of many innovations and breakthroughs related to the terahertz technology, the widespread use of the phrase "terahertz gap" still describes the challenges both in the sensitivity of typical detectors and the power available from typical sources. This study revolves around the source of the terahertz radiation and in particular the laser-based terahertz generation. The thesis serves the purpose of the AXSIS project where the terahertz-driven electron acceleration is developed, which can be utilized in a potential attosecond X-ray source. Two main aspects of laser-based terahertz generation problem are discussed. One is the single- to few-cycle terahertz generation. This format of terahertz pulses is commonly achieved by utilizing the tilted-pulse-front technique. Five different experimental setups are proposed and simulated for generating the pulse front tilt. The advantages and disadvantages of each scheme are discussed in detail. The terahertz electric field distribution and the Fresnel loss due to out-coupling are analyzed. These can give guidance to terahertz-related experiments, and suggest the most appropriate setup for a given experiment. The simulations suggest that close to 0.8% conversion efficiency is possible at room temperature. The other aspect is the generation of multi-cycle terahertz pulses using periodically poled lithium niobate. In order to achieve high conversion efficiency, phase compensation with optical pump pulse recycling is proposed. Additionally, the study indicates that a phase-front fluctuation, common for high energy lasers, can induce damage via the terahertz generation process. The simulations indicate that beam energies on the level of a few tens of mJ can be achieved.

Object-oriented numerical packages are developed. For single- to few-cycle terahertz generation, a full 3D+1 numerical model is implemented using MATLAB. This model precisely captures the diffraction, walk-off and nonlinear interactions of the optical pump and the terahertz pulses. For multi-cycle terahertz generation, a numerical model assuming cylindrical symmetry is developed using C++. The MPI and OpenMP are used for parallelization.

The numerical models utilize the split-step Fourier and the finite difference methods. The structure of the numerical models supports future implementation of new material properties, higher-order nonlinear processes, and different numerical methods.

Keywords: terahertz generation, nonlinear optics, tilted-pulse-front, periodically poled lithium niobate, numerical method, coupled nonlinear wave equations

Zusammenfassung

Trotz vieler Innovationen und erheblichem Interesse an der Terahertz-Technologie, beschreibt die "Terahertz-Lücke" noch immer die Schwierigkeiten in der Detektion und der begrenzten erreichbaren Leistung von Strahlungsquellen in diesem Frequenzband. Hier setzt die vorliegende Arbeit an und befasst sich durch numerische Simulationen insbesondere mit der auf optischen Laserpulsen basierten Erzeugung von Terahertz (THz)-Strahlung. Eingegliedert in das AXSIS Forschungsprojekt soll eine rein auf optischen Lasern basierte Elektronenbeschleunigung durch THz-Strahlung schließlich zu ultrakurzen Röntgenpulsen mit einer Dauer von wenigen Attosekunden führen. Es werden zwei Schwerpunkte der laserbasierten Erzeugung von THz-Strahlung diskutiert, einerseits die Erzeugung von Ein-Zyklen-Pulsen und andererseits von Mehr-Zyklen-Pulsen. Ein-Zyklen-THz-Pulse werden durch Pulsfrontverkippung eines optischen Pulses erzeugt. Fünf verschiedene experimentelle Aufbauten zur Pulsfrontverkippung werden gezeigt und anhand von numerischen Simulationen diskutiert. Insbesondere die elektrische Feldverteilung und die Fresnelverluste an den Kristalloberflächen werden betrachtet, μm schließlich die Effizienz im Experiment zu maximieren. Die Simulationen in der vorliegenden Arbeit führen zu einer maximal erreichbaren Effizienz von 0,8% für Kristalle in Raumtemperaturumgebung. Für die bereits erwähnten Mehr-Zyklen-THz-Pulse werden zur Erzeugung periodisch gepolte Lithiumniobat-Kristalle genutzt. Eine Steigerung der Effizienz wird möglich durch die Phasenkompensation zwischen optischem und THz-Puls und der wiederholten THz-Strahlungserzeugung durch ein und denselben Laserpuls. Eine aus den Simulationen gewonnene Erkenntnis sind Kristalldefekte, hervorgerufen durch die THz-Strahlungserzeugung selbst, wenn sie Phasenfrontfluktuationen des Erregerpulses, die typischerweise bei Hochenergielasern auftreten, ausgesetzt ist. Die final berechneten THz-Pulsenergien erreichen einige Dutzend Millijoule.

Für die vorliegende Studie wurden Objekt orientierte, numerische Softwarepakete entwickelt. Die Berechnungen zu Ein-Zyklen-THz-Pulsen erforderte die Entwicklung eines vollständigen numerischen 3D+1 Modells in MATLAB, das die Effekte der Beugung, walk-off und nichtlinearen Kopplungen der optischen Erregerpulse und THz-Pulse erfasst. Für die Simulationen zu Mehr-Zyklen-THz-Pulsen wurde ein Programmcode in C++ unter Annahme der Zylindersymmetrie entwickelt, welcher MPI und OpenMP für die Parallelisierung nutzt.

Übergreifend nutzen die numerischen Modelle die Split-Step Fourier- und die Finite-Differenzen-Methode. Die generische Struktur der Programmierung erlaubt das Ergänzen von neuen Materialparametern, nichtlinearen Prozessen höherer Ordnung und weiteren numerischen Methoden für zukünftige Anwendungen.

Schlüsselwörter: THz-Strahlungserzeugung, nichtlineare Optik, Pulsfrontverkippung, periodisch gepoltes Lithiumniobat, numerische Methode, gekoppelte nichtlineare Wellengleichung

Contents

List of abbreviations

Abbreviation	Description
BA	Brewster angle
CG	conventional grating
DFG	difference frequency generation
FDTD	finite difference time-domain
FFT	fast Fourier transform
FFT-BPM	fast Fourier transform beam propagation method
FWHM	full width half maximum
GDD	group delay dispersion
K-K	Kramers-Kronig
LN	lithium niobate ($LiNbO_3$)
MSPM	multi-step phase mask
NLES	nonlinear echelon
OP	optical pump
PPLN	periodically poled lithium niobate
PM	phase-matching
QC	quartz coupler
RES	reflective echelon
SPM	self-phase-modulation
SRS	stimulated Raman scattering
SS	self-steepening
STC	spatio-temporal chirp
STFT	short time Fourier transform
TEM	transverse electric mode
THz	terahertz
THz-TDS	terahertz time-delay spectroscopy
TOD	third order dispersion
TPF	tilted-pulse-front

Part I

Introduction

The last decades have seen a surge in research studies on generation and applications of terahertz radiation, which typically refers to electromagnetic waves in the spectral range from 0.1 to 10 THz. The lower frequency side reaches the microwave and the higher frequency side extends to the far-infrared.

Terahertz radiation is emitted as part of the black-body radiation and 300 K corresponding with energies to 0.3 THz on the order of a few μW[1]. While this thermal emission is very weak, the observation of these frequencies is important for characterizing the 10-20 K cold dust in the interstellar medium[2]. Furthermore, due to the long wavelength compared to near-infrared light, terahertz radiation results in higher penetration depth and could penetrate many opaque materials e.g. paper, plastics, and textiles[3]. Besides, many toxic and explosive material e.g. cocaine, ecstasy, TNT and RDX feature absorption lines between 0.5 and 5 THz[3]. The non-invasive detection compared to X-ray makes the terahertz field an ideal candidate for industrial and military settings. Additionally, terahertz wireless communication is another thriving field of terahertz technology. Compared to infrared wireless communications, terahertz radiation has higher bandwidth, less diffraction, and high data rates[4].

There are two main categories of the terahertz pulses: single-cycle and multi-cycle. Single- to few-cycle (broadband) high energy terahertz pulses have many promising applications such as spectroscopy[5], strong field terahertz physics[6;7], particle acceleration[8], electron spin manipulation[6] and phonon resonance studies[9]. Multi-cycle terahertz can be utilized for spectroscopy[10;11;12], semiconductor exciton excitation[13], and linear electron acceleration[8;14;15].

There are many possible ways to generate terahertz radiation. Free electron lasers and synchrotron radiation have a high degree of tunability and are capable of delivering high peak-power coherent terahertz pulses[16]. Gyrotrons, based on the principle of electron cyclotron radiation, are able to generate watt-to-megawatt-level terahertz continuous wave radiation[17] at low terahertz frequencies (0.3-1.3 THz)[18;19]. Quantum cascade lasers are attractive due to their compactness and production simplicity in its use in the spectral range > 1 THz despite their limited tunability[20;21;22]. Molecular gas lasers can provide high terahertz energies but are less tunable in terms of the generated terahertz frequency[23].

Alternatively, laser based terahertz generation can leverage on developments in solid-state laser technology to enable compact coherent terahertz sources with high conversion efficiency at low terahertz frequency (<1 THz)[24;25;26]. It brings the advantages of high accessibility and intrinsic synchronization. The terahertz range stimulated emission is first demonstrated in the 1960s using hydrogen cyanide (HCN) and related molecules in pulsed electrical discharges[27;28]. Laser based terahertz generation typically falls into three categories. One, using electrically-charged photoconductive antennas[29;30], where excitation of semiconductors by an ultrashort pulse and subsequent radiation of a sub-picosecond pulse[31] form transient photocurrents. The emitted terahertz pulse properties are determined by the carrier lifetime of the material, the applied voltage and the breakdown threshold[32]. The second category is based on laser-induced plasma radiation in air or noble gases. Here, the incident optical pulse induces a ponderomotive force which causes a charge separation between ions and electrons, leading to the emission of a terahertz pulse[33;34], with peak electric fields that can reach as high as a few MV/cm[35]. However, the terahertz frequency, spatial distribution and polarizability are strongly related to the plasma density, plasma length, and plasma defocusing effect[36;37], which can be difficult to control. Difference frequency generation or optical rectification is the third category.

At early stage, the homodyne detection with a photodiode, is used to measure terahertz signals[38]. The modern laser based terahertz detection generally utilize terahertz time-delay spectroscopy (THz-TDS), which measures both the amplitude and phase information of the frequency components the terahertz pulse contains[39]. However, the THz-TDS employs single-pixel detectors and thus requires scanning in order to obtain a 2D image. Therefore, it consumes long image acquisition time[40]. THz-TDS is an ideal method to measure mobile charge carriers which reflect and absorb terahertz radiation. Electro-optic Sampling (EOS) is another alternative. In EOS, the terahertz pulse together with an optical pump is sent together through a nonlinear medium. Via the second-order nonlinear process, the polarization change of the optical pump changes according to the amplitude of the terahertz field. By scanning the relative delay of the terahertz and the optical fields, the entire terahertz electric field can be measured.

Regardless of many innovations and breakthroughs related to the terahertz technology, the widespread use of the phrase "terahertz gap" still describes the challenges both in the sensitivity of typical detectors and the power available from typical sources. This study revolves around the source of the terahertz radiation and in particular the laser-based terahertz generation. The thesis serves the purpose of the AXSIS project[41] where the terahertz-driven attosecond X-ray source is developed. The analysis in the thesis can bring insights into few- and multi-cycle terahertz generation problems and give guidance to related experiments.

1 Nonlinear polarization

In this section, I focus on the origin of the material nonlinear response. It serves as background to prepare the readers before they venture to nonlinear optics. The terahertz generation process utilizes the second order nonlinearity of the material via the difference frequency generation (DFG) process, where two pump beams generate another beam with the difference of the optical frequencies of the pump beams. Specifically in this thesis, up to the third order nonlinearity is considered. In order to understand the origin of the nonlinear polarizations and grasp the essence of terahertz generation. I start from the Maxwell equations for a homogeneous non-magnetic material,

$$\begin{aligned}\nabla \times E(r,t) &= -\frac{\partial B(r,t)}{\partial t} \\ \nabla \times H(r,t) &= J(r,t) + \frac{\partial D(r,t)}{\partial t} \\ \nabla \cdot D(r,t) &= \rho(r,t) \\ \nabla \cdot B(r,t) &= 0\end{aligned}$$

where the current density $J(r,t) = 0$, the free charge density $\rho(r,t) = 0$, $\mu_0 H(r,t) = B(r,t)$ and $D = \varepsilon_0 E(r,t) + P(r,t)$. The polarization $P(r,t)$ can be written as a sum of polarization currents stemming from different nonlinear orders in the form of $P(r,t) = \sum_{n=1}^{\infty} P^{(n)}(r,t)$, where $P(r,t)$ is formulated according to[42].

$$\begin{aligned}
P^{(1)}(r,t) &= \int dt' \chi^{(1)}(t') E(r,t-t') \\
P^{(2)}(r,t) &= \iint dt' dt'' \chi^{(2)}(t',t'') E(r,t-t') E(r,t-t'') \\
P^{(3)}(r,t) &= \iiint dt' dt'' dt''' \chi^{(3)}(t',t'',t''') E(r,t-t') E(r,t-t'') E(r,t-t''') \\
&\dots
\end{aligned} \tag{1}$$

From the convolution theorem, one can also write the polarization term as a product of $\chi^{(n)}(t-t', t-t'' \dots)$ and $E(t), E(t') \dots$ which is equivalent to Eq. (1). The polarizations are defined in the convolution forms of the electric fields and the susceptibilities are defined in the time domain. The polarizations should only depend on the difference of times e.g $t-t'$ and not on their individual values. More detailed explanations are given by P. Butcher[43]. For simplicity, I neglect the spatial dependence of the material response (r dependence). By applying the Fourier transform, one can rewrite Eq. (1) in the form of Eq. (2), where $\omega_0 = \sum_{m=1}^{n} \omega_m$ and the susceptibility $\chi^{(n)}(\omega_0;\, \omega_1, \omega_2, \dots, \omega_n) = \mathscr{F}[\chi^{(n)}(t', t'', \dots)]$.

$$P^{(n)}(t) = \int d\omega_1 \dots \int d\omega_n \, \chi^{(n)}(\omega_0;\, \omega_1, \omega_2, \dots, \omega_n) E(\omega_1) E(\omega_2) \dots E(\omega_n) \exp[i\omega_0 t] \tag{2}$$

From Eq. (2), it can be seen that

$$P^{(n)}(\omega_0) = \chi^{(n)}(\omega_0;,\, \omega_1, \omega_2, \dots, \omega_n) E(\omega_1) E(\omega_2) \dots E(\omega_n).$$

The first variable of $\chi^{(n)}$ (ω_0 in this case) is separated by ";". It represents the final resulting frequency after the contraction with all the electric fields. For any order of the susceptibilities, there are three conditions (see Eq. (3a-3c)) that need to be full filled.

$$\begin{cases}
\chi^{(n)}(\omega_0;\, \omega_1, \dots, \omega_n) = \chi_e^{(n)}(\omega_0;\, \omega_1, \dots, \omega_n) + \chi_i^{(n)}(\omega_0;\, \omega_1, \dots, \omega_n) & \text{(3a)} \\
\chi^{(n)}(\omega_0;\, -\omega_1, \dots, \omega_n) = \chi^{(n)}(\omega_0;\, \omega_1, \dots, \omega_n)^* & \text{(3b)} \\
\text{Kramers-Kronig formulae (K-K)} & \text{(3c)}
\end{cases}$$

Equation (3a) shows that the susceptibility is always a combination of both the ions ($\chi_i^{(n)}$) and the electrons ($\chi_e^{(n)}$) susceptibilities[44;45]. Equation (3b) guarantees that $\chi^{(n)}(t', t'', \dots)$ is a real function. The Kramers-Kronig (K-K) formulas guarantee the causality. At $t < 0$,

$\chi^{(n)}(t) = 0$ and this suggests causality. Since the polarization is a material response induced by the external electric field, the response should only be present after the external field has arrived (i.e. $t > 0$). Figure 1 shows one example of $\chi^{(1)}$ in frequency and corresponding time domain.

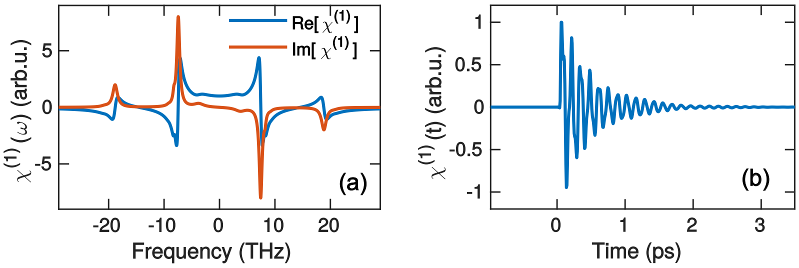

Figure 1: First order susceptibility $\chi^{(1)}$ in frequency and time domains are plotted in (a) and (b) respectively.

Specifically, the K-K formulae (3c) are,

$$\begin{aligned}
\mathfrak{R}[\chi^{(n)}(\omega_0;\, \omega_1, \dots \omega_i \dots, \omega_n)] &= \int_{-\infty}^{\infty} \frac{d\omega_i' \mathfrak{I}[\chi^{(n)}(\omega_0;\, \omega_1, \dots \omega_i' \dots, \omega_n)]}{\pi(\omega_i' - \omega_i)} \\
&= \frac{2}{\pi} \int_0^{\infty} \frac{d\omega_i' \omega_i' \mathfrak{I}[\chi^{(n)}(\omega_0;\, \omega_1, \dots \omega_i' \dots, \omega_n)]}{(\omega_i'^2 - \omega_i^2)} \qquad (4)
\end{aligned}$$

$$\begin{aligned}
\mathfrak{I}[\chi^{(n)}(\omega_0;\, \omega_1, \dots \omega_i \dots, \omega_n)] &= -\int_{-\infty}^{\infty} \frac{d\omega_i' \mathfrak{R}[\chi^{(n)}(\omega_0;\, \omega_1, \dots \omega_i' \dots, \omega_n)]}{\pi(\omega_i' - \omega_i)} \\
&= -\frac{2\omega_i}{\pi} \int_0^{\infty} \frac{d\omega_i' \mathfrak{R}[\chi^{(n)}(\omega_0;\, \omega_1, \dots \omega_i' \dots, \omega_n)]}{(\omega_i'^2 - \omega_i^2)} \qquad (5)
\end{aligned}$$

where $\mathfrak{R}$ and $\mathfrak{I}$ indicate the real and imaginary part, respectively. In the following context, we show that the commonly used harmonic oscillator model satisfies the K-K relation. Without loss of generality, the first order susceptibility $\chi^{(1)}(\omega;\, \omega) = 1/(\omega_0^2 - \omega^2 + i\Gamma\omega)$ is chosen as an example. In order to prove that the harmonic oscillator satisfies Eqs. (4) and (5), a contour integral within the complex plane needs to be used (see Fig. 2).

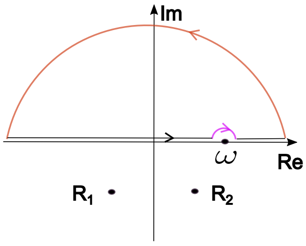

Figure 2: The summation of paths L_1, L_2 and L_3 is a contour integral in the complex plane, with $\Gamma < 0$, R_1, R_2 representing two poles of $\chi^{(1)}(\omega')$ in the complex plane.

Since the entire function is analytic in the upper half plane, one can write the contour integral as the following,

$$\frac{1}{\pi}\oint d\omega' \frac{\chi^{(1)}(\omega')}{\omega'-\omega} = \frac{1}{\pi}\int_{-\infty}^{\infty} d\omega' \frac{\chi^{(1)}(\omega')}{\omega'-\omega} - i\mathrm{Res}_{\omega'=\omega}[\frac{\chi^{(1)}(\omega')}{\omega'-\omega}] + \frac{1}{\pi}\int_{L_3} d\omega' \frac{\chi^{(1)}(\omega')}{\omega'-\omega} = 0. \quad (6)$$

where Res represents the residue. Along the path L_3, $|\omega'| = \infty$. As a result, the L_3 related integral vanishes. Consequently, Eq. (6) reduce to

$$\begin{aligned} \frac{1}{\pi}\int_{-\infty}^{\infty} d\omega' \frac{\chi^{(1)}(\omega')}{\omega'-\omega} &= i\chi^{(1)}(\omega) \\ \frac{1}{\pi}\int_{-\infty}^{\infty} d\omega' \frac{\Re[\chi^{(1)}(\omega')] + i\Im[\chi^{(1)}(\omega')]}{\omega'-\omega} &= i\Re[\chi^{(1)}(\omega)] - \Im[\chi^{(1)}(\omega)]. \end{aligned} \quad (7)$$

By relating the real and imaginary parts on both sides of the Eq. (7), one can get Eqs. (4) and (5). Of course one can also perform a brute force calculation. Here, I show one example of $\Im[\chi^{(1)}(\omega)]$. The $\Re[\chi^{(1)}(\omega)]$ follows the same manner. By choosing the upper half complex plane as in Fig. 2, one can get

$$\begin{aligned}
&\frac{1}{\pi}\int_{-\infty}^{\infty} d\omega' \frac{\Im[\chi^{(1)}(\omega')]}{\omega'-\omega} = \frac{1}{\pi}\int_{-\infty}^{\infty} d\omega' \frac{1}{\omega'-\omega}\left[\frac{-\Gamma\omega'}{(\omega'^2-\omega_0^2)^2+\Gamma^2\omega'^2}\right] \\
= \quad & -2i\left\{-\frac{1}{2}\mathrm{Res}[\omega] + \mathrm{Res}\left[\frac{-i\Gamma}{2}+\sqrt{\omega_0^2-\frac{\Gamma^2}{4}}\right] + \mathrm{Res}\left[\frac{-i\Gamma}{2}-\sqrt{\omega_0^2-\frac{\Gamma^2}{4}}\right]\right\} \\
= \quad & -2i\left\{\frac{1}{2}\left[\frac{\Gamma\omega}{(\omega^2-\omega_0^2)^2+\Gamma^2\omega^2}\right] - \frac{1}{4i}\left[\frac{1}{\sqrt{\omega_0^2-\frac{\Gamma}{4}}\left(-\frac{i\Gamma}{2}-\omega+\sqrt{\omega_0^2-\frac{\Gamma^2}{4}}\right)}\right]\right. \\
& \left. -\frac{1}{4i}\left[\frac{1}{\sqrt{\omega_0^2-\frac{\Gamma}{4}}\left(\frac{i\Gamma}{2}+\omega+\sqrt{\omega_0^2-\frac{\Gamma^2}{4}}\right)}\right]\right\} \\
= \quad & \frac{\omega_0^2-\omega^2}{(\omega^2-\omega_0^2)^2+\Gamma^2\omega^2} = \Re[\chi^{(1)}(\omega)] \qquad (8)
\end{aligned}$$

which agrees with Eq. (5). Using the concept of perturbation theory, one can also expand the polarization in the following form

$$P(\omega_0) = \varepsilon_0 \sum_{n=1}^{\infty} \chi^{(n)}(\omega_0;\, \omega_1, \ldots) E(\omega_1) \ldots E(\omega_n) = Ne \sum_{n=1}^{\infty} q^{(n)}(\omega_0) \qquad (9)$$

where ε_0 denotes vacuum permittivity, N represents the density of charged dipoles and e is the elementary charge. The term $q^{(n)} = q_i^{(n)} + q_e^{(n)}$ represents the induced dipole displacement where $q_e^{(n)}$ and $q_i^{(n)}$ are the induced displacements of the electron and ion, respectively.

$$\ddot{q}_i + \omega_i^2 q_i + \Gamma_i \dot{q}_i + \frac{a}{m_i}(q_i - q_e)^2 + \frac{b}{m_i}(q_i - q_e)^3 = \frac{e_i}{m_i}(E_1 \exp[i\omega_1 t] + E_2 \exp[i\Omega_1 t]) \qquad (10)$$

$$\ddot{q}_e + \omega_e^2 q_e + \Gamma_e \dot{q}_e - \frac{a}{m_e}(q_i - q_e)^2 - \frac{b}{m_e}(q_i - q_e)^3 = \frac{e_e}{m_e}(E_1 \exp[i\omega_1 t] + E_2 \exp[i\Omega_1 t]) \qquad (11)$$

The dot '·' above the variable represents the derivative with respect to time (t). In order to get the frequency dependent susceptibility, the coupled oscillator model (see Eqs. (11) and (10)) is used, where ω_1 represents an optical frequency, Ω_1 represents a terahertz (phonon) frequency, a and b are the second and third order electron-ion coupling coefficients, respectively and e_i and e_e represent the positive and negative elementary charges, respectively[44;45;46] . The terms $(q_i - q_e)^2$ and $(q_i - q_e)^3$ represent the coupling between the ion and the electron, where $q_i - q_e$ is exactly the dipole distance. The coupling terms start from the second order and the first order is neglected. This is due to the fact that the external driving field $E_1 e^{i\omega_1 t} + E_2 e^{i\Omega_1 t}$ is generally far larger than the linear response of the dipole itself. The origin of these terms comes from the expansion of the potential

$$V(q_i - q_e) = c_1(q_i - q_e) + c_2(q_i - q_e)^2 + c_3(q_i - q_e)^3 + c_4(q_i - q_e)^4 \dots$$

, where $c_1 = 0$ because at the bottom of the potential well, the first order derivative is zero. The force can be written as

$$\begin{aligned} F_i &= -\frac{\overrightarrow{q_i - q_e}}{|q_e - q_i|} \partial V(q_i - q_e)/\partial(q_i - q_e) \\ F_e &= -\frac{\overrightarrow{q_e - q_i}}{|q_e - q_i|} \partial V(q_i - q_e)/\partial(q_i - q_e) \end{aligned}$$

The directions of F_i and F_e are opposite to each other, which explains the sign difference in front of the $(q_i - q_e)$ related terms in Eqs. (11) and (10). The material is neutral of charge. As a result, the induced electron charge density is equal to the induced ion charge density. The resonance frequency of the ion and the electron are represented by ω_i and ω_e, respectively. In the following context, I will prove that the lower order coupling can contribute to higher orders, i.e. $(q_i - q_e)^2$ is responsible for the second order susceptibility ($\chi^{(2)}$) and it can also cause higher order susceptibilities ($\chi^{(3)}, \chi^{(4)}, \dots$). However, the high order terms can not contribute to the low orders. In other words, $(q_i - q_e)^n$ contributes to $\chi^{(m)}$ where $m \geqslant n$. On a macroscopic scale, $q_i - q_e$ is exactly the dipole distance. By using perturbation theory to expand the solution where λ ranges from 0 to 1, one can get[47]

$$\begin{aligned} q_i &= \lambda q_i^{(1)} + \lambda^2 q_i^{(2)} + \lambda^3 q_i^{(3)} \dots \\ q_e &= \lambda q_e^{(1)} + \lambda^2 q_e^{(2)} + \lambda^3 q_e^{(3)} \dots \end{aligned}$$

By putting the electric field to the first order, separating the terms with the same order of λ and setting λ to 1, one can get the following equation set, where Eq. (10) is solved as an example.

$$\begin{aligned}
\lambda: &\quad \ddot{q_i}^{(1)} + \omega_i^2 q_i^{(1)} + \Gamma_i \dot{q_i}^{(1)} = \frac{e_i}{m_i}(E_1 e^{i\omega_1 t} + E_2 e^{i\Omega_1 t}) && (12)\\
\lambda^2: &\quad \ddot{q_i}^{(2)} + \omega_i^2 q_i^{(2)} + \Gamma_i \dot{q_i}^{(2)} + \frac{a}{m_i}((q_i^{(1)})^2 + (q_e^{(1)})^2 - 2q_e^{(1)} q_i^{(1)}) = 0 && (13)\\
\lambda^3: &\quad \ddot{q_i}^{(3)} + \omega_i^2 q_i^{(3)} + \Gamma_i \dot{q_i}^{(3)} + \frac{2a}{m_i}(q_i^{(1)} q_i^{(2)} - q_i^{(1)} q_e^{(2)} - q_e^{(1)} q_i^{(2)} + q_e^{(1)} q_e^{(2)}) &&\\
&\quad + \frac{b}{m_i}\left[(q_i^{(1)})^3 + 3q_i^{(1)}(q_e^{(1)})^2 - 3q_e^{(1)}(q_i^{(1)})^2 - (q_e^{(1)})^3\right] = 0 && (14)\\
&\quad \ldots\ldots
\end{aligned}$$

1.1 Frequency dependent $\chi^{(1)}$

By Fourier transforming Eq. (12), one can get

$$q_i^{(1)} = \frac{e_i E_1}{m_i(\omega_i^2 - \omega_1^2 + i\Gamma_i\omega_1)} + \frac{e_i E_2}{m_i(\omega_i^2 - \Omega_1^2 + i\Gamma_i\Omega_1)} \tag{15}$$

Since ω_1 is far bigger than ω_i, the first term on the right hand side of Eq. (15) can be neglected. Consequently, by combining Eqs. (9), (11), (10) and (15), the solutions of the linear terms of the ion and electron are

$$q_i^{(1)}(\Omega_1) \approx \frac{e_i E_2}{m_i(\omega_i^2 - \Omega_1^2 + i\Gamma_i\Omega_1)} \Rightarrow \chi_i^{(1)}(\Omega_1) = \frac{Ne_i^2}{m_i\varepsilon_0(\omega_i^2 - \Omega_1^2 + i\Gamma_i\Omega_1)} \tag{16}$$

$$q_e^{(1)}(\omega_1) \approx \frac{e_e}{m_e(\omega_e^2 - \omega_1^2 + i\Gamma_e\omega_1)} \Rightarrow \chi_e^{(1)}(\omega_1) = \frac{Ne_e^2}{m_e\varepsilon_0(\omega_e^2 - \omega_1^2 + i\Gamma_e\omega_1)} \tag{17}$$

As a result $q^{(1)}(t) = \mathscr{F}[q^{(1)}(\omega)] = \sum_n q^{(1)}(\omega_n)e^{i\omega_n t}$, where $q^{(1)}(\omega_n) = eE/[m(\omega_0^2 - \omega_n^2 + i\Gamma_0\omega_n)]$ follows the solution of the oscillator format as in Eq. (15) and (17)[47]. Generally, the linear effects i.e. dispersion (frequency dependent refractive index n) and material absorption (α) are related to the real and the imaginary part the first order susceptibility $\chi^{(1)}(\omega)$ respectively by Eq. (18)[47].

$$n(\omega) + i\alpha(\omega) = \sqrt{1 + \chi^{(1)}(\omega)} \tag{18}$$

One can also try to understand Eq. (18) in the following way. Starting from the 1-dimension wave equation with the first order polarization and Fourier transforming both sides of the equation, one can get the following results

$$\mathscr{F}\left[\frac{\partial^2 E(z,t)}{\partial^2 z}\right] = \mathscr{F}\left[\frac{\partial^2 E(z,t) + \int dt' E(z,t-t')\chi^{(1)}(t')}{c^2\partial^2 t}\right]$$
$$\Rightarrow \frac{\partial^2 E(z,\omega)}{\partial^2 z} = \frac{-\omega^2}{c^2}[1+\chi^{(1)}(\omega)]E(z,\omega) \tag{19}$$

The solution of Eq. (19) is $E(z,\omega) = E_0 \exp[\pm i\sqrt{1+\chi^{(1)}}\omega/c]$. By plugging in Eq. (18), one can get $E(z,\omega) = E_0 \exp\{\pm i[n(\omega) + i\alpha(\omega)]\omega/c\}$. The term $\pm in(\omega)\omega/c = \pm ik(\omega)$ represents two plane wave solutions of Eq. (19), which propagate along z and $-z$ directions. The absorption of the electric field after propagation distance z is represented by $\exp[-\omega|\alpha|z/c]$.

In order to further understand the first order susceptibility $\chi^{(1)}$, I try to fit the experimentally measured data with the oscillator model. The refractive index and absorption at the terahertz frequency range of the congruent Lithium Niobate (LN) along the extraordinary axis is chosen as an example. The dielectric function is expressed in form of a summation of oscillators as shown in Eq. (20)[48;49]. The resonance frequency (ω_i) and the corresponding damping (Γ_i) (see Table. 1) are obtained from Raman spectroscopy A_1 (TO)[48;49].

$$\varepsilon = \varepsilon_\infty + \sum_{i=1}^{n} \frac{s_i\omega_i^2}{\omega_i^2 - \omega^2 + i\omega\Gamma_i} \tag{20}$$

Table 1: Raman resonance of lithium niobate at terahertz frequencies

Resonance frequency ω_i (THz)	3.9	7.44	8.22	9.21	18.84	20.76
Weighting s_i	4	16	1	0.16	2.55	0.13
Damping Γ_i (THz)	2.25	0.63	0.42	0.75	1.02	1.47

In the measurement of Barker. Jr et al., the first resonant frequency of the Raman scattering is $\omega_1 = 7.44$ THz[50], whereas M. Schall found that $\omega_1 = 3.9$ THz[48]. Within the frequency range of 0.25 THz to 2.5 THz the extraordinary congruent LN doesn't contain a resonance peak[51]. For the stimulated Raman scattering (SRS), the commonly reported first resonance is $\omega_1 = 7.44$ THz. This is because compared with the resonance at 7.44 THz, the one at 3.9 THz has much smaller weighting, and thus cannot be easily detected in the SRS process. In the specific case of this thesis, $\omega_1 = 3.9$ THz is necessary for the fitting of refractive index and absorption from 0 to 2.5 THz.

Figure 3(a) shows the fitting of $\chi^{(1)}$ based on the data presented in Table 1 and Eq. (20). Figure 3(b,c) are the comparisons between the fitted curves and experimental data obtained by Wu. X in our lab . The experimental data is only valid from 0.4 THz to 2 THz.

The damping term Γ is related to the absorption of the material. Smaller Γ leads to narrower waist of the resonance peak which can be seen from the red curve in Fig. 3(a). When the charged particles interact with the incident electric field, the emitted electromagnetic fields caused by the motion of the particles do not add up in phase with respect to the driving field, leading to destructive interference. This destructive interference causes energy loss from the electric field. The lost energy transfers into the thermal energy of the crystal and is used to overcome the potential when the charged particles move.

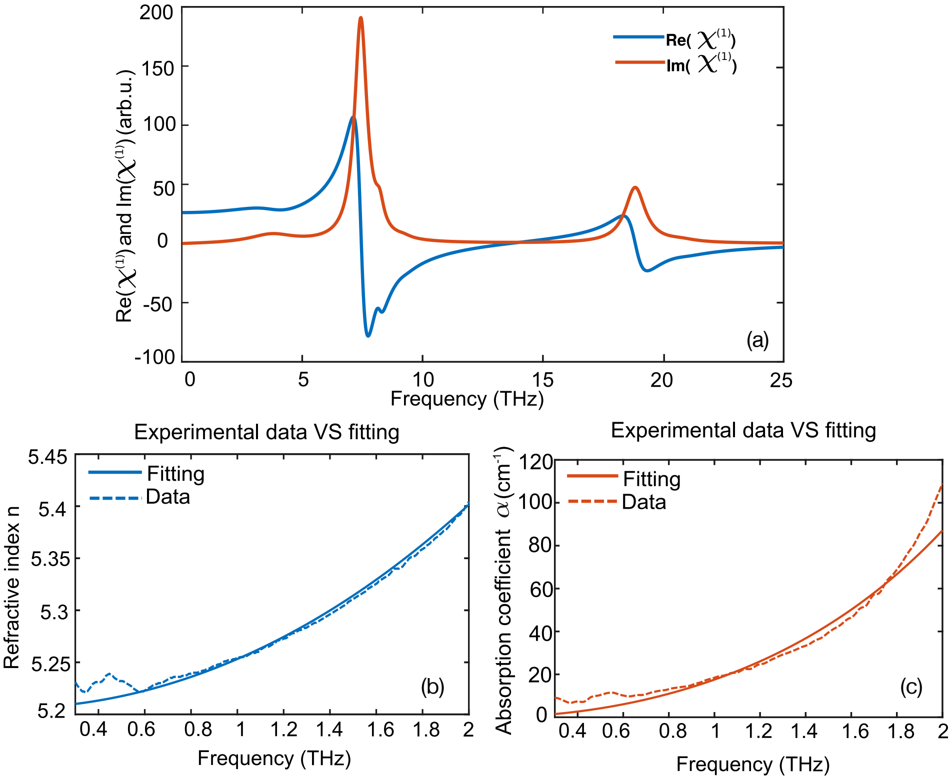

Figure 3: (a) With $\varepsilon_\infty = 2.3$, the real and imaginary part of $\chi^{(1)}$ are plotted against frequency. (b) and (c) are the refractive index and absorption coefficient (solid curves) derived from (a). The experimental data is represented by the dashed curves.

1.2 Frequency dependent $\chi^{(2)}$

The second order perturbation corresponds to the second order susceptibility which can be derived from Eq. (13). I am interested in terahertz generation, e.g. $\chi^{(2)}(\omega_1 - \omega_2; \omega_1, -\omega_2)$ where ω_1, ω_2 are at optical frequencies and $\omega_1 - \omega_2$ is at terahertz frequency. As a result, $q_e^{(1)}(\omega_1) \gg q_i^{(1)}(\omega_1)$. Consequently, for the second order perturbation (e.g. Eq. (13)) only the $q_e^{(1)}(\omega_1) q_e^{(1)}(\omega_2)^*$ term is considered. By calculating the second order response of both the ion and the electron, one can get

$$q_i^{(2)}(\omega_1-\omega_2;\,\omega_1,-\omega_2)= \\ \frac{-ae_e^2}{m_i m_e^2[\omega_i^2-(\omega_1-\omega_2)^2+i\Gamma_i(\omega_1-\omega_2)]}\left[\frac{E_1}{\omega_e^2-\omega_1^2+i\Gamma_e\omega_1}\right]\left[\frac{E_2}{\omega_e^2-\omega_2^2+i\Gamma_e\omega_2}\right]^* \tag{21}$$

$$q_e^{(2)}(\omega_1-\omega_2;\,\omega_1,-\omega_2)= \\ \frac{ae_e^2}{m_e^3[\omega_e^2-(\omega_1-\omega_2)^2+i\Gamma_e(\omega_1-\omega_2)]}\left[\frac{E_1}{\omega_e^2-\omega_1^2+i\Gamma_e\omega_1}\right]\left[\frac{E_2}{\omega_e^2-\omega_2^2+i\Gamma_e\omega_2}\right]^* \tag{22}$$

By combining Eqs. (9), (3a) (22) and (21), one can obtain Eq. (23).

$$\begin{aligned}&\chi^{(2)}(\omega_1-\omega_2;\,\omega_1,-\omega_2)=\chi_i^{(2)}(\omega_1-\omega_2;\,\omega_1,-\omega_2)+\chi_e^{(2)}(\omega_1-\omega_2;\,\omega_1,-\omega_2)\\ &=\chi_e^{(1)}(\omega_1)\chi_e^{(1)}(-\omega_2)\left[\frac{-a\varepsilon_0^2}{e_i e_e^2 N^2}\chi_i^{(1)}(\omega_1-\omega_2)+\frac{a\varepsilon_0^2}{e_e^3 N^2}\chi_e^{(1)}(\omega_1-\omega_2)\right]\\ &=\delta_{\text{miller}}\chi_e^{(1)}(\omega_1)\chi_e^{(1)}(-\omega_2)\chi^{(1)}(\omega_1-\omega_2)\end{aligned} \tag{23}$$

The Miller index δ_{miller} is defined by $\chi^{(2)}(\omega_1-\omega_2;\,\omega_1,-\omega_2)/\chi^{(1)}(\omega_1-\omega_2)\chi_e^{(1)}(\omega_1)\chi_e^{(1)}(\omega_2)$[47] which in our case equals to $a\varepsilon_0^2/(e^3N^2)$. Since the commonly used $\chi^{(2)}(\omega_1-\omega_2;\,\omega_1,-\omega_2)$ of the LN crystal is 305pm/V, the corresponding Miller coefficient is around 10^{-13}m/V, which is at a reasonable scale.[52]

From the previous discussion, one can see that for the second order polarization of a specific frequency can be written as $P^{(2)}(\omega_1-\omega_2)=\chi^{(2)}(\omega_1-\omega_2;\,\omega_1,-\omega_2)E(\omega_1)E(-\omega_2)$. In order to get the full spectrum of $P^{(2)}$, all possible frequency combinations need to be considered. This is achieved by considering a convolution in the spectral domain as shown in Eq. (24), where $\Omega=\omega_1-\omega_2$ i.e. the terahertz frequency range.

$$\begin{aligned}P^{(2)}(\Omega)\quad&=\int_{-\infty}^{\infty}\chi^{(2)}(\Omega;\,\omega,-\omega+\Omega)E(\omega)E(\omega-\Omega)^*d\omega\\ &=\delta_{\text{miller}}\chi^{(1)}(\Omega)\int_{-\infty}^{\infty}\chi_e^{(1)}(\omega)\chi_e^{(1)}(-\omega+\Omega)E(\omega)E(\omega-\Omega)^*d\omega\end{aligned} \tag{24}$$

If ω and $-\omega+\Omega$ are far from the electron resonance, $\chi_e^{(1)}(\omega)$ and $\chi_e^{(1)}(-\omega+\Omega)$ are all constants and can be taken out from the integration in Eq. (24). As a result, Eq. (24) can be written in the form,

$$
\begin{aligned}
P^{(2)}(\Omega) = & \quad \chi^{(2)}(\Omega;\,\omega,-\omega+\Omega)\int_{-\infty}^{\infty} dt_1 \int_{-\infty}^{\infty} dt_2 \int_{-\infty}^{\infty} d\omega E(t_1)e^{-it_1\omega}E(t_2)^* \exp[it_2(\omega-\Omega)] \\
= & \quad \chi^{(2)}(\Omega;\,\omega,-\omega+\Omega)\int_{-\infty}^{\infty} dt_1 \int_{-\infty}^{\infty} dt_2 \delta(t_1-t_2)E(t_1)E(t_2)^* \exp[-it_2\Omega] \\
= & \quad \chi^{(2)}(\Omega;\,\omega,-\omega+\Omega)\int_{-\infty}^{\infty} |E(t)|^2 \exp[-it\Omega]dt. \qquad (25)
\end{aligned}
$$

1.3 Frequency dependent $\chi^{(3)}$

The commonly calculated third order effects in the optical region are stimulated Raman (SR) effect and self phase modulation (SPM). In first order, $q_i^{(1)} \ll q_e^{(1)}$ since the driving fields are at optical frequencies. Consequently, $q_i^{(1)}$ related terms can be neglected. Since the Raman effect is related to the resonance of the phonon, the term $q_i^{(2)}(\Omega)$, where $\Omega = \omega_1 - \omega_2$, can be considerably large and thus should be included. One can see in the later results that the $q_i^{(2)}(\Omega)$ term brings in the phonon influence into the third order susceptibility and is directly related to the Raman response function $h(t)$. Additionally, since I am interested the $\chi^{(3)}(\omega)$ at the optical region, the $\chi_i^{(3)}(\omega)$ can be neglected.

$$
\begin{aligned}
&\ddot{q}_e^{(3)}(t) + \omega_e^2 q_e^{(3)}(t) + \Gamma_e \dot{q}_e^{(3)}(t) = e^{i\omega t}\frac{2a}{m_e}\Big[q_e^{(1)}(-\omega_1)q_e^{(2)}(\omega+\omega_1;\omega,\omega_1) \\
&+q_e^{(1)}(-\omega_2)q_e^{(2)}(\omega+\omega_2;\omega,\omega_2) - q_e^{(1)}(\omega-\Omega)q_i^{(2)}(\Omega;\omega_1,-\omega_2)\Big] \\
&-e^{i\omega t}\frac{b}{m_e}\left[q_e^{(1)}(\omega)\right]^2 q_e^{(1)}(-\omega) \qquad (26)
\end{aligned}
$$

Using Eq. (17) in chapter 1.1 and Eq. (87) in chapter 1.2, Eq. (26) becomes

$$
\begin{aligned}
&\ddot{q}_e^{(3)}(t) + \omega_e^2 q_e^{(3)}(t) + \Gamma_e \dot{q}_e^{(3)}(t) = \Big[c_1\chi_e^{(1)}(-\omega_1)\chi_e^{(1)}(\omega+\omega_1)\chi_e^{(1)}(\omega)\chi_e^{(1)}(\omega_1) \\
&+c_2\chi_e^{(1)}(-\omega_2)\chi_e^{(1)}(\omega+\omega_2)\chi_e^{(1)}(\omega)\chi_e^{(1)}(\omega_2) - c_3\chi_e^{(1)}(\omega-\Omega)\chi_e^{(1)}(\omega_1)\chi_e^{(1)}(-\omega_2)\chi_i^{(1)}(\Omega) \\
&-c_4\chi_e^{(1)}(-\omega)\chi_e^{(1)}(\omega)\chi_e^{(1)}(\omega)\Big]\exp[i\omega t] \qquad (27)
\end{aligned}
$$

where $c_1,\ c_2,\ c_3,\ c_4$ are constants. By solving Eq. (27) and absorbing other constants into $c_1,\ c_2,\ c_3,\ c_4$, one can get

$$\begin{aligned}\chi_e^{(3)}(\omega) = \quad & c_1\chi_e^{(1)}(\omega)\chi_e^{(1)}(-\omega_1)\chi_e^{(1)}(\omega+\omega_1)\chi_e^{(1)}(\omega)\chi_e^{(1)}(\omega_1) \\ & +c_2\chi_e^{(1)}(-\omega_2)\chi_e^{(1)}(\omega+\omega_2)\chi_e^{(1)}(\omega)\chi_e^{(1)}(\omega_2) \\ & -c_3\chi_e^{(1)}(\omega)\chi_e^{(1)}(\omega-\Omega)\chi_e^{(1)}(\omega_1)\chi_e^{(1)}(-\omega_2)\chi_i^{(1)}(\Omega) \\ & -c_4\chi_e^{(1)}(\omega)\chi_e^{(1)}(-\omega)\chi_e^{(1)}(\omega)\chi_e^{(1)}(\omega) \qquad (28)\end{aligned}$$

From Eq. (28), one can see that the third order susceptibility consists of two possibilities. In one of the possibilities, c_1 ,c_2 ,c_3 related terms represent the effective third order nonlinearity induced by the second order nonlinearity. In other words, if a second order nonlinear effect happens twice, it is equivalent to a third order effect. In the other possibility (c_4 related term), the third order effect is directly driven by the third order nonlinearity. If there are no resonances at the optical frequencies, all the optical frequency related $\chi_e^{(1)}$ are constants and do not vary much with respect to frequency. As a result, one can group c_1 ,c_2 ,c_4 related terms together as a constant α_1, which represents the instantaneous electronic response. Furthermore, the $\chi_i^{(1)}(\Omega)$ related term represents the phonon response i.e the stimulated Raman effect. As a result, one can write Eq. (28) in the form of Eq. (29), where $\Omega = \omega_1 - \omega_2$ represents the frequency difference at the optical region[53].

$$\chi_e^{(3)}(\omega) = \alpha_1 + \alpha_2\chi_i^{(1)}(\Omega) = \alpha_c h(\omega_1 - \omega_2) \qquad (29)$$

The third order of polarization can be written as Eq. (30)[53].

$$\begin{aligned}& P^{(3)}(\omega) = \alpha_c \int_{-\infty}^{\infty}\int_{-\infty}^{\infty} h(\omega_1-\omega_2)E(\omega-\omega_1+\omega_2)E(\omega_1)E(-\omega_2)d\omega_1 d\omega_2 \\ & = \alpha_c \int_{-\infty}^{\infty}\dots\int_{-\infty}^{\infty} h(\omega_1-\omega_2)E(t)\exp[-i(\omega-\omega_1+\omega_2)t]E(t_1) \\ & \times\exp[-i\omega_1 t_1]E(t_2)^* \exp[i\omega_2 t_2]d\omega_1 d\omega_2 dt_1 dt_2 dt \qquad (30)\end{aligned}$$

By performing a variable transformation and setting $\omega_1 - \omega_2 = \Omega$, one can get

$$\begin{aligned}
P^{(3)}(\omega) \quad &= \alpha_c \int_{-\infty}^{\infty} \cdots \int_{-\infty}^{\infty} \exp[-i\omega t] h(\Omega) E(t) E(t_1) E^*(t_2) \exp[-i(t_1 - t)\Omega] \\
&\times \exp[i(t_2 - t_1)\omega_2] dt_1 dt_2 dt d\Omega d\omega_2 \\
&= \alpha_c \int_{-\infty}^{\infty} \cdots \int_{-\infty}^{\infty} \exp[-i\omega t] h(\Omega) E(t) E(t_1) E^*(t_2) \exp[-i(t_1 - t)\Omega] \delta(t_1 - t_2) dt_1 dt_2 dt d\Omega \\
&= \alpha_c \int_{-\infty}^{\infty} \cdots \int_{-\infty}^{\infty} \exp[-i\omega t] h(\Omega) E(t) |E(t_1)|^2 \exp[-i(t_1 - t)\Omega] dt_1 dt d\Omega \\
&= \alpha_c \int_{-\infty}^{\infty} \int_{-\infty}^{\infty} \exp[-i\omega t] h(t - t_1) E(t) |E(t_1)|^2 dt_1 dt
\end{aligned} \tag{31}$$

Equation (31) is in the form of the stimulated Raman scattering that we are familiar with. One can also write the corresponding polarization in the time domain as

$$P^{(3)}(t) = c\varepsilon_0 n(\omega_0)^2 n_2 E(x, y, z, t) \int h(t - t_1) |E(x, y, z, t_1)|^2 dt_1 \tag{32}$$

where the n_2 is the intensity dependent refractive index and

$$h(t_1 - t) = \int_{-\infty}^{\infty} h(\Omega) \exp[-i\Omega(t_1 - t)] d\Omega.$$

It is also worth to notice that if the $h(\Omega) = h(0)$, which means $\omega_1 = \omega_2$, the $h(t_1 - t)$ reduces to a delta function which is exactly the case for self phase modulation. The delay in function $h(t_1 - t)$ comes from the real part of the $h(\omega)$ and the imaginary part of $h(\omega)$ takes into account the Raman gain.[54]

2 Coupled wave equations

Using Maxwell equations, one can get

$$\nabla \times (\nabla \times E(x, y, z, t)) = -\mu_0 \partial^2 D(x, y, z, t)/\partial t^2 = -\frac{1}{c^2} \partial^2 \left[E + P^{(1)} + P^{(2)} + P^{(3)}(t) ... \right] / \partial t^2 \tag{33}$$

Assuming the material is homogeneous, Eq. (1) can be written as $\nabla \cdot D(r, t) = \varepsilon \nabla \cdot E(r, t) = 0$. With the condition $\nabla \cdot E(r, t) = 0$, Eq. (33) becomes

$$\nabla^2 E(x, y, z, t) = \frac{1}{c^2} \partial^2 \left[E(t) + P^{(1)}(t) + P^{(2)}(t) + P^{(3)}(t) ... \right] / \partial t^2.$$

By Fourier transforming both sides and plugging in the ansatz of input electric field $\mathscr{F}[E(x,y,z,t)] = E(x,y,z,\omega) = E_0(x,y,z,\omega)\exp\{-i[k_{x0}(\omega)x + k_{y0}(\omega)y + k_{z0}(\omega)z]\}$, one can get

$$\begin{aligned}
&\frac{\partial^2 E_0(x,y,z,\omega)}{\partial x^2} + \frac{\partial^2 E_0(x,y,z,\omega)}{\partial y^2} + \frac{\partial^2 E_0(x,y,z,\omega)}{\partial z^2} - 2ik_{x0}(\omega)\frac{\partial E_0(x,y,z,\omega)}{\partial x} \\
&-2ik_{y0}(\omega)\frac{\partial E_0(x,y,z,\omega)}{\partial y} - 2ik_{z0}(\omega)\frac{\partial E_0(x,y,z,\omega)}{\partial z} - \cancel{[k_{x0}^2(\omega) + k_{y0}^2(\omega) + k_{z0}^2(\omega)]}E_0 \\
&= -\left\{\cancel{\frac{\omega^2}{c^2}\mathscr{F}[E(t) + P^{(1)}(t)]} + \frac{\omega^2}{c^2}\mathscr{F}[P^{(2)}(t) + P^{(3)}(t)...]\right\}\exp\{i[k_{z0}(\omega)z + k_{y0}(\omega)y + k_{x0}(\omega)x]\}
\end{aligned}$$

From Eq. (18), we know that when the absorption is negligible, $1 + \chi^{(1)}(\omega) = n(\omega)^2$ and thus $k_{x0}^2(\omega) + k_{y0}^2(\omega) + k_{z0}^2(\omega) = \frac{\omega^2}{c^2}[1 + \chi^{(1)}(\omega)]$ as shown in the canceled out terms above. As a result, one can get the wave equation as the following

$$\begin{aligned}
&\frac{\partial^2 E_0(x,y,z,\omega)}{\partial x^2} + \frac{\partial^2 E_0(x,y,z,\omega)}{\partial y^2} + \frac{\partial^2 E_0(x,y,z,\omega)}{\partial z^2} - 2ik_{x0}(\omega)\frac{\partial E_0(x,y,z,\omega)}{\partial x} \\
&-2ik_{y0}(\omega)\frac{\partial E_0(x,y,z,\omega)}{\partial y} - 2ik_{z0}(\omega)\frac{\partial E_0(x,y,z,\omega)}{\partial z} \\
&= -\frac{\omega^2}{c^2}\mathscr{F}[P^{(2)}(t) + P^{(3)}(t)...]\exp\{i[k_{z0}(\omega)z + k_{y0}(\omega)y + k_{x0}(\omega)x]\} \qquad (34)
\end{aligned}$$

By performing Fourier transform from the $x,\ y$ domain to $k_x,\ k_y$ domain on both sides of the equation and setting $(\omega^2/c^2)\mathscr{F}[P^{(2)}(t) + P^{(3)}(t)...]\exp\{i[k_{z0}(\omega)z + k_{y0}(\omega)y + k_{x0}(\omega)x]\} = P^{NL}(x,y,z,\omega)$, one can obtain,

$$\begin{aligned}
\left[\frac{\partial^2}{\partial z^2} - 2ik_{z0}(\omega)\frac{\partial}{\partial z}\right]E_0(k_x,k_y,z,\omega) &= \left[k_x^2 + k_y^2 + 2k_xk_{x0}(\omega) + 2k_yk_{y0}(\omega)\right]E_0(k_x,k_y,z,\omega) \\
&-P^{NL}(k_x,k_y,z,\omega). \qquad (35)
\end{aligned}$$

Equation (35) is of the standard second order nonhomogeneous differential equation. One can put the term $\left[k_x^2 + k_y^2 + 2k_xk_{x0}(\omega) + 2k_yk_{y0}(\omega)\right]E_0(k_x,k_y,z,\omega)$ to the left hand side, so that the homogeneous form of Eq. (35) follows the type $a_2E'' + a_1E' + a_0E = 0$. However, for the convenience of the following discussion, this term is shifted to the right hand side and serves together with P^{NL} as the source $g(z)$ of the nonhomogeneous equation (see Eq. 36).

$$g(z) = \left[k_x^2 + k_y^2 + 2k_xk_{x0}(\omega) + 2k_yk_{y0}(\omega)\right]E_0(k_x,k_y,z,\omega) - P^{NL}(k_x,k_y,z,\omega) \qquad (36)$$

With the source $g(z)$, the two independent solutions of the homogeneous equation are $y_1 = C_1,\ y_2(z) = C_2\exp[2ik_{z0}(\omega)z]$. Since the ansatz is

$$E(x, y, z, \omega) = E_0(x, y, z, \omega) \exp\{-i[k_{x0}(\omega)x + k_{y0}(\omega)y + k_{z0}(\omega)z]\}$$

where $E_0(x, y, z, \omega)$ is the envelope, solution y_1 represents the electric field which propagates along the z direction and solution y_2 represents the electric field which propagates along the $-z$ direction. One can construct a particular solution as

$$y_p(z) = -y_1(z) \int \frac{y_2(z)g(z)}{W(y1, y2)(z)} dz + y_2(z) \int \frac{y_1(z)g(z)}{W(y1, y2)(z)} dz \tag{37}$$

$$W(y_1, y_2)(z) = \begin{vmatrix} y_1 & y_1' \\ y_2 & y_2'. \end{vmatrix}$$

As a result, the final electric field is

$$\begin{aligned} E_0(x, y, z, \omega) &= y_1 + y_2(z) + y_p(z) \\ E(x, y, z, \omega) &= E_0(x, y, z, \omega) \exp\{-i[k_{x0}(\omega)x + k_{y0}(\omega)y + k_{z0}(\omega)z]\} \\ &= \Bigg\{ C_1 \exp[-ik_{z0}(\omega)z] + C_2 \exp[ik_{z0}(\omega)z] - \frac{\exp[-ik_{z0}(\omega)z]}{2ik_{z0}(\omega)z} \int g(z)dz \\ &\quad + \frac{\exp[ik_{z0}(\omega)z]}{2ik_{z0}(\omega)z} \int g(z) \exp[-2ik_{z0}(\omega)]dz \Bigg\} \exp\{-i[k_{x0}(\omega)x + k_{y0}(\omega)y]\} \\ &\approx \left[C_1 - \frac{1}{2ik_{z0}(\omega)} \int g(z)dz \right] \exp\{-i[k_{x0}(\omega)x + k_{y0}(\omega)y + k_{z0}(\omega)z]\} \end{aligned} \tag{38}$$

Due to the phase term $\exp[ik_{z0}(\omega)]$, the terms in red represent the electric fields which propagate towards the $-z$ direction. Within our range of study, both the terahertz generation in the periodically poled lithium niobate and the tilted-pulse-front setup do not involve back propagation waves, since there is no reflection in the system and the nonlinear interactions are always aimed at the forward propagation direction. Thus, the back propagation terms can be neglected.

Note that Eq. (38) leads to a very important result. It is the exact solution from the second order differential equation by only neglecting the backward propagation. However, it is exactly the same as the solution of Eq. (35) when the second order derivative is directly dropped (see Eq. (39)). This suggests that, as long as there is no backward propagating electric field, Eq. (39) is exact and is also valid to describe the few- to single-cycle pulses.

$$-2ik_{z0}(\omega)\frac{\partial E_0(k_x, k_y, z, \omega)}{\partial z} = \left[k_x^2 + k_y^2 + 2k_x k_{x0}(\omega) + 2k_y k_{y0}(\omega)\right] E_0(k_x, k_y, z, \omega) - P^{NL}(k_x, k_y, z, \omega) \tag{39}$$

In the following chapters, Eq. (39) is used for both single-cycle and multi-cycle terahertz generation.

3 Gaussian beam

In the development of the analytical results of the following models, the Gaussian function is chosen to be the pump pulse spatial and temporal shapes due to its friendly mathematical properties. It is possible to decompose a coherent paraxial beam using the orthogonal set of the Hermite-Gaussian modes in Cartesian coordinates or the Laguerre-Gaussian modes in cylindrical coordinates. Hermite-Gaussian modes and Laguerre-Gaussian modes are the solutions of the wave equations with different boundary conditions. I choose the transverse mode (TEM$_{00}$), where the electromagnetic field pattern of the radiation is in the plane perpendicular (i.e., transverse) to the radiation's propagation direction, since it resembles the optical laser field in free space.

The following context is based on the analytical expressions of the focusing and propagation of the Gaussian beam. This serves as the basis for Part. II since the analytical expressions of the optical pump electric field after various optical systems are used as the input in the numerical calculations. In other words, the numerical calculations only start when the optical pump interacts with the LN. By defining

$$z_R = \pi\sigma_0^2/\lambda_0, \;\; q(0) = iz_R \;\; k_0 = 2\pi\lambda_0$$

one can write the electric field in the following form

$$E(x) = \exp(-x^2/\sigma_0^2) = \exp(-ik_0x^2/2q(0)). \tag{40}$$

3.1 Free space propagation

With the approximation of free propagation and paraxial approximation, Eq. (**??**) reduces to $\partial E(k_x)/\partial z = ik_x^2/2k_0$. Consequently, one can obtain the solution

$$E(k_x, z) = E_0 \exp(ik_x^2 z/2k_0). \tag{41}$$

where z is the propagation distance, and $\exp(ik_x^2 z/2k_0)$ can be considered as a propagator. This indicates that the effect of free propagation is the multiplication of a quadratic phase in the reciprocal domain. This is similar to the temporal broadening in the time domain caused by the second order dispersion (GDD). The k_x and x is a Fourier pair similar to t and ω. In particular, here the "temporal broadening" is replaced by a broadening in space (x) which is exactly the effect of diffraction. In other words, quadratic phase of the electric field in one domain leads to the broadening of the field in the corresponding Fourier domain. By Fourier transforming Eq. (40), one can get

$$E(k_x) = \frac{1}{\sqrt{2\pi}} \int \exp(-ik_0 x^2/2q(0)) \exp(ik_x x)\, dx = \sqrt{\frac{q(0)}{ik_0}} \exp(ik_x^2 q(0)/2k_0).$$

By combining the equation above together with the propagator in Eq. (41), one can obtain the following,

$$\begin{aligned} E(x,z) = & \sqrt{\frac{q(0)}{ik_0 2\pi}} \int \exp\left(ik_x^2 q(0)/2k_0 + ik_x^2 z/2k_0 - ik_x x\right) dk_x \\ = & \sqrt{\frac{q(0)}{q(0)+z}} \exp\left[-\frac{ix^2 k_0}{2(q(0)+z)}\right] \end{aligned} \tag{42}$$

where the $q' = q(0) + z$ can be considered as the new complex beam parameter. In order to separate the real and imaginary parts, one can also rewrite $q' = q_r + iq_i$. Thus, the exponential term in Eq. (42) becomes

$$\exp\left[-\frac{ix^2 k_0}{2(q(0)+z)}\right] = \exp\left[-\frac{ix^2 k_0 q_r}{2(q_r^2 + q_i^2)}\right] \exp\left[-\frac{x^2 k_0 q_i}{2(q_r^2 + q_i^2)}\right] \tag{43}$$

Equation (43) is the general form which I will discuss more in the following chapters. Here, in this simple free propagation case, with $q_r = z, q_i = z_R$, one can rewrite Eq. (42) as

$$E(x,z) = \sqrt{\frac{\sigma_0}{\sigma(z)}} \exp\left[-\frac{i \arctan(z/z_R)}{2}\right] \exp\left[\frac{-x^2}{\sigma(z)^2}\right] \exp\left[\frac{-ik_0 x^2}{2R(z)}\right] \tag{44}$$

where

$$\frac{2(q_r^2 + q_i^2)}{k_0 q_i} = \sigma_0^2 \left[1 + \left(\frac{z}{z_R}\right)^2\right] = \sigma(z)^2 \tag{45}$$

$$\frac{(q_r^2 + q_i^2)}{q_r} = z\left[1 + \left(\frac{z_R}{z}\right)^2\right] = R(z) \tag{46}$$

In Eq. (44), the coefficient $\sqrt{\sigma_0/\sigma(z)}\exp\left[i\arctan\left(z/z_R\right)/2\right]$ is due to the diffraction only in one dimension. When considering the y dimension with identical diffraction behavior, one can obtain

$$E(x,y,z)=\frac{\sigma_0}{\sigma(z)}\exp\left[i\arctan\left(z/z_R\right)\right]\exp\left[\frac{-(x^2+y^2)}{\sigma(z)^2}\right]\exp\left[\frac{-ik_0(x^2+y^2)}{2R(z)}\right]$$

3.2 Propagation in medium

Here I derive the Gaussian beam expression after propagation distance z in a medium with refractive index n. Similar to Eq. (42), the effect of the medium on the propagation of the Gaussian beam is the reduced diffraction, since the medium decreases the wavelength of the electric field. Here the Fresnel loss of entering a medium is neglected. By modifying the propagator $\exp(ik_x^2z/2k_0)$ into $\exp(ik_x^2z/2k_0n)$, it can be seen that

$$\begin{aligned}E(x,z)=&\quad\sqrt{\frac{q(0)}{ik_02\pi}}\int\exp\left(ik_x^2q(0)/2k_0+ik_x^2z/2k_0n-ik_xx\right)dk_x\\ =&\sqrt{\frac{q(0)}{q(0)+z/n}}\exp\left[-\frac{ix^2k_0}{2(q(0)+z/n)}\right]\end{aligned}\tag{47}$$

Accordingly, $q'=q(0)+z/n$.

3.3 Focusing

The idea of focusing is to create a spatially varied phase front. Once a curved phase front is generated, together with the free propagation, a focusing effect occurs. Since the focusing must be related to the wavelength of the electric field and the focal length of the lens, the most direct guess would be a phase front of the format $\exp(ik_0x^2/2f)$ where f is the focal length. As a result, one can write the electric field after the focusing lens as

$$\begin{aligned}E(x)&=\exp(-ik_0x^2/2q(0))\exp(ik_0x^2/2f)\\ E(k_x)&=\mathscr{F}[E(x)]=\sqrt{\frac{-q(0)}{i\left[k_0-k_0q(0)/f\right]}}\exp\left[\frac{ik_x^2q(0)}{2k_0\left(1-q(0)/f\right)}\right]\end{aligned}$$

After propagating for distance z, one can write

$$\begin{aligned} E(x,z) = & \quad \mathscr{F}\left[E(k_x)\exp(ik_x^2 z/2k_0)\right] \\ = & \quad \sqrt{\frac{q(0)}{q(0)+z-zq(0)/f}}\exp\left\{\frac{-ix^2k_0\left[1-q(0)/f\right]}{2\left[q(0)+z-zq(0)/f\right]}\right\} \end{aligned} \tag{48}$$

From the exponential term, one can see that $q' = \left[q(0)+z(1-q(0)/f)\right]/\left[1-q(0)/f\right]$, which is also consistent with the ABCD matrix method.

3.4 Grating

For a grating, by defining the angle of incidence (γ), the output angle (θ) and angular dispersion, one can write

$$\Delta\theta = \alpha\Delta\gamma + \beta\Delta\omega \tag{49}$$

The partial derivative of the grating equation $\sin(\gamma) + \sin(\theta) = m\lambda/d$ leads to $\alpha = -\cos(\gamma_0)/cos(\theta_0)$, which is also the value of magnification of the beam size at the grating. For simplicity, α is set to 1 in this section. Besides, in this section, I focus on the frequency dependent angular dispersion to the first order. For higher orders, please see chapter 4. The electric field in the time domain and the pulse front tilt angle with respect to the propagation distance after the grating can be found in[55]. The electric field after the grating at the grating incidence surface is[56]

$$E(x,z) = a_1\exp\left(-ikx^2\alpha^2/2q(0)\right)\exp\left(ik\beta x\Delta\omega\right)$$

where the constant a_1 takes into account the amplitude for energy conservation. The propagation after the grating can be considered in two different ways. One is via the Huygens-Fresnel integral where each spatial point is considered as a point source and the final result of the propagation is the summation of the propagation from previous fields. The other is by solving the wave equation directly. One can see eventually that these two methods are equivalent.

Huygens-Fresnel principle: The illustration of the Huygens-Fresnel principle is shown in Fig. 4. In the following calculation, the y dimension is neglected for simplicity.

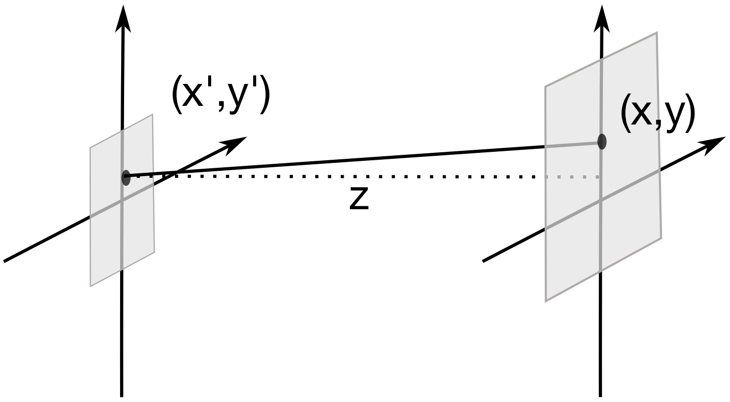

Figure 4: Illustration of the Huygens-Fresnel principle.

By setting $k = 2\pi/\lambda$, one can write the electric field after propagation distance z as the following

$$\begin{aligned} E(x,z) = & \frac{i}{\lambda z}\int_{-\infty}^{\infty} E(x',0)\exp\left(-ik\sqrt{(x-x')^2+z^2}\right)dx' \\ & \approx \frac{i}{\lambda z}\int_{-\infty}^{\infty} E(x',0)\exp\left[-\frac{ik}{2z}(x-x')^2\right]dx' \end{aligned} \quad (50)$$

Substituting $E(x',0) = \exp\left(-ikx'^2/2q(0)\right)$, Eq. (50) becomes,

$$E(x,z) = b_1\exp\left(\frac{-ikx^2}{2z}\right)\exp\left\{\frac{ikq(0)}{2z\left[q(0)+z\right]}\left(x+z\beta\Delta\omega\right)^2\right\} \quad (51)$$

where b_1 is a constant for energy conservation. It can be seen in Eq. (51) that the beam has a linear spatial chirp. If the distance z is large and is far larger than the beam size x', the phase term $ik(x-x')^2/2z \approx ik(x^2-2xx')/2z$. Consequently the far field diffraction can be written as Eq. (52) where the kx/z can be considered as k_x. Equation (52) shows the form of Fourier transform. This brings some insights into the far field diffraction. In another word, it means that the far field diffraction patten should be equivalent to the Fourier transform of the object e.g. pin hole, slit, etc..

$$E(x,z) = \frac{i}{\lambda z}\exp\left(-ikx^2/2z\right)\int_{-\infty}^{\infty} E(x',0)\exp\left(ikxx'/z\right)dx' \quad (52)$$

Directly solve the wave equation: By solving the wave equation as the following

$$-2ik\frac{\partial E(x,z)}{\partial z} + \frac{\partial^2 E(x,z)}{\partial x^2} = 0$$

one can obtain the analytical result as shown in Eq. (54).

$$\begin{aligned} E(x,z) &= \mathscr{F}\left[E(kx,0)\exp\left(\frac{ik_x^2 z}{2k}\right)\right] && (53)\\ &= b_1\exp\left\{\frac{-ik}{2\left[z+q(0)\right]}\left[q(0)\beta\Delta\omega - x\right]^2\right\}\exp\left[iq(0)\beta^2(\Delta\omega)^2 k/2\right] && (54)\end{aligned}$$

After some simply algebra, one can easily see that Eq. (54) and Eq. (51) are identical. This is not a surprising result, since one can already see that Eq. (53) and Eq. (50) are identical. The convolution is equivalent to a direct multiplication in the Fourier domain.

Continue with Eq. 51, if a second grating is added which resembles the case of a compressor, the role of γ and θ are interchanged ($\Delta\gamma = -\beta\Delta\omega/\alpha + \Delta\theta/\alpha$). Thus, the electric field after the second grating yields

$$\begin{aligned} E(x,z) = &\quad b_1\exp\left(\frac{-ikx^2}{2z}\right)\exp\left\{\frac{ikq(0)}{z\left[q(0)+z\right]}\left(x+z\beta\Delta\omega\right)^2\right\}\exp\left(-ik\beta\Delta\omega x/\alpha\right)\\ = &\quad b_1\exp\left\{\frac{ik}{2\left[q(0)+z\right]}\left(x+z\beta\Delta\omega\right)^2\right\}\exp\left[ik\beta^2(\Delta\omega)^2 z/2\right]. && (55)\end{aligned}$$

By propagating Eq. (55) after distance z', one can get the following

$$E(x,z+z') = b_1\exp\left\{\frac{ik}{2\left[q(0)+z+z'\right]}\left(x+z\beta\Delta\omega\right)^2\right\}\exp\left[ik\beta^2(\Delta\omega)^2 z/2\right] \qquad (56)$$

where z is the distance between two gratings and z' is the distance after the second grating. The phase term is

$$\phi(\omega) = \frac{ik\beta^2(\Delta\omega)^2 z}{2} - \frac{ik(z+z')(2xz\beta\Delta\omega + \beta^2(\Delta\omega)^2 z^2)}{\left[(z+z')^2 + \pi^2\sigma^4/\lambda^2\right]}$$

The first term gives the phase term quadratic in frequency, which accounts for the desired group delay dispersion. The second term is undesirable because it depends on the propagation distance after the second grating i.e. z'. If

$$(z+z')z/\left[(z+z')^2 + \pi^2\sigma^4/\lambda^2\right] \ll 1$$

$$\therefore z \ll \pi\sigma^2/\lambda$$

Equation 56 can be rewritten as

$$E(x, z + z') = b_1 \exp\left[-\left(x + z\beta\Delta\omega\right)^2/\sigma^2\right]\exp\left[ik\beta^2(\Delta\omega)^2 z/2\right].$$

Thus, after the compressor, the linear spatial chirp is $z\beta\Delta\omega$ and the group delay dispersion induced is $2k\beta^2 z$.

Part II

Terahertz generation in tilted-pulse-front setup

4 Full 3D+1 (x,y,z,t) numerical model

Section 4 is published in the work done by L. Wang et.al.[57].

4.1 Introduction

Single- to few-cycle (broadband) high energy terahertz pulses have many promising applications such as spectroscopy[5], strong field terahertz physics[6;7], particle acceleration[8], electron spin manipulation[6] and phonon resonance studies[9]. All of these applications require well-characterized terahertz fields.

There are many possible ways to generate terahertz radiation. Free electron lasers and synchrotron radiation have a high degree of tunability and are capable of delivering high peak power coherent terahertz pulses[16]. Gyrotrons, based on the principle of electron cyclotron radiation, are able to generate watt-to-megawatt-level terahertz continuous wave radiation[17] at low terahertz frequencies (0.3-1.3 THz)[18;19]. These devices, however, have limited accessibility to the larger scientific community, and can be difficult to synchronize to laser sources with high (fs) precision.

Alternatively, single- to few-cycle terahertz generation, based on table-top optical laser systems, brings the advantages of high accessibility and intrinsic synchronization, but suffers from limited optical-to-terahertz conversion efficiency. This synchronization is required for terahertz electron acceleration. Laser based terahertz generation typically falls into three categories. One, using electrically-charged photoconductive antennas[29;30], excitation of semiconductors by an ultrashort pulse and subsequent radiation of a sub-picosecond pulse[31] forms transient photocurrents. The emitted terahertz pulse properties are determined by the carrier lifetime of the material, the applied voltage and the breakdown threshold[32]. The second category is based on laser-induced plasma in air or noble gases. Here, the incident optical pulse induces a ponderomotive force which causes a charge separation between ions and electrons, leading to the emission of a terahertz pulse[33;34], with peak electric fields that can reach as high as a few MV/cm[35]. However, the terahertz frequency, spatial distribution and polarizability are strongly related to the plasma density, plasma length, and plasma defocusing effect[36;37], which can be difficult to control. Difference frequency generation or optical rectification is the third category. By utilizing the second-order nonlinear effect, an ultrashort pump laser pulse induces a strong dipole moment. The dipole oscillation together with the repeated energy down conversion of pump photons (cascading effect) leads to terahertz pulse emission with an efficiency close to, or even above, the Manley-Rowe limit[58]. Using the well-known "tilted-pulse-front" (TPF) technique, first proposed and demonstrated by J.Hebling et.al.[59], pulse energies in the millijoule range can be reached[60]. The ease of this setup, the high pulse energies and the controllability of the terahertz properties has made this last approach an ubiquitous one for high-field applications. However, the non-collinear geometry of the phase matching and the spatial asymmetry of the interaction, in combination with the cascading effect, result in terahertz beams with non-uniform spatial distribution. A robust 3D+1 numerical tool is therefore necessary to investigate the spatial and temporal properties of the generated terahertz fields.

4.2 Theoretical model

The setup modelled and simulated is shown in Fig.5. The often used nonlinear materials are $LiNbO_3$, CdTe, GaAs, GaSe, GaP and ZnTe. Here, I focus on $LiNbO_3$ (LN for short) due to its large second-order nonlinear coefficient, high damage threshold and easy accessibility. The results however can be extended to other materials. A two-lens imaging system is analyzed here instead of the one-lens system, because the imaging errors and terahertz divergence are reduced, both of which favor the terahertz generation process[61]. In this article, I focus on the impact of the optical pump (OP) beam size on the properties of the generated terahertz beam.

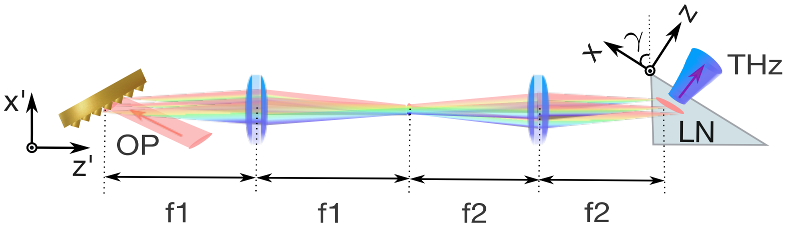

Figure 5: Illustration of the simulated tilted-pulse-front setup. The optical pump pulse is noted by OP and the $LiNbO_3$ crystal is represented by LN. The OP propagates along the z' direction. The $x-y-z$ coordinates denote the pulse-front-tilt frame (terahertz frame) inside the LN-crystal. The y and y' axes are equivalent.

First, I show analytically that, regardless of the noncollinear phase matching and the prism geometry, the second order dispersion generated by the grating can already cause inhomogeneity of the terahertz pulses (see Eq. (60)). I start from the grating relation $\sin(\theta_1)+\sin(\theta_2) = 2\pi c/\omega d$, where θ_1 and θ_2 are the incidence and output angles with respect to the normal of the grating surface respectively. The optical frequency is represented by ω while d denotes the grating groove period. Assuming that the input OP is collimated ($d\theta_1/d\omega = 0$), one can get Eq. (57).

$$\begin{cases} \dfrac{d\theta_2}{d\omega} = \dfrac{-2\pi c}{\omega^2 d\cos(\theta_2)} \\ \dfrac{d^2\theta_2}{d^2\omega} = \dfrac{4\pi c}{\omega^3 d\cos(\theta_2)} - \dfrac{2\pi c\sin(\theta_2)}{\omega^2 d\cos^2(\theta_2)}\dfrac{d\theta_2}{d\omega} \end{cases} \tag{57}$$

One can obtain the angular dispersion $\Delta\theta_2$ with respect to the OP propagation direction, via performing a Taylor expansion to the second order. By inserting Eq. (57) and setting the first order angular dispersion $F_1 = -2\pi c/(\omega_0^2 d\cos(\theta_{02}))$ where ω_0 is the center frequency and θ_{02} is the grating output angle at the center frequency, I obtain:

$$\begin{aligned}\Delta\theta_2 \quad &= \frac{d\theta_2}{d\omega}|_{\omega=\omega_0}(\omega-\omega_0) + \frac{1}{2}\frac{d^2\theta_2}{d^2\omega}|_{\omega=\omega_0}\Delta(\omega-\omega_0)^2 \\ &= F_1\,(\omega-\omega_0) + \left[-F_1/\omega_0 + \frac{1}{2}F_1^2\tan(\theta_{02})\right](\omega-\omega_0)^2 \\ &= F_1\,(\omega-\omega_0) + F_2(\omega-\omega_0)^2 \qquad (58)\end{aligned}$$

The second order dispersion is denoted by F_2. After the propagation through the telescope system, the angular dispersion is magnified by a factor of -f_1/f_2. Thus, the angular dispersion becomes $-\Delta\theta_2 f_1/f_2$. Note that the transverse k-vector $k_{x'0}(\omega) = -\Delta\theta_2 f_1\omega_0/(cf_2)$ remains the same before and after entering the LN-crystal due to the Fresnel law. As a result, by assuming $k_{z'0}(\omega) \approx \omega n(\omega)/c$, where n is the refractive index, the OP electric field inside the LN-crystal is given in Eq. (59) in the $x'-y'-z'$ coordinates. In Eq. (59), the pulse duration is $\tau = \tau_0/\sqrt{2\log 2}$, A_0 is the electric field amplitude and σ'_x, σ'_y are beam waists (1/e) of the OP at the incidence surface of the LN-crystal in x' and y' dimensions respectively.

$$\begin{aligned}E(\omega,x',y',z') = \quad & A_0\exp\left[-(\omega-\omega_0)^2\tau^2/4\right]\exp\left[-x'^2/(2\sigma_x'^2)\right]\exp\left[-y'^2/(2\sigma_y'^2)\right] \\ & \times\exp\left[-i\omega n(\omega)z'/c\right]\exp\left[i\Delta\theta_2 f_1\omega_0 x'/(cf_2)\right] \qquad (59)\end{aligned}$$

The imaging system was chosen such that the image of the grating is parallel to the pulse-front-tilt plane inside the nonlinear crystal[62]. The expression of the OP electric field given in Eq. (59), is only valid at the imaging plane of the telescope. It is very important to notice that the higher order angular dispersion (F_2) induced by the grating leads to temporal broadening of the OP[56;63], as it adds nonlinear phase (see Eqs. (58) and (59)). If the second order angular dispersion is neglected ($F_2 = 0$ in Eq. (58)), the OP pulse duration reduces to the transform limited case at each spatial point along the x' dimension.

Using Eq. (59), the second order polarization which is responsible for the terahertz generation can be expressed as in Eq. (60), where γ is the angle between the terahertz pulse propagation direction and the OP propagation direction, $\chi^{(2)}$ is the second order nonlinear susceptibility and Ω is the terahertz angular frequency. The group refractive index at the center frequency of the optical pump is denoted by n_g.

$$\begin{aligned}
P_{NL}^{(2)}(\Omega, x', y', z') = \quad & -\chi^{(2)} \frac{\Omega^2}{c^2} \int_0^{\infty} E(\omega + \Omega, x', y', z') E^*(\omega, x', y', z') d\omega \\
& \times \exp\left\{ i\Omega n(\Omega)[\cos(\gamma) z' + \sin(\gamma) x']/c \right\} \\
= \quad & -\chi^{(2)} \frac{\Omega^2 \sqrt{2\pi}}{\tau c^2} A_0^2 \exp\left(\frac{-x'^2}{\sigma_x'^2} \right) \exp\left(\frac{-y'^2}{\sigma_y'^2} \right) \\
& \times \exp\left(-\frac{\Omega^2 \tau^2}{8} \left\{ 1 + \frac{16 x'^2 n_g^2 \tan(\gamma)^2}{\tau^4 c^2} \left(\frac{F_2}{F_1} \right)^2 \right\} \right) \\
& \times \exp\left\{ -i\frac{\Omega}{c} \Big[n_g - n(\Omega)\cos(\gamma) \Big] z' \right\} \exp\left\{ i \Big[\frac{f_1 \omega_0}{f_2} F_1 + n(\Omega)\sin(\gamma) \Big] \frac{\Omega}{c} x' \right\}
\end{aligned} \tag{60}$$

The last two exponential phase terms in Eq. (60) represent the phase matching condition.

$$\begin{cases}
\Delta k_z' = \dfrac{\Omega}{c} \Big[n_g - n(\Omega)\cos(\gamma) \Big] = 0 \rightarrow n_g / n(\Omega) = \cos(\gamma) \\
\Delta k_x' = \Big[\dfrac{f_1 \omega_0}{f_2} F_1 + n(\Omega)\sin(\gamma) \Big] \dfrac{\Omega}{c} = 0 \rightarrow \dfrac{2\pi c f_1}{d \cos(\theta_2) \omega_0 n_g f_2} = \tan(\gamma)
\end{cases}$$

The term in the third exponential ($(F_2/F_1)^2\, 16x'^2 n_g^2 \tan(\gamma)^2/\tau^4 c^2$) is due to the second order angular dispersion which has been discussed in more detail in[64]. It can be seen that the second order angular dispersion leads to a spatial dependence of the generated terahertz bandwidth along the x' dimension. At the center of the pump pulse ($x' = 0$), the generated terahertz pulse possesses its largest bandwidth. However, towards the sides of the OP beam, the bandwidth of the terahertz pulse reduces. In other words, due to the second order angular dispersion ($(\omega - \omega_0)^2$ related term), the OP experiences a temporal chirp and thus, the pulse duration varies with respect to x'. The effective instantaneous bandwidth of the OP reduces towards the sides of the beam, leading to a narrower terahertz spectrum (multi-cycle pulses).

4.3 Comparison of the 1D+1, 2D+1 and 3D+1 simulations

Owing to the geometry of the LN-crystal, the interaction length varies with respect to x'. Since the generated terahertz pulses act back on to the OP, cascading occurs. This causes a spatially dependent OP spectrum, which further enhances spatial inhomogeneities of the generated terahertz pulses. Furthermore, at the desired terahertz frequency range (<4 THz), the material absorption (α) increases with respect to frequency. This favors lower terahertz frequencies towards the base of the LN-crystal due to longer interaction length. The aforementioned aspects can only be investigated by a robust numerical model.

The numerical model solves the coupled wave equations with slowly varying amplitude approximation in the terahertz coordinates (x-y-z). By setting the electric field of the OP $\mathscr{F}[E_{\text{op}}(t,x,y,z)] = E_{\text{op}}(\omega,x,y,z) = E(\omega,x,y,z)e^{-i[k_{z0}(\omega)z+k_{x0}(\omega)x]}$, and the electric field of the terahertz $\mathscr{F}[E_{\text{THz}}(t,x,y,z)] = E_{\text{THz}}(\Omega,x,y,z) = E(\Omega,x,y,z)e^{-ik_0(\Omega)z}$ respectively, one can get Eqs. (61) and (62). The operator $\mathscr{F}$ represents the Fourier transform.

$$\begin{aligned}
-2ik_0(\Omega)\frac{\partial E(\Omega,x,y,z)}{\partial z} &= -[\underbrace{\overbrace{\frac{\partial^2}{\partial y^2}}^{\text{neglected by 2D+1}}+\frac{\partial^2}{\partial x^2}}_{\text{neglected by 1D+1}} - i\alpha k_0(\Omega)]E(\Omega,x,y,z)\\
&\quad -\frac{\Omega^2\chi^{(2)}}{c^2}\int_{-\infty}^{\infty}E(\omega+\Omega,x,y,z)E^*(\omega,x,y,z)e^{i(\Delta k_z z+\Delta k_x x)}d\omega
\end{aligned} \tag{61}$$

$$\begin{aligned}
-2ik_{z0}(\omega)\frac{\partial E(\omega,x,y,z)}{\partial z} &= -[\underbrace{\overbrace{\frac{\partial^2}{\partial y^2}}^{\text{neglected by 2D+1}}+\frac{\partial^2}{\partial x^2} - 2ik_{x0}(\omega)\frac{\partial}{\partial x}}_{\text{neglected by 1D+1}}]E(\omega,x,y,z)\\
-\varepsilon_0 n^2(\omega_0)\frac{\omega^2}{c}\mathscr{F}&\left\{E_{\text{op}}(t,x,y,z)\int_{-\infty}^{\infty}n_2(\tau)E_{\text{op}}^2(t-\tau,x,y,z)d\tau\right\}e^{i[k_{z0}(\omega)z+k_{x0}(\omega)x]}\\
&\quad -\frac{\omega^2\chi^{(2)}}{c^2}\int_{-\infty}^{\infty}E(\omega+\Omega,x,y,z)E^*(\Omega,x,y,z)e^{i(\Delta k_z z+\Delta k_x x)}d\Omega
\end{aligned} \tag{62}$$

In Eqs. (61) and (62), $\Delta k_x = k_{x0}(\omega) - k_{x0}(\omega+\Omega)$, $\Delta k_z = k_{z0}(\omega) - k_{z0}(\omega+\Omega) + k_0(\Omega)$. The $\chi^{(2)}$ related terms are responsible for the second order nonlinear effects, i.e., the terahertz generation and back conversion processes. In Eq. (62), the third-order nonlinear effects, including self-phase-modulation, self-steepening and stimulated Raman effect, are represented by the term $n_2(\tau) = \mathscr{F}[n_2(\omega-\omega_0)]$[42]. The phonon resonances at terahertz frequencies[49] are implemented by considering the stimulated Raman effect at the optical frequency region together with the frequency-dependent refractive index in the terahertz frequency region. In the simulation, frequency dependent refractive index and the terahertz absorption are used. The parameters used in simulations are listed in Table.2. The peak fluence of the OP at the input LN-crystal surface is chosen to be right beneath the estimated damage threshold 70.7 mJ/cm^2 based on our previous studies[65].

Table 2: Simulation parameters

Parameters	**Value**	**Parameters**	**Value**
focal length f_1	300 mm	focal length f_2[61]	$0.613 \times f_1$ mm
wavelength λ	1030 nm	grating period d	1/1500 mm
pulse duration τ_0 (FWHM)[66]	0.5 ps	peak fluence[65]	$10^8 \sqrt{\tau_0}$ mJ/cm^2
phase-matching frequency	0.3 THz	absorption coefficient $\alpha(300\,\mathrm{K}, 0.3\,\mathrm{THz})$[51]	7/cm

By comparing different models, one can see that the 1D+1 calculation neglects diffraction effects and, more importantly, the spatial walk-off between the terahertz and OP beams (the operator $2ik_{x0}\frac{\partial}{\partial x}$). The neglected terms are marked in Eqs. (61) and (62) by "neglected by 1D+1". Figure 6 suggests that, by neglecting any spatial walk-off effect, the 1D+1 model overestimates the OP spectral broadening leading to a more pronounced stimulated Raman effect. Consequently, higher terahertz frequencies can be generated within the OP bandwidth via difference-frequency generation. This explains why the 1D+1 model predicts higher terahertz frequency content as compared to the 3D+1 model shown in Fig. 2(b). The 2D+1 model, though neglecting diffraction in the dimension y (labeled by "neglected by 2D+1"), captures the broadening of the OP spectrum better than the 1D+1 case. Accordingly, the terahertz spectrum is predicted in very good agreement with the 3D+1 model.

Figure 6(c) shows the computed conversion efficiency along the terahertz propagation direction (z). As can be seen, the 1D+1 model drastically underestimates the optimal interaction length, which also leads to a significant overestimation of the conversion efficiency. The interaction length is captured better by the 2D+1 model, while the conversion efficiency is still overestimated by about 25% compared to the value obtained by a 3D+1 calculation, since the reduction of the OP fluence along the y dimension is not accounted for in this model and only properly captured in the 3D+1 case.

It can be concluded that in order to capture the key characteristics of the OP and terahertz spectra, at least a 2D+1 model should be used while for a proper prediction of the conversion efficiency both 1D+1 and 2D+1 model overestimate the efficiency significantly. Here, a 3D+1 model is recommended.

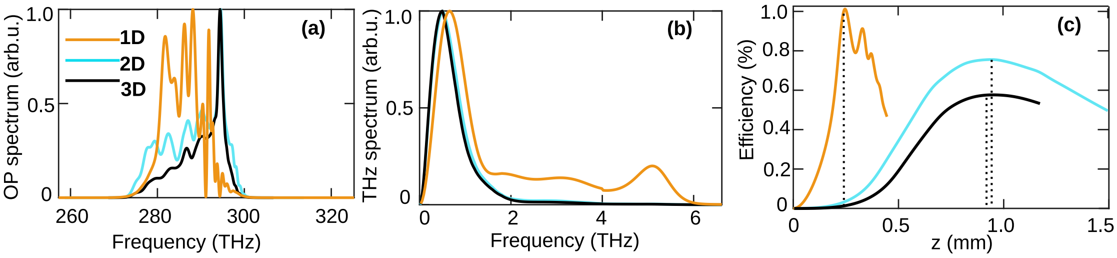

Figure 6: Comparison of the results obtained from 1D+1, 2D+1 and 3D+1 simulations. (a), (b) and (c) are the output OP spectra, the output terahertz spectra and the efficiencies respectively. (a) and (b) are plotted at the location of maximum efficiency.

4.4 Spatial dependence of the terahertz electric field

Without loss of generality, the nonlinear interaction between the OP and the LN-crystal is numerically implemented in the $x-y-z$ coordinate frame where $x=0$ represents the apex location of the LN-crystal. Note that the OP beam size in the $x-y-z$ coordinates $\sigma_x{=}\sigma_{x'}/\cos(\gamma)$ is due to the projection onto the plane of the tilted pulse front. The simulations suggest that within an OP beam size range $\sigma_y = [0.5, 4.5]$ mm (not shown), diffraction has a negligible effect on the terahertz generation process and the terahertz beam size scales as $\sigma_y/\sqrt{2}$. This agrees well with the analytic result in Eq. (60). In the following simulations, σ_y is chosen to be 3.5 mm.

In Fig. 7, the maximum terahertz generation efficiency is plotted against the OP beam size $\sigma_{x'}$ for two different OP peak fluences. For this calculation, the 2D+1 model is chosen due to the high computational cost of the 3D+1 model.

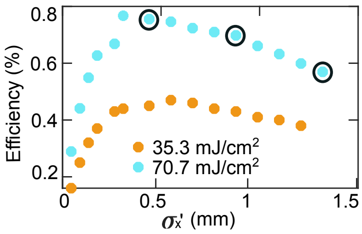

Figure 7: With the input pump fluence 70.7 mJ/cm^2 (blue dots) and 35.3 mJ/cm^2 (orange dots), the maximum terahertz generation efficiencies versus the OP beam size $\sigma_{x'}$, calculated by the 2D model, are presented. The black circles indicate 3 beam sizes chosen as examples in the following 3D+1 calculations.

Due to the nature of the non-collinear phase-matching condition, the terahertz generation process requires different sections of the beam along the x dimension to add up coherently in the emission direction z. In contrast with the OP beam size in the y dimension, a small beam size along the x dimension cannot produce high generation efficiencies due to the walk-off between the OP and the terahertz beam. On the other hand, if the beam size is too large, the terahertz radiation generated by the side of the OP at the farther side from the LN-crystal apex suffers from more absorption compared to the part closer to the apex. Thus, the generation efficiency shows a maximum as a function of OP beam size in the x'-direction. Additionally, since lower pump fluence leads to longer interaction length, the optimal pump beam size increases (see the orange dots in Fig. 7).

As in experiments different OP beam sizes may be required in order to optimize the use of the available pump energy and limited crystal aperture, I select three pump sizes ($\sigma_{x'}$ = 0.44mm, 0.88mm and 1.32 mm, marked by black circles in Fig. 7) for studying the spatio-temporal properties of the terahertz field using the 3D+1 model.

In order to compare the terahertz fields generated by different spatial positions of the OP beam, the center of the OP (highest peak fluence $y = 0$) and the side region of the OP (low fluence, $y = \sigma_y/\sqrt{2} = 2.47\,\text{mm}$) within the optical beam are chosen. Figures 8(a)-8(f) show the OP and the terahertz beam profiles at the output LN-crystal surface with different input OP beam sizes. For the beam sizes $\sigma'_x = 0.44\,\text{mm}$,0.88 mm and

1.32 mm, the conversion efficiencies are 0.57%, 0.54%, 0.46% respectively. Figures 8(g)-8(i) present the fluence of the OP at $y = 0$ and $y = \sigma_y/\sqrt{2}$ with the center of the OP marked by the dashed lines. The fluence distribution indicates an energy shift towards the base of the LN-crystal. This shift is due to the non-collinear nature of the phase-matching mechanism, which causes the new optical frequencies of the OP, generated via the cascading effect, to propagate towards the base of the crystal. Surprisingly, the size of the OP does not strongly influence the size of the generated terahertz beams. Towards the base of the LN, the interaction length increases, the terahertz absorption and the nonlinear effect become more pronounced. The terahertz fields generated close to the base are absorbed before they reach the output LN surface. Thus, for large OP beam sizes, the OP farther from the LN apex is wasted. Figures 8(j)-8(l) indicate that at a given OP beam size, a higher pump fluence leads to a smaller terahertz beam size compared with the case using a lower pump fluence. This finding agrees with the experimental results of C. Lombosi et al.[67]. The terahertz beams are found to be symmetric along the y dimension.

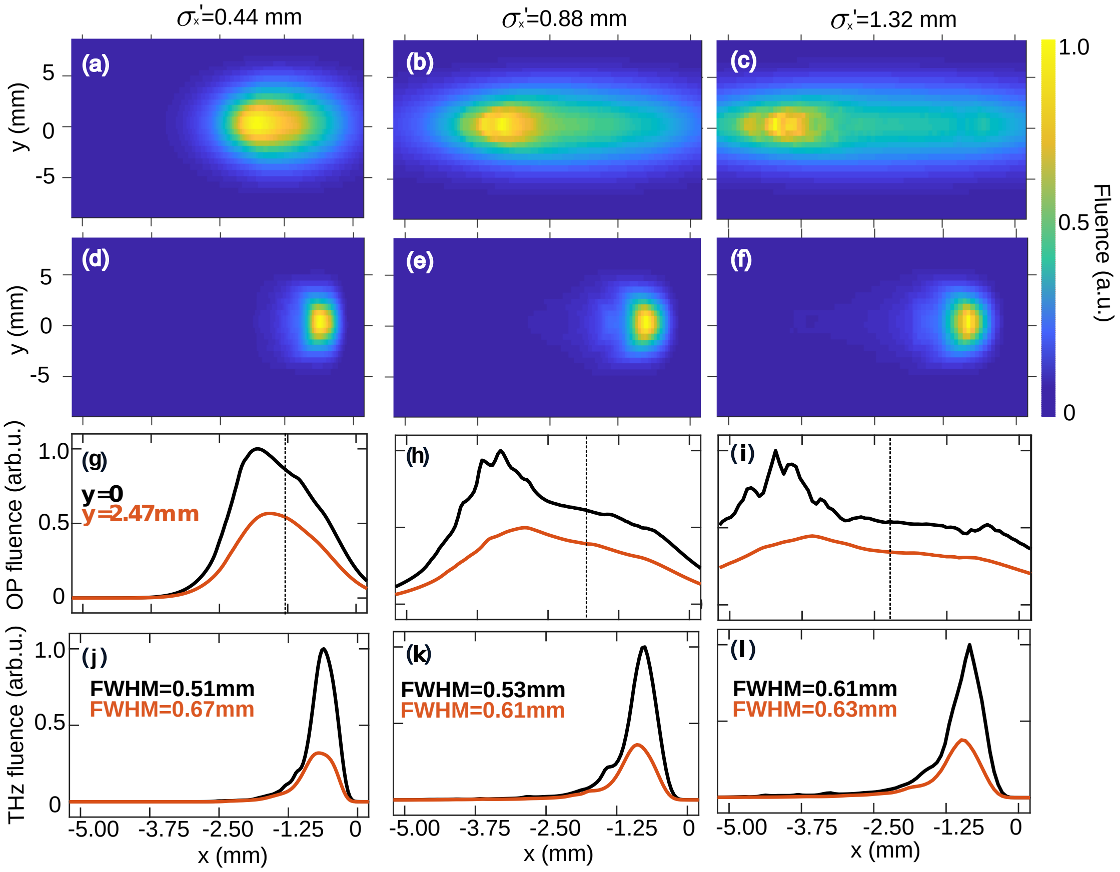

Figure 8: Spatial dependence of the generated terahertz beams along x and y dimensions. (a-c) and (d-f) represent the OP and the terahertz beam profiles at the output surface of the LN-crystal respectively. (g-i) and (j-l) represent the OP and terahertz fluence respectively at a given position $y = 0$ (black curve) and $y = \sigma_y/\sqrt{2} = 2.47$ (red curve). The OP beam sizes at the input LN-crystal surface are $\sigma_x' = 0.44\,\text{mm}$, $0.88\,\text{mm}$ and $1.32\,\text{mm}$ in $x' - y' - z'$ frame respectively. The center position of the OP beam is marked by the dashed line. The OP beam size in the y dimension is $\sigma_y = 3.5\,\text{mm}$. The apex of the LN-crystal is located at $x = 0$.

Figures 9(a)-9(c) and Figs. 9(g)-9(i) show the spatially dependent electric fields at $y = \sigma_y/\sqrt{2}$ and $y = 0$ respectively, with the corresponding terahertz spectra shown in Figs. 9(d)-9(f) and Figs. 9(j)-9(l). It can be seen that the few-cycle terahertz electric fields are only generated at the vicinity of the apex of the LN-crystal. This effect is seen to increase with larger pump beam sizes, as a larger fraction of the terahertz is generated farther from the apex and the terahertz electric fields deviate from a single-cycle waveform.

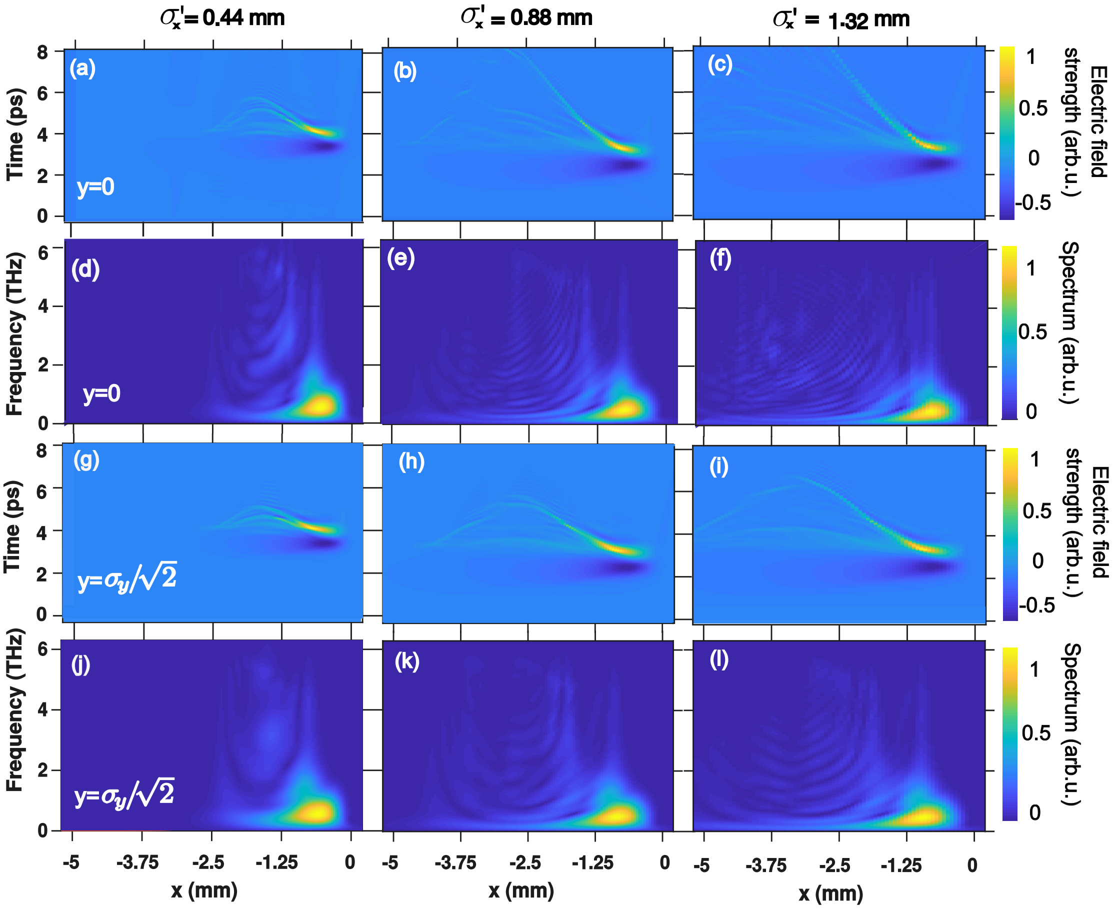

Figure 9: Spatial dependence of the generated terahertz spectra and temporal profiles along the x dimension. (a-c) and (d-f) are the terahertz electric fields and the corresponding terahertz spectra with respect to x at $y = 0$. (g-i) and (j-l) are the terahertz electric fields and the corresponding terahertz spectra with respect to x at $y = \sigma_y/\sqrt{2}$.

To quantify the deviation from a single-cycle waveform, the root-mean-square pulse duration Δt is chosen to evaluate the electric field distribution (see Eq.63)). In Eq. (63), $\delta t = |t(x, y) - t(x, y)_p|$, $t(x, y)_p$ is the time coordinate of the peak of the electric field at position (x, y) and I represents the intensity. The reference $\Delta t(x_p, y_p)$ is chosen at the position (x_p, y_p) where the terahertz peak fluence is located.

$$\Delta t(x,y) = \sqrt{\frac{\int [\delta t(x,y)]^2 I(t,x,y)dt}{\int I(t,x,y)dt} - \left[\frac{\int \delta t(x,y) I(t,x,y)dt}{\int I(t,x,y)dt}\right]^2} \tag{63}$$

The resulting map of $\Delta t(x,y)$ can be used to determine the portion of the terahertz beam, where the electric field deviates significantly from a single-cycle format (see Fig. 10). Figure 10 shows the terahertz beam generated by an OP with $\sigma_x = 1.32$mm, where the part with $\Delta t(x,y) > 2\Delta t(x_p, y_p)$ is shaded grey to indicate the non-single-cycle content.

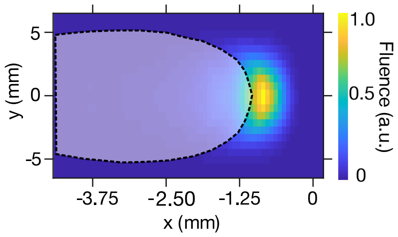

Figure 10: The example shown is for $\sigma'_x = 1.32$ mm, where the non-single-cycle region, $\Delta t(x,y) > 2\Delta t(x_p, y_p)$, is indicated by the shaded region. The terahertz beam under the shaded region contains up to 25% of the total terahertz energy.

The shaded region in Fig. 10 shows that high quality few-cycle pulses are only generated close to the apex of the crystal ($x = 0$). The terahertz beam profiles are symmetric along the y-direction. I find that, even though higher pump fluence ($y = 0$) leads to a higher terahertz energy, the portion of non-single-cycle content in the beam increases. It can be seen from Fig. 9 and Fig. 10 that the side of the OP beam (for example $y = \sigma_y / \sqrt{2}$ mm) possesses lower fluence, which leads to less OP spectral broadening in the terahertz generation process. Such a less broadened OP spectrum leads to a relatively homogeneous terahertz distribution along the x dimension. For $\sigma_{x'} = 0.44$ mm, 0.88 mm and 1.32 mm the $\Delta t(x,y) > 2\Delta t(x_p, y_p)$ region (shaded region) take up 4%, 20% and 25% of the total terahertz energy respectively. It can be seen that, with the increase of the OP beam size, the single-cycle region of the generated terahertz pulses reduces significantly. Additionally, due to the geometry of the nonlinear crystal, it is inevitable that the generated terahertz possesses a spatial inhomogeneity. In order to resolve this problem, a setup which combines a conventional tilted-pulse-front setup and a transmission stair-step echelon is promising to generate spatially homogeneous terahertz pulses[68].

5 2D+1 numerical simulations for different TPF schemes

Section 5 is published in the work done by L. Wang et.al.[69].

5.1 Introduction

Optical rectification is used for terahertz generation where an ultrashort pump laser pulse induces a strong dipole moment via the second-order nonlinear effect. Due to the terahertz absorption of the nonlinear material, limited damage threshold of the nonlinear material and the low terahertz photon to pump photon energy ratio, generating high energy terahertz pulses is extremely challenging. The "tilted-pulse-front" (TPF) technique, a velocity matching method for terahertz generation by optical rectification, brings new possibilities to the generation of high energy terahertz pulses. In this technique, the intensity front of the optical pump is tilted with respect to the phase front[70]. The generated terahertz propagates perpendicularly to the tilted pulse front.

Many approaches have been proposed related to the TPF technique in order to achieve efficient single- to few-cycle terahertz generation. In this section, I present analyses of five characteristic examples. The conventional TPF technique is proposed and demonstrated in 2002 by J. Hebling et.al.[59], where a diffraction grating induces angular dispersion onto the optical pump pulse, forming a pulse front tilt. Shortly after, in 2004, the pulse front tilt caused by spatio-temporal chirp (STC) is proposed by S. Akturk et.al.[71]. The pulse front tilt is generated by propagating a spatially chirped optical pulse through a dispersive medium. In this method, no angular dispersion occurs. However, this method was not used to generate terahertz pulses until 2019 when the analytic results were investigated by K. Ravi[64]. In 2016, BK. Ofori-Okai et.al.[72] demonstrated a stair-step reflective echelon (RES) structure. The echelon produces a discretely tilted pulse front, eliminating the negative effect of large angular dispersion[72]. In 2017, a multistep phase mask (MSPD) scheme is proposed by Y. Avetisyan et.al.[73]. This scheme splits a single input beam into many smaller time-delayed "beamlets". Compared with the grating method, it reduces the angular dispersion and eliminates the necessity of the imaging optics. In the same year, L. Pálfalvi et.al. performed numerical studies of a nonlinear echelon (NLES) slab[68], where a stair-step echelon-faced nonlinear crystal is used instead of a nonlinear prism. This scheme produces good-quality, symmetric terahertz beams. The corresponding experiment is demonstrated by PS. Nugraha et.al. in 2019[74].

Simulations of terahertz generation with the conventional grating (CG) scheme have been developed by M. I. Bakunov et al.[75;76] via a 2D+1 numerical model. However, this model doesn't include back conversion of the terahertz to the optical pump (OP), i.e. the cascading effect. Consequently, the effective length and conversion efficiency are overestimated. Later on, the interaction between the optical pump and the terahertz pulse was included in the 2D+1 model along with a one lens imaging system by K. Ravi et al.[77]. The one-lens imaging system has larger imaging errors and induces more terahertz divergence[61], compared with the telescope imaging system. A full 3D+1 numerical model with a telescope system is developed by L. Wang et.al.[57].

In this part, I focus on the 2D+1 model. The terahertz conversion efficiency, the spatial distribution of the terahertz electric field and spectrum are discussed. Furthermore, the advantages and disadvantages of each TPF scheme are analyzed. As far as we know, no work has been done related to the comparison of different TPF schemes. The results bring insights into the terahertz generation process and can give useful and clear guidance to terahertz related experiments in the future.

In order to investigate the terahertz spatial and temporal electric field distribution, a 3D+1 model is necessary. However, from section 4, one can see that the 2D+1 calculation is a good approximation. In the following sections, I confine our numerical calculations to the 2D+1 model due to the relatively low computational cost. The numerical tool is based on the fast Fourier transform beam propagation method (FFT-BPM)[78] and the split-step Fourier method. The combination of these two methods reduces computational cost compared to the finite difference time-domain (FDTD) method which is very accurate but requires a massive computational effort. The polarization terms are calculated in the frequency domain. The entire electric field is updated by the 4th order Runge-Kutta in the propagation direction of the terahertz (z). The apex of the LN is located at $x = 0$. The $z = 0$ coordinate is defined is defined at the location where the center of the OP starts to interact with the LN crystal. Two OP beam sizes $\sigma_x' = 0.5$ mm and $\sigma'_x = 4mm$ are chosen as examples, where σ'_x is the OP beam size at the LN input surface. The analytical results are shown with the assumption that each beamlet is of Gaussian shape. In the numerical calculation, the beamlets maintain the shape of the overall Gaussian envelope.

The out-coupling loss is calculated by Fourier transforming the terahertz fields into the reciprocal domain (k_x). With the terahertz incidence angle at the LN output surface $\theta = \sin^{-1}[k_x(\Omega)/k(\Omega)]$, the transmission of the Fresnel law is calculated for every single frequency.

In this section, the analytical expressions of the electric field at the LN input surface and the corresponding second order polarization are given. Apart from the spatial-temporal chirp (STC) scheme, the input OP in the OP propagation frame can be defined as Eq. (64), where σ' is the input OP beam size before the optical system, $\Delta\omega = \omega - \omega_0$ and σ'_x in Table. 3 is the OP beam size at the LN input surface i.e after optical elements and the imaging system.

$$E(\omega, x', z') = E_0 \exp\left(\frac{-\Delta\omega^2\tau^2}{4}\right)\exp\left(\frac{-x'^2}{2\sigma'^2}\right)\exp(-i\omega z'/c). \tag{64}$$

With the ansatz of the terahertz electric field

$$E(\Omega, x', z') = A(\Omega, x', z')\exp\left[-i\Omega n_t \sin(\gamma)x'/c\right]\exp\left[-i\Omega n_t \cos(\gamma)z'/c\right]$$

, where γ is the propagation direction of the terahertz pulse with respect to the OP inside the LN i.e. the phase matching angle. The wave equation for terahertz generation can be written in the form of Eq. (65) where the corresponding second order polarization is defined in Eq. (66).

$$\begin{aligned}&\frac{\partial^2 A(\Omega, x', z')}{\partial x'^2} + \frac{\partial^2 A(\Omega, x', z')}{\partial z'^2} - \frac{2i\Omega n_t \cos(\gamma)}{c}\frac{\partial A(\Omega, x', z')}{\partial z'}\\ &-\frac{2i\Omega n_t \sin(\gamma)}{c}\frac{\partial A(\Omega, x', z')}{\partial x'} = -\frac{\Omega^2}{c^2}P(\Omega, x', z')\end{aligned} \tag{65}$$

$$\begin{aligned}&P(\Omega, x', z') = \chi^{(2)}\int_0^\infty E(\omega + \Omega, x', z')E^*(\omega, x', z')d\omega\\ &\times\exp\left[i\Omega n_t \sin(\gamma)x'/c\right]\exp\left[i\Omega n_t \cos(\gamma)z'/c\right]\end{aligned} \tag{66}$$

5.2 (a) Conventional grating (CG)

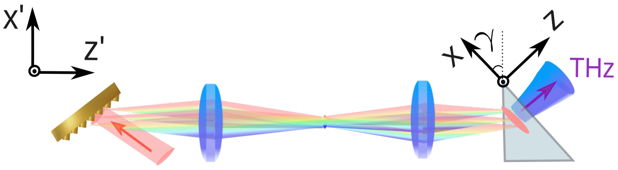

Figure 11: Illustration of the CG scheme.

The ease of this setup, the high pulse energies and the controllability of the terahertz properties have made this scheme a strong candidate for generating high energy terahertz pulses where the millijoule range can be reached[60]. However, the non-collinear geometry of the PM and the translational asymmetry of the interaction, in combination with the cascading effect, result in terahertz beams which possess a non-uniform spatial distribution. The CG scheme utilizes the grating induced angular dispersion to form a pulse front tilt. The angular dispersion has two effects on the OP away from the imaging plane. One is that the pulse duration increases (due to the decrease in the available bandwidth at each spatial point) with respect to the distance from the imaging plane. The other effect is that the TPF angle reduces with respect to the distance from the imaging plane[55]. These two effects are more pronounced for larger angular dispersion (or broadband OP), leading to the minimum interaction length in the CG scheme compared with all the other schemes. The PM condition along the x' dimension is given in Eq. (69), where γ is the pulse-front-tilt angle, c is the speed of light, θ_o is the grating output angle and $\beta = -F_1 k_0 = 2\pi/\left[\omega_0 \cos(\theta_o) d\right]$ is the first order angular dispersion induced by the grating, where F_1 is defined in Section. 4.2.

In Section. 4.2, the influence of the higher order angular dispersion on terahertz generation is presented analytically. In this section, I focus on the influences of the grating and imaging system (see Fig. 5) on the OP. Using the results in Section. 3, one can prove that the corresponding electric field at the LN input surface (the imaging plane) is

$$\begin{aligned} E(\omega, x', z') = \quad & E_0 \sqrt{\frac{f_1 \cos(\theta_i)}{f_2 \cos(\theta_o)}} \exp\left(\frac{-\Delta\omega^2\tau^2}{4}\right) \exp\left(\frac{-x'^2 f_1^2 \cos(\theta_i)^2}{2\sigma'^2 f_2^2 \cos(\theta_o)^2}\right) \\ & \times \exp\left(-i\beta\Delta\omega x' f_1/f_2\right) \exp\left(\frac{-i\omega n_{ir}(\omega) z'}{c}\right) \end{aligned} \tag{67}$$

where the θ_i and θ_o are the incident and output angle of the OP at the grating. The grating has two effects on the OP, one is rescaling the beam size by the factor $\cos(\theta_o)/\cos(\theta_i)$, which also leads to a rescaling of the amplitude. The other is introducing the phase $\exp\left(i\beta\Delta\omega x\right)$[55]. This phase factor represents the angular dispersion to the first order and leads to a spatial dependent delay. Compared with the center of the beam ($x' = 0$), at $x' > 0$ the beam travels faster and at $x' < 0$ the beam experiences a delay. The telescope imaging system also has two effects. One is rescaling the beam size by the factor f_2/f_1 and likewise the amplitude change accordingly. The other is changing the angular dispersion by the factor $-f_1/f_2$. After the telescope system, the $x' > 0$ region of the incident beam locates at the $x' < 0$ region and vice versa. This indicates that after the telescope system, at $x' > 0$ the beam experiences a delay. One can notice that the scaling factors of the beam size and the angular dispersion, induced by the telescope system, are inversely proportional to each other. This can also be understood intuitively, since the angular divergence is inversely proportional to the beam size. The second order nonlinear polarization for the terahertz generation is

$$\begin{aligned} P^{(2)}(\Omega, x', z') = & \frac{E_0^2\chi^{(2)}\sqrt{2\pi}f_1\cos(\theta_i)}{\tau f_2\cos(\theta_o)}\exp\left[\frac{-x'^2 f_1^2\cos(\theta_i)^2}{\sigma'^2 f_2^2\cos(\theta_o)^2}\right]\exp\left(\frac{-\Omega^2\tau^2}{8}\right) \\ & \times\exp\left[iz'\Omega(n_t\cos(\gamma) - n_g)/c\right]\exp\left\{i\Omega x'\left[n_t\sin(\gamma)/c - \beta f_1/f_2\right]\right\} \end{aligned} \tag{68}$$

From Eq. (68), it can be seen that the phase matching conditions are

$$\begin{aligned} \Delta k'_z = \Omega(n_t\cos(\gamma) - n_g)/c = 0 \longrightarrow & \quad n_t\cos(\gamma) = n_g \\ \Delta k'_x = \Omega\left[n_t\sin(\gamma)/c - \beta f_1/f_2\right]/c = 0 \longrightarrow & \quad \tan(\gamma) = \beta c f_1/(f_2 n_g) \end{aligned} \tag{69}$$

Fig. 12(b-c) indicates that, compared to the 0.5 mm OP, the terahertz field generated by 4 mm OP suffers from more translational spread in terms of fluence and temporal distribution. By increasing the OP spot size by 8 times, the terahertz beam size increases ~ 50%. This is the main reason of the efficiency drop for large OP beam size as shown in Fig. 32. Furthermore, Fig. 12(a) indicates that most of the energy is contained in the single-cycle region of the terahertz electric field.

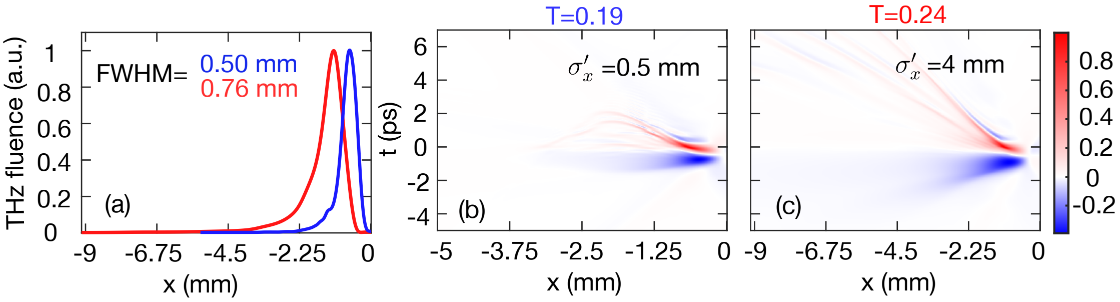

Figure 12: Numerical results of the terahertz electric field generated by CG scheme. (a) represents the output terahertz fluence with 0.5mm OP (blue) and 4 mm OP (red) respectively. The terahertz electric field distribution versus *x* generated by 0.5 mm and 4 mm OP are shown in (b) and (c) respectively. The terahertz energy transmission at the exit surface of the LN is denoted by T.

The terahertz spectra generated by different OP beam sizes are presented in Fig. 13. One can see that, the terahertz pulse generated by a larger OP beam size possesses lower center frequency due to the absorption and longer interaction length. Figure 14 shows the dependence of the OP fluence. Lower OP fluence leads to larger terahertz beam size. However, the terahertz spectrum doesn't vary much with respect to fluence. In this scheme, the angular dispersion is the dominating factor for effective interaction length. By reducing the energy, the effective length doesn't vary much.

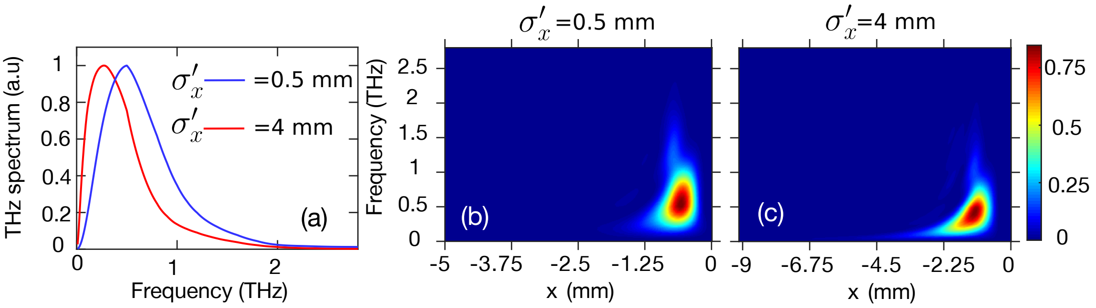

Figure 13: Numerical results of the terahertz spectra generated by CG scheme. (a) represents the terahertz spectra generated by 0.5mm OP (blue) and 4 mm OP (red) respectively. The spatial dependent terahertz spectral densities are shown in (b) and (c) respectively.

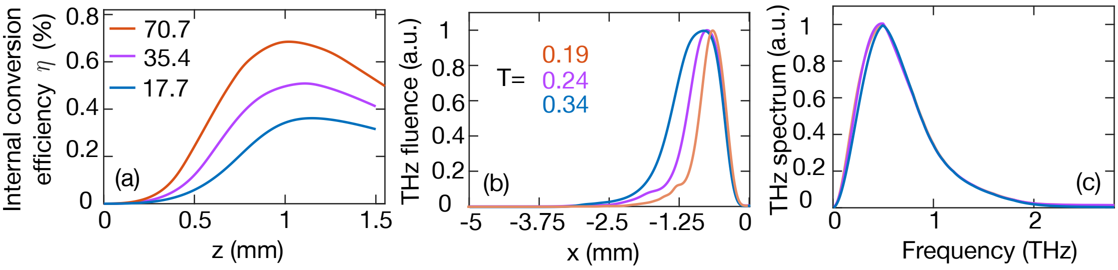

Figure 14: With a given OP beam size (σ'_x =0.5 mm), (a) represents the internal terahertz conversion efficiency with pump fluence 70.7 mJ/cm^2, 35.4 mJ/cm^2 and 17.7 mJ/cm^2 respectively. The terahertz fluences and corresponding spectra at the peak of each efficiency curve are shown in (b) and (c) respectively. The out-coupling energy transmission is denoted by T.

5.3 (b) Nonlinear echelon staircase (NLES)

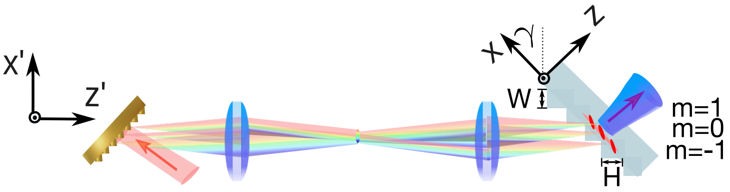

Figure 15: Illustration of the NLES scheme. Each of the steps is identified by m where $m = 0, \pm 1, \pm 2 \cdots$. The center of the pump beam ($x' = 0$) is noted by $m = 0$.

In this configuration, the grating and the telescope system resembles the CG scheme in Section. 5.2. The difference is that the prism shaped LN crystal is replaced by a stair case LN structure. The stair step size in x' and z' dimensions are represented by W and H respectively (see Fig. 15). This method is beneficial for generating high energy, large size and spatially homogeneous terahertz beams. The step size of the LN nonlinear echelon at x' and z' dimensions are represented by W and H respectively.

By setting $\sigma'_m \sim W/2$, $q_0 = i\pi\sigma'^2_m/\lambda_0$ and $q_m = q_0 - mH + mH/n_0$, where n_0 is the refractive index of the OP at center frequency ω_0, the electric field at the LN input surface is given in Eq. (70). The corresponding polarization can be found in Eq. (71).

$$\begin{aligned}
E(\omega,x',z') = \quad & E_0 \sum_{m=-\infty}^{\infty} \sqrt{\frac{q_0 f_1 \cos(\theta_i)}{q_m f_2 \cos(\theta_o)}} \exp\left(\frac{-\Delta\omega^2\tau^2}{4}\right) \\
& \times \exp\left(\frac{-x'^2 f_1^2 \cos(\theta_i)^2}{2\sigma'^2 f_2^2 \cos(\theta_o)^2}\right) \exp\left[\frac{-ik_0(x'-mW)^2}{2q_m}\right] \\
& \times \exp\left(-i\beta\Delta\omega x' f_1/f_2\right) \exp\left(\frac{-i\omega n_{ir}(\omega) z'}{c}\right) \\
& \times \exp\left[-i\omega m H\left(n_{ir}(\omega)-1\right)/c\right]
\end{aligned} \tag{70}$$

$$\begin{aligned}
P(\Omega,x',z') = \quad & \frac{E_0^2 \chi^{(2)} \sqrt{2\pi} f_1 \cos(\theta_i)}{\tau f_2 \cos(\theta_o)} \sum_{m=-\infty}^{\infty} \left|\frac{q_0}{q_m}\right| \exp\left(\frac{-\Omega^2\tau^2}{8}\right) \\
& \times \exp\left(\frac{-x'^2 f_1^2 \cos(\theta_i)^2}{\sigma'^2 f_2^2 \cos(\theta_o)^2}\right) \exp\left[\frac{-k_0^2\sigma_m^2(x'-mW)^2}{\left|q_m\right|^2}\right] \\
& \times \exp\left\{i\Omega\left[n_t \sin(\gamma) x' - c\beta x' f_1/f_2 - mH\left(n_{ir}(\omega)-1\right)\right]/c\right\} \\
& \times \exp\left[i\Omega z'(n_t\cos(\gamma) - n_g)/c\right]
\end{aligned} \tag{71}$$

Equation 71 indicates that the phase matching conditions are

$$\begin{aligned}
\Delta k'_z &= \Omega(n_t\cos(\gamma) - n_g)/c = 0 \longrightarrow n_t\cos(\gamma) = n_g \\
\Delta k'_x x' &= \Omega\left[n_t \sin(\gamma) x' - c\beta x' \frac{f_1}{f_2} - mH\left(n_g - 1\right)\right]/c = 0 \\
&\longrightarrow \left[n_g \tan(\gamma) - \frac{c\beta f_1}{f_2}\right] x' = mH(n_g-1)
\end{aligned} \tag{72}$$

It can be seen that Eq. (72) is not always satisfied along x' since m can only be integers. Although the entire trend of the beamlets follow the PM angle, each beamlet itself is not perfectly phase matched. In order to maintain the trend of the pulse-front-tilt, the size of the LN stair should be chosen such that the terahertz pulse propagates perpendicular to the entrance and exit surfaces of the plane-parallel LN slab i.e. the condition H/W = $\tan(\gamma)$ needs to be satisfied[68]. Another condition is that, when $m = 1$, x' = W (at $m = 0$, the beamlet is centered at position x' = W). With these two conditions, Eq. (72) reduces to $c\beta f_1/f_2 = \tan(\gamma)$. Compared with the CG scheme in Eq. (69), the NLES scheme requires less angular dispersion. Additionally, with different input pump fluence, the effective length varies due to the nonlinear effects and thus the thickness of the NLES slab should vary accordingly. With different input OP pulse duration, the optimal effective length may differ. However, for a given NLES with fixed thickness, this can be adjusted by adapting the pump fluence.

Figure 16 indicates that by changing the OP beam size the generated terahertz beam size changes accordingly. Besides, as long as $\sigma'_x > \sin(\gamma)L_{\text{eff}}$ is satisfied, the generation efficiency is independent of the OP beam size. These enable the possibility of generating high energy terahertz pulses by simply increasing the pump energy and the OP beam size. Additionally, the electric fields show strong single-cycle character homogeneously along the entire translational dimension (x).

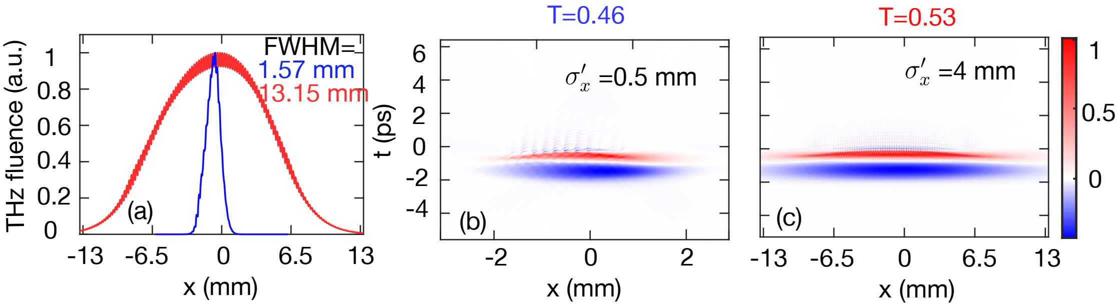

Figure 16: Numerical results of the terahertz electric field generated by NLES scheme. (a) represents the output terahertz fluence with 0.5mm OP (blue) and 4 mm OP (red) respectively. The electric field distribution versus x of terahertz pulses generated by 0.5 mm OP and 4 mm OP are shown in (b) and (c) respectively. The terahertz energy transmission at the exit surface of the LN is denoted by T.

Figure 17 show the terahertz spectra generated by different OP beam size. In this scheme, the terahertz spectrum shape is not related to the OP beam size. Figure 18 shows the dependence of the OP fluence. Lower OP fluence leads to larger terahertz beam size. However, the terahertz spectrum does not vary much with respect to fluence.

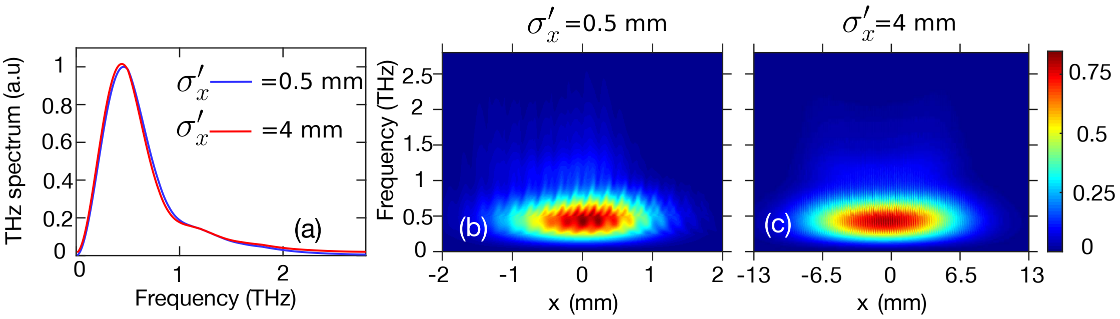

Figure 17: Numerical results of the terahertz spectra generated by CG scheme. (a) represents the terahertz spectra generated by 0.5mm OP (blue) and 4 mm OP (red) respectively. The spatial dependent terahertz spectral densities are shown in (b) and (c) respectively.

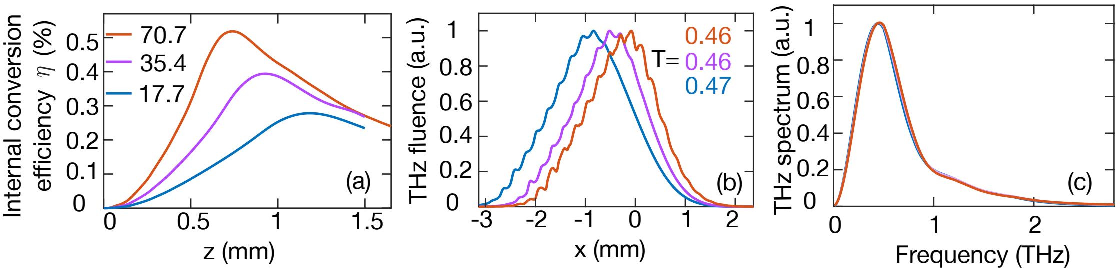

Figure 18: With a given OP beam size (σ'_x =0.5 mm), (a) represents the internal terahertz conversion efficiency with pump fluence 70.7 mJ/cm^2, 35.4 mJ/cm^2 and 17.7 mJ/cm^2 respectively. The terahertz fluences and corresponding spectra at the peak of each efficiency curve are shown in (b) and (c) respectively. The out-coupling energy transmission is denoted by T.

5.4 (c) Reflective echelon (RES)

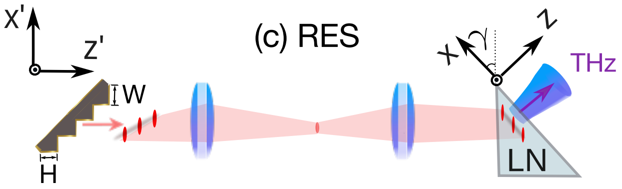

Figure 19: Illustration of the RES scheme.

Echelon is a grating structure with large groove density (input beam wavelength $\ll$ step size). For the echelon, the input beam and the output beam propagates exactly in the opposite direction, since each step acts as a mirror. As the step size reduces (input beam wavelength $\simeq$ step size), the diffraction effect of each step increases. Thus, the electric fields generated at each step form an interference pattern. Depending on the wavelength of the input beam and the size of the steps, the final interference pattern can have different dominant reflection angles. This corresponds to the order of the grating. As the step size reduces even further (input beam wavelength $\ll$ step size), the discrete steps reduce to a smooth surface. At this point, the reflection occurs, i.e. the diffraction effect of each step is so strong that the entire diffraction pattern merges together and forms one dominant order which is equivalent to the reflection from a flat mirror surface.

Compared with the CG scheme, in this scheme the effective interaction length is not limited by angular dispersion. The echelon step sizes in z' and x' dimensions are represented by H, W respectively (see Fig. 19). The temporal delay between the two neighboring beamlets is $2\mathrm{H}/c$. Before the imaging system, $m = 1$ represents the beamlet at center position x' =W. After the imaging system, the delay remains $2\mathrm{H}/c$, whereas for $m = 1$ the beamlet is centered at position $x' = -\mathrm{W}f_2/f_1$. Consequently, together with Eq. (76), it can be seen that the echelon structure needs to satisfy the condition $\tan(\gamma) = 2\mathrm{H}f_1/\mathrm{W}n_g f_2$ to generate terahertz effectively. Similar to the NLES scheme, the PM condition given in Eq. (76) is not always satisfied along x'.

By setting $\sigma'_m \sim W/2$, one can write $q_0 = i\pi\sigma'^2_m/\lambda_0$ and $q_m = q_0 - 2mH$. Consequently, the input OP electric field after the echelon structure before the imaging system, the electric field at the LN input surface and the second order polarization for terahertz generation are shown in Eqs (73), (74) and (75) respectively.

$$\begin{aligned} E(\omega, x', z') = \quad & E_0 \sum_{m=-\infty}^{\infty} \sqrt{\frac{q_0}{q_m}} \exp\left(\frac{-x'^2}{2\sigma'^2_x}\right) \exp\left[\frac{-i(x' - mW)^2 k_0}{2q_m}\right] \\ & \times \exp\left(-\frac{\Delta\omega^2\tau^2}{4}\right) \exp\left(i\Delta\omega 2mH/c\right) \end{aligned} \tag{73}$$

$$
\begin{aligned}
E(\omega, x', z') = \quad & E_0 \sum_{m=-\infty}^{\infty} \sqrt{\frac{f_1 q_0}{f_2 q_m}} \exp\left(\frac{-x'^2 f_1^2}{2\sigma'^2_x f_2^2}\right) \exp\left[\frac{-ik_0(x' + mWf_2/f_1)^2 f_1^2}{2q_m f_2^2}\right] \\
& \times \exp\left(-\frac{\Delta\omega^2\tau^2}{4}\right) \exp\left(i2\Delta\omega mH/c\right) \exp\left[\frac{-i\omega n_{ir}(\omega)z'}{c}\right] \qquad (74)
\end{aligned}
$$

$$
\begin{aligned}
P^{(2)}(\Omega, x', z') = \quad & \frac{E_0^2 \chi^{(2)} \sqrt{2\pi} f_1}{\tau f_2} \sum_{m=-\infty}^{\infty} \left|\frac{q_0}{q_m}\right| \exp\left[\frac{-x'^2 f_1^2}{\sigma'^2 f_2^2}\right] \\
& \times \exp\left[\frac{-k_0^2 \sigma'^2_m (x' + mWf_2/f_1)^2 f_1^2}{\left|q_m\right|^2 f_2^2}\right] \exp\left(\frac{-\Omega^2\tau^2}{8}\right) \\
& \times \exp\left[iz'\Omega(n_t\cos(\gamma) - n_g)/c\right] \exp\left\{i\Omega\left[n_t \sin(\gamma)x' + 2mH\right]/c\right\} \quad (75)
\end{aligned}
$$

It is important to notice that compared with Eq. 74, the term $x' - mW$ on the second exponential changes to $x' + mW$ in Eq. 75. This is due to the telescope imaging system which flips the positive and the negative parts of the OP in the x' dimension. In Eq. 75, $m > 0$, represents the beamlets which locate at the center positions $x' < 0$. From Eq. (75), it can be seen that the phase matching conditions are listed as the following. Since at $m = -1$, $x' = Wf_2/f_1$, one can see from the phase matching condition in the x' dimension that $\tan(\gamma) = 2Hf_1/Wn_g f_2$.

$$
\begin{aligned}
\Delta k'_z = \Omega(n_t\cos(\gamma) - n_g)/c = 0 \longrightarrow \quad & n_t\cos(\gamma) = n_g \\
\Delta k'_x x' = \Omega\left[n_t\sin(\gamma)x' + 2mH\right]/c = 0 \longrightarrow \quad & \tan(\gamma)x' = -2mH/n_g \qquad (76)
\end{aligned}
$$

Examples of the beamlets spatial profiles are shown in Fig. 20. Figures 20(b-c) indicate that the nonlinear interactions largely modify the spatial profiles of each beamlet. It can be seen from Fig. 21 that the electric field distributions are very similar to the CG scheme. However, the terahertz beam size is far larger ($\sim \times 2$) than the ones produced by the CG. For small OP beam size ($\sigma'_x = 0.5$ mm), the output terahertz beamsize reduces with respect to the increase of the initial angular dispersion, i.e. STC > RES > CG. Due to the large angular dispersion, the OP intensity decreases more significantly along the propagation direction z'. This drastic intensity decrease delivers terahertz pulse with less energy close to the base of the LN.

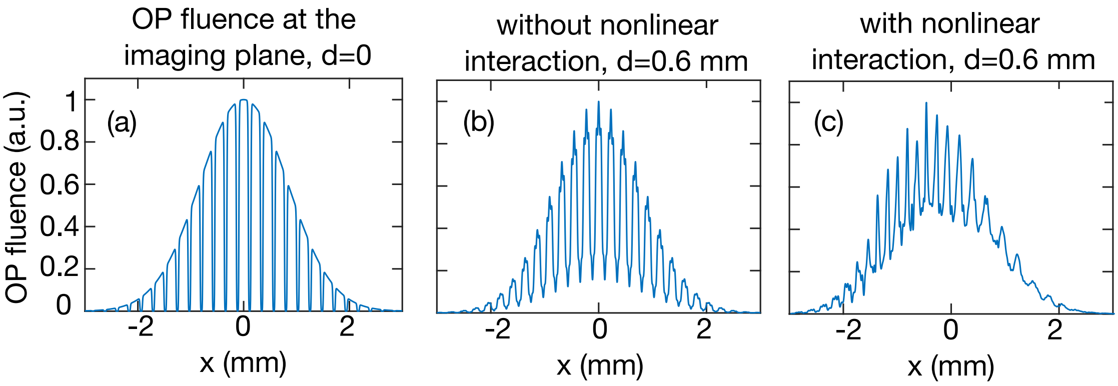

Figure 20: The beamlets spatial profile at the imaging plane is shown in (a). The beamlets spatial profiles without and with nonlinear interactions are presented in (b) and (c), respectively. The interaction distance with respect to the imaging plane in the terahertz coordinates (x-z) is denoted by d.

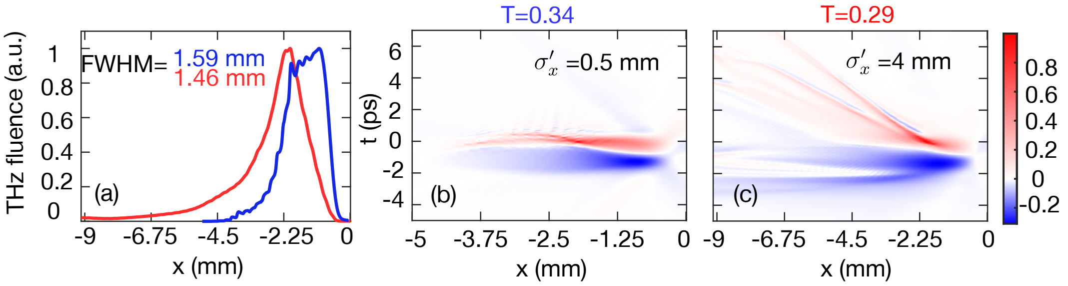

Figure 21: Numerical results of the terahertz electric field generated by RES scheme. (a) represents the output terahertz fluence with 0.5mm OP (blue) and 4 mm OP (red) respectively. The electric field distribution versus x of terahertz pulses generated by 0.5 mm OP and 4 mm OP are shown in (b) and (c) respectively. The terahertz energy transmission at the exit surface of the LN is denoted by T.

The terahertz spectra generated by different OP beam sizes are presented in Fig. 22. One can see that, the terahertz pulse generated by larger OP beam size possesses lower center frequency due to the absorption and longer interaction length. Figure 23 shows the dependence of the OP fluence. Lower OP fluence leads to larger terahertz beam size. The terahertz spectrum does not vary much with respect to the OP fluence.

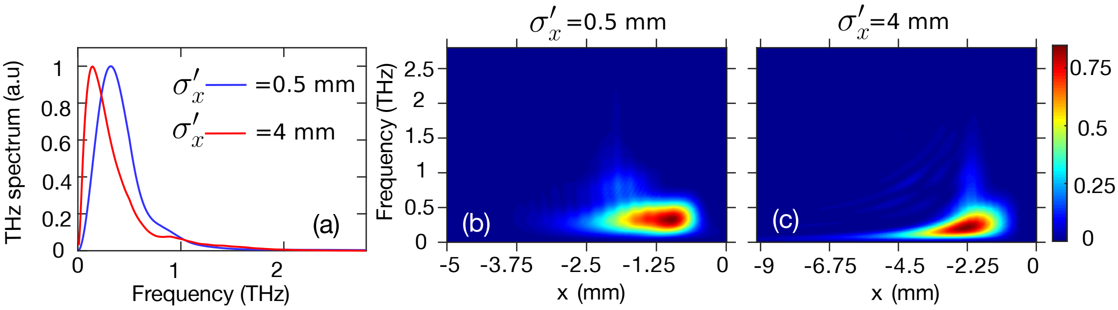

Figure 22: Numerical results of the terahertz spectra generated by CG scheme. (a) represents the terahertz spectra generated by 0.5mm OP (blue) and 4 mm OP (red) respectively. The spatial dependent terahertz spectral density are shown in (b) and (c) respectively.

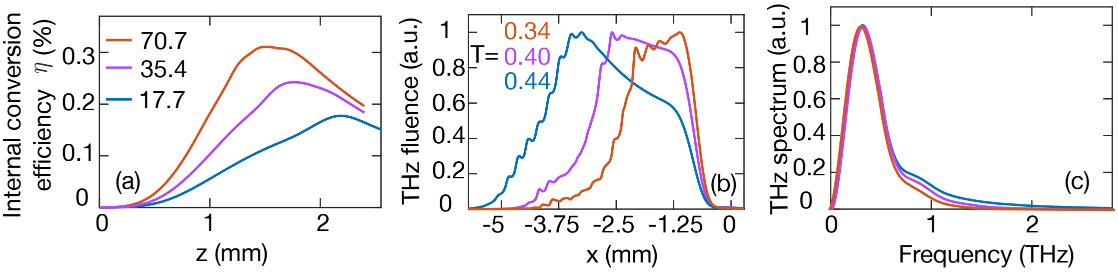

Figure 23: With a given OP beam size (σ'_x =0.5 mm), (a) represents the internal terahertz conversion efficiency with pump fluence 70.7 mJ/cm^2, 35.4 mJ/cm^2 and 17.7 mJ/cm^2 respectively. The terahertz fluences and corresponding spectra at the peak of each efficiency curve are shown in (b) and (c) respectively. The out-coupling energy transmission is denoted by T.

5.5 (d) Spatial-temporal chirp (STC)

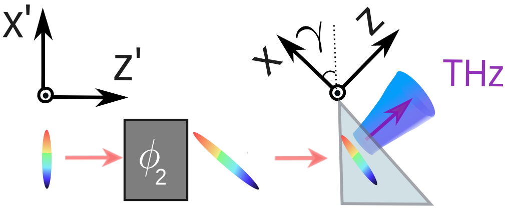

Figure 24: Illustration of the STC scheme.

In this scheme, no initial angular dispersion is present, leading to a maximum conversion efficiency among all 5 schemes discussed. However, the input OP pulse has to be broadband and a ELI-ALPS SYLOS laser can be an ideal option.

The full width half maximum (FWHM) of the overall input OP spectral bandwidth is presented in Eq. (77), which corresponds to a ~10 fs transform limited pulse. For a fair comparison, the local transform limited pulse duration (τ_0) at a given x' position is chosen to be 350 fs. Thus, the local pulse duration remains 500 fs after the chirp.

$$f_{\text{FWHM}} = \sigma_x' \sqrt{2\log(2)(v^2\tau^2/2 + 1/\sigma_x'^2)}/\tau\pi \tag{77}$$

In Eq. (77), v is the spatial chirp rate and $\tau = \tau_0/\sqrt{2\log 2}$. The PM condition is presented in Eq. (80) where ϕ_2 is the second order dispersion. The OP electric field at the LN input surface and the second order polarization for terahertz generation are shown in Eqs. (78) and (79) respectively.

$$E(\omega, x', z') = E_0 \exp\left(\frac{-x'^2}{2\sigma_x'^2}\right) \exp\left[-\frac{(\Delta\omega - vx')^2\tau^2}{4}\right] \exp\left(-\frac{i\phi_2\Delta\omega^2}{2} - ik(\omega)z'\right) \tag{78}$$

$$\begin{aligned} P(\Omega, x', z') = \quad & \frac{\chi^{(2)}\sqrt{2\pi}E_0^2}{\tau} \exp\left(-\frac{x'^2}{\sigma_x'^2}\right) \exp\left[-\frac{\Omega^2\tau^2}{8}\left(1 + \frac{4\phi_2^2}{\tau^4}\right)\right] \\ & \times \exp\left\{-i\Omega x'\left[v\phi_2 - \frac{n_t \sin(\gamma)}{c}\right]\right\} \exp\left\{\frac{-i\Omega z'}{c}\left[n_g - n_t\cos(\gamma)\right]\right\}. \end{aligned} \tag{79}$$

$$\begin{aligned} \Delta k_z' &= \Omega\left[n_t\cos(\gamma) - n_g\right]/c = 0 \longrightarrow & n_t\cos(\gamma) &= n_g \\ \Delta k_x' &= \Omega\left[v\phi_2 - n_t\sin(\gamma)\right]/c \longrightarrow & v\phi_2 &= \tan(\gamma) n_g/c \end{aligned} \tag{80}$$

One can also choose smaller input OP bandwidth together with a larger ϕ_2. However, this leads to the temporal broadening of the OP at each spatial point, which is not in favor of the terahertz generation process. In the following simulations, $\phi_2 = 0.045$ ps^2 is chosen.

From Fig. 25, it can be seen that the electric field shows nearly perfect few-cycle property. With the given OP beamsize (σ_x' =0.5 mm), this scheme delivers the largest terahertz beam size. However, the disadvantage is that the input OP must contain a large bandwidth. Additionally, since the bandwidth of the OP is also related to the input beam size (see Eq. (77)), this scheme is not applicable to large OP beamsize.

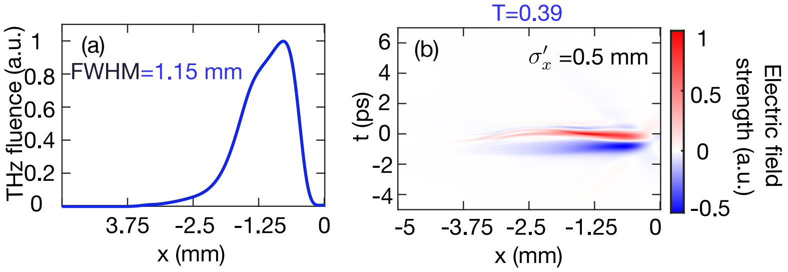

Figure 25: Numerical results of the terahertz electric field generated by STC scheme. (a) represents the output terahertz fluence with 0.5mm OP. The electric field distribution versus x of terahertz pulses generated by 0.5 mm OP is shown in (b). The terahertz energy transmission at the exit surface of the LN is denoted by T.

The terahertz spectra generated by different OP beam sizes are presented in Fig. 26. Figure 27 shows the dependence of the OP fluence. Lower OP fluence leads to larger terahertz beam size. The terahertz spectrum does not vary much with respect to the OP fluence.

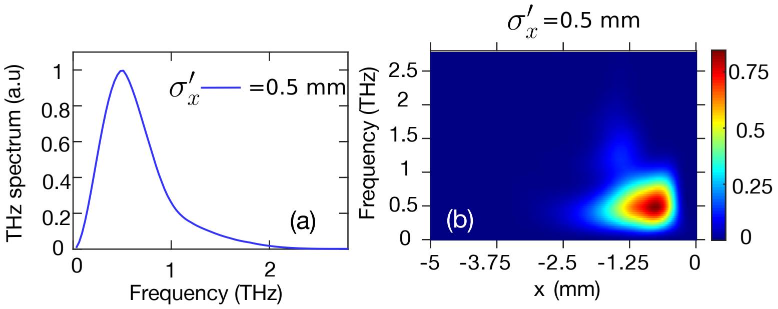

Figure 26: Numerical results of the terahertz spectra generated by CG scheme. (a) represents the terahertz spectra generated by 0.5 mm OP. The spatial dependent terahertz spectral density is shown in (b).

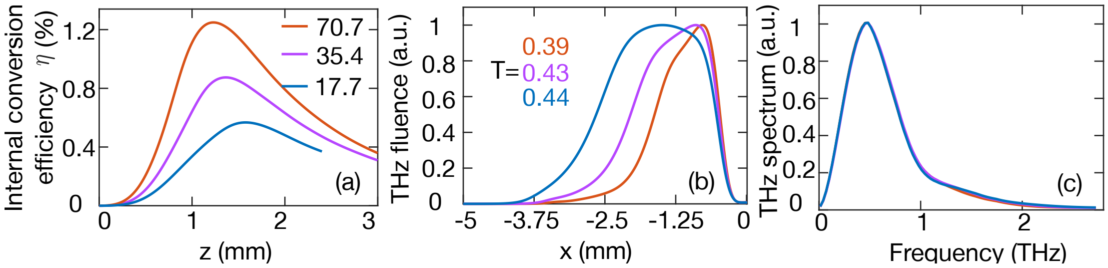

Figure 27: With a given OP beam size (σ'_x =0.5 mm), (a) represents the internal terahertz conversion efficiency with pump fluence 70.7 mJ/cm^2, 35.4 mJ/cm^2 and 17.7 mJ/cm^2 respectively. The terahertz fluences and corresponding spectra at the peak of each efficiency curve are shown in (b) and (c) respectively. The out-coupling energy transmission is denoted by T.

5.6 (e) Multi step phase mask (MSPM)

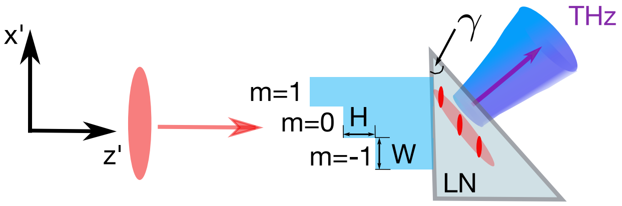

Figure 28: Illustration of the MSPM scheme. Each of the steps is identified by m where $m = 0, \pm 1, \pm 2 \cdots$. The center of the pump beam ($x' = 0$) is noted by $m = 0$.

In this scheme, no imaging system is required. The delay of each beamlet is generated by different propagation lengths inside the mask stripes. In the simulation, silica with refractive index n is chosen as the mask material due to low dispersion at the OP wavelength. The phase mask step size in x' and z' dimensions are W and H respectively (see Fig. 28). This is very similar to scheme (c) RES. However, the imaging system in scheme (c) guarantees that at the image plane, each beamlet experiences the same condition whereas in scheme (e), this does not happen. In scheme (e), the diffraction modifies the beamlets envelope drastically, leading to poor terahertz electric field quality. It can be seen in the comparison of schemes (c) and (e) that an imaging system is necessary. Numerically, each beamlet maintains the shape of the input OP envelope. However, in the following calculation, the analytical result is shown with the assumption that each beamlet is of a Gaussian shape with the size comparable to the MSPM step size. The input electric field at the LN surface is defined as the following

$$\begin{aligned} E(\omega,x',z') = \quad & E_0 \sum_{m=-\infty}^{\infty} \sqrt{\frac{q_0}{q_m}} \exp\left(\frac{-x'^2}{2\sigma_x'^2}\right) \exp\left[\frac{-i(x'-mW)^2 k_0}{2q_m}\right] \exp\left(\frac{-i\omega n_{ir}(\omega) z'}{c}\right) \\ & \times \exp\left(-\frac{\Delta\omega^2\tau^2}{4}\right) \exp\left\{-i\Delta\omega\left[mH(n-1)+L_0+L_1 n\right]/c\right\} \end{aligned} \tag{81}$$

where $\sigma'_m \sim W/2$, γ is the phase matching angle inside the LN, $q_0 = i\pi\sigma_m'^2/\lambda_0$ and $q_m = q_0 + L_0 + L_1/n - mh(1-1/n)$. The q_m obtained from Eq. (47), where the new complex parameter as a function of the propagation distance in a medium is presented. The term $L_0 + L_1 n$ is the optical path from the center of the OP ($x' = 0$) to the LN surface with the propagation distances in the air and in the MSPM noted by L_0 and L_1 respectively. The refractive index of the MSPM is represented by n, which should be chosen such that the dispersion doesn't play a significant role. Thus, n is not frequency dependent. From the q_m, one can get the corresponding beam waist as

$$w_m^2 = \frac{|q_m|^2}{k_0^2\sigma_m'^2} = \frac{\left[L_0 + L_1/n - mh(1-1/n)\right]^2 + \left(\pi\sigma_m'^2/\lambda_0\right)^2}{k_0\pi\sigma_m'^2/\lambda_0}$$

Consequently, the polarization of the terahertz generation can be written as Eq. (82). The exponential term $\exp\left[-i\Omega\left(L_0 + L_1 n\right)/c\right]$ represents a constant time delay and thus, can be set to zero without losing generality. From Eq. (82), one can obtain the PM in Eq.

(83).

$$P(\Omega, x', z') = \frac{E_0^2\chi^{(2)}\sqrt{2\pi}}{\tau}\sum_{m=-\infty}^{\infty}\left|\frac{q_0}{q_m}\right|\exp\left(\frac{-x'^2}{\sigma_x'^2}\right)\exp\left[\frac{-(x'-mW)^2}{w_m^2}\right]\exp\left[-i\Omega\left(L_0+L_1n\right)/c\right]$$
$$\times\exp\left(\frac{-\Omega^2\tau^2}{8}\right)\exp\Big[i\Omega z'(n_t\cos(\gamma)-n_g)/c\Big]\exp\Big\{i\Omega\Big[n_t\sin(\gamma)x'-mH(n-1)\Big]/c\Big\} \quad (82)$$

$$\begin{aligned}\Delta k_z' = \Omega(n_t\cos(\gamma)-n_g)/c = 0 \longrightarrow &\quad n_t\cos(\gamma) = n_g\\ \Delta k_x'x' = \Omega\Big[n_t\sin(\gamma)x'-mH(n-1)\Big]/c = 0 \longrightarrow &\quad n_g\tan(\gamma)x' = mH(n-1) \quad (83)\end{aligned}$$

When $m = 1$, i.e $x' = W$, Eq. (83) reduces to $n_g\tan(\gamma)/(n-1) = H/W$. It is very important to notice that since m can only be integers, Eq. (83) is not always satisfied along x'. This indicates that the entire trend of the beamlets satisfies the phase matching condition while each individual beamlet is not phase matched.

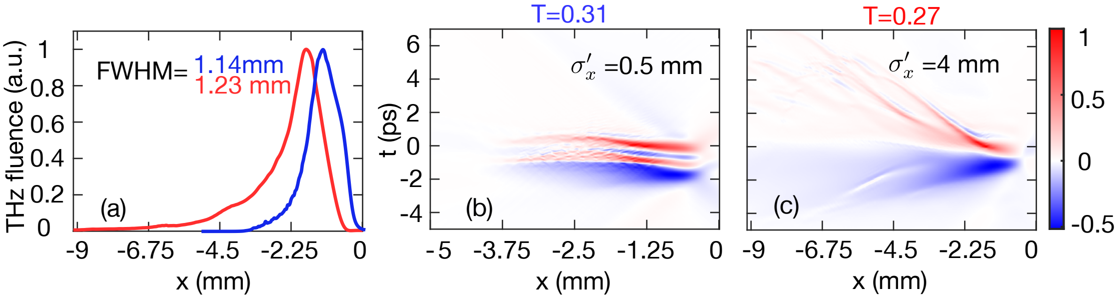

Figure 29: Numerical results of the terahertz electric field generated by MSPM scheme. (a) represent the output terahertz fluence with 0.5mm OP (blue) and 4 mm OP (red) respectively. The electric field distribution versus x of terahertz pulses generated by 0.5 mm OP and 4 mm OP are shown in (b) and (c) respectively. The terahertz energy transmission at the exit surface of the LN is denoted by T.

The terahertz spectra generated by different OP beam sizes are presented in Fig. 30. The terahertz spectrum generated by a larger OP beam size possesses a Gaussian distribution whereas the terahertz spectrum generated by a small OP beam size shows an interference pattern. This indicates that the phase-matching condition is not perfectly fulfilled. Figure 31 shows the dependence of the OP fluence. Lower OP fluence leads to larger terahertz beam size. The terahertz spectra do not vary much with respect to the OP fluence.

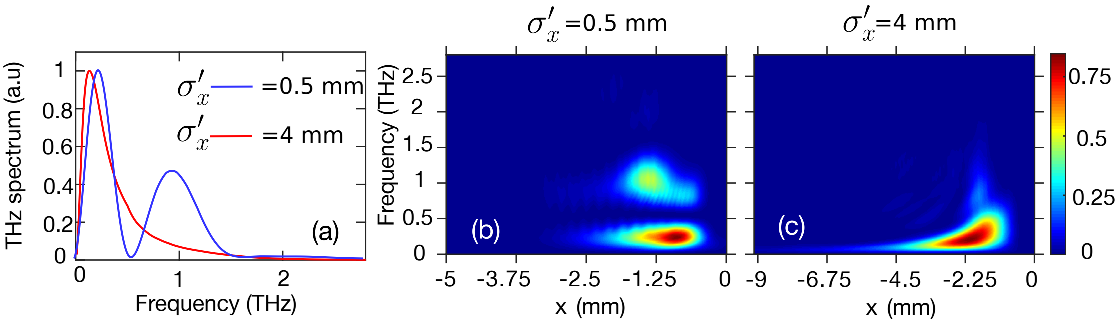

Figure 30: Numerical results of the terahertz spectra generated by CG scheme. (a) represents the terahertz spectra generated by 0.5mm OP (blue) and 4 mm OP (red) respectively. The spatial dependent terahertz spectral density are shown in (b) and (c) respectively.

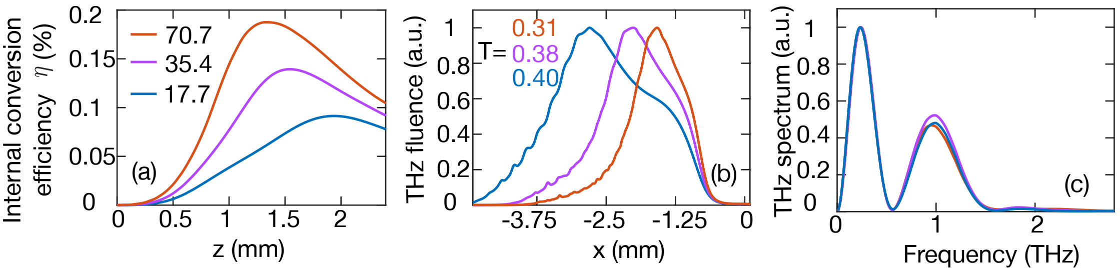

Figure 31: With a given OP beam size (σ'_x =0.5 mm), (a) represents the internal terahertz conversion efficiency with pump fluence 70.7 mJ/cm^2, 35.4 mJ/cm^2 and 17.7 mJ/cm^2 respectively. The terahertz fluences and corresponding spectra at the peak of each efficiency curve are shown in (b) and (c) respectively. The out-coupling energy transmission is denoted by T.

5.7 Comparison of different schemes

In schemes (a-c), the imaging systems are chosen such that the image of the grating (echelon) overlaps with the pulse-front-tilt inside the LN[61]. This is considered to be the optimal imaging condition and the analytical expressions can be found in Eqs. (84-86).

The lens at the farther side of the LN has a fixed focusing length $f_1 = 300$ mm and the one close to the LN has a focusing length f_2. The optimal imaging conditions for different schemes are the following,

conventional grating (CG), scheme (a): (84)

$$\sin(\theta_o) = \frac{1}{2}\left[\frac{-n\lambda_0}{\tan^2(\gamma)n_g d} + \sqrt{\left(\frac{n\lambda_0}{\tan^2(\gamma)n_g d}\right)^2 + 4}\,\right],$$

$$\frac{f_2}{f_1} = \frac{\lambda_0}{d\cos(\theta_o)\tan(\gamma)n_g} = 0.613$$

nonlinear echelon (NLES), scheme (b): (85)

$$\sin(\theta_o) = \frac{1}{2}\left[\frac{-n\lambda_0}{\tan^2(\gamma)(n-1)d} + \sqrt{\left(\frac{n\lambda_0}{\tan^2(\gamma)(n-1)d}\right)^2 + 4}\,\right],$$

$$\frac{f_2}{f_1} = \frac{\lambda_0}{d\cos(\theta_o)\tan(\gamma)} = 1.057$$

reflective echelon (RES), scheme (c): (86)

$$\sin(\theta_o) = \sqrt{\frac{1}{1 + 2n/\tan^2(\gamma)n_g}},\quad \frac{f_2}{f_1} = \sqrt{\frac{2}{n\,n_g}} = 0.646$$

where the θ_o is the output grating angle of OP and n_g is the group velocity refractive index of the OP at ω_0 in the lithium niobate (LN).

For a fair comparison, the peak fluence of the OP at the LN input surface is set the same for all the schemes. In particular, σ'_x which is the OP beam size at the LN input surface i.e after optical elements and the imaging system, is also kept the same. For schemes (b), (c) and (e), the size of the beamlets along x' dimension is kept the same at the LN input surface. The step numbers of the structures are labeled by m. The LN apex is located at $x = 0$. The $z = 0$ coordinate is defined is defined at the location where the center of the OP starts to interact with the LN crystal. With the simulation parameters listed in Table 3, the efficiencies of each scheme are presented in Fig. 32.

Table 3: Simulation parameters

parameter name	value
wavelength λ_0	1018 nm
beam size σ'_x	0.5 mm & 4 mm
grating density d	1/1500 mm
focusing length f_1	300 mm
phase matching angle γ	64.8°
phase matching frequency Ω_0	$2\pi\times$ 0.3 THz
pulse duration (FWHM) τ_0	500 fs[66]
temperature	300 K
peak fluence	$\sqrt{10 \times \tau_0(\mathrm{fs})}$ mJ/cm^2[65]
THz absorption $\alpha(300\,\mathrm{K}, 0.3\,\mathrm{THz})$	7/cm[51]
NLES scheme W, H	97 μm , 206 μm
RES scheme W, H	150 μm[72], 229 μm
MSPM scheme W, H	97 μm , 1000 μm

It can be seen from Fig. 32 that due to the large angular dispersion, CG loses the advantage for longer interaction lengths. For the NLES scheme with high input OP fluence, the optimal effective length is $L_{\mathrm{eff}} = 1/\alpha$. When $\sigma'_x > \sin(\gamma)L_{\mathrm{eff}}$, the efficiency and the optimal interaction length is nearly independent of the OP beamsize. This is due to the fact that since the NLES structure creates beamlets at the LN input surface, all of the beamlets experience an almost identical condition i.e similar walk-off distances. Thus, the generated terahertz spectrum is also not related to the OP beam size, which is a unique property of the NLES compared to all the other schemes. The RES scheme shows less sensitivity with respect to the OP beam size (or interaction length) compared with the CG scheme. The STC scheme delivers highest conversion efficiency and has longest interaction length since it doesn't contain any initial angular dispersion. However, the STC scheme is only applicable for the small OP beam size due to the limitation of the OP bandwidth (see scheme (d) section for more detail). The MSPM and the RES are similar i.e. the PM is achieved by generating time-delayed beamlets. However, despite the similar beam size and interaction length, RES outperforms MSPM in terms of efficiency due to the imaging system and no dispersion from the mask material. As a result, MSPM can be used for larger OP beam sizes. With the small OP beam size, MSPM scheme experiences relatively short interaction length and the diffraction modifies the spatial profiles of the beamlets, leading to poor quality terahertz pulses with largely spread spectrum.

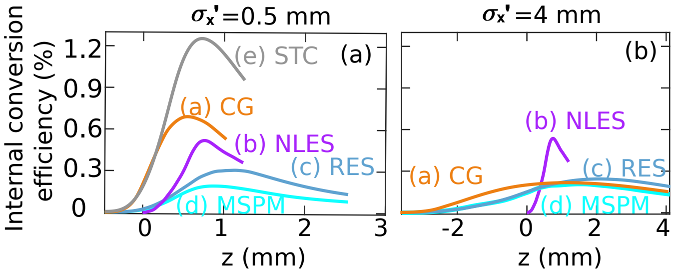

Figure 32: The internal conversion efficiency (without out-coupling loss) of different tilted-pulse-front schemes are plotted against the interaction length. (a) and (b) correspond to 0.5 mm and 4 mm OP beam sizes respectively.

Due to the large terahertz refractive index inside LN ($n(\Omega_0) = 5.2$), the energy loss of the terahertz pulse propagating from the LN into the air is inevitable. The maximum Fresnel transmission (T) at the desired terahertz frequency is $\mathrm{T}=1-(n(\Omega_0)-1)^2/(n(\Omega_0)+1)^2 = 0.54$. To further investigate the out-coupling loss, the energy transmission of the terahertz pulse at the LN output surface is studied. The T is very sensitive to the spatial distribution of the terahertz beam, which is largely dependent on the fluence and size of the OP. Consequently, the T of electric fields at the peak of each efficiency curves in Fig. 32 are calculated and the corresponding results are listed in Table. 4

Table 4: Terahertz energy transmission (T) and the external conversion efficiency (η_e) at the LN output surface

	σ'_x =0.5 mm		σ'_x =4 mm	
	T	η_e (%)	T	η_e (%)
(a) CG	0.19	0.12	0.24	0.05
(b) NLES	0.46	0.24	0.53	0.29
(c)RES	0.34	0.11	0.29	0.07
(d) STC	0.39	0.48	-	-
(e) MSPM	0.31	0.06	0.27	0.06

Due to the non-collinear phase-matching, frequency downshifted optical components generated via the second-order effect, possess large angular spread. This leads to a spatial and temporal break-up of the optical pump, limiting the terahertz generation efficiency and reducing the few-cycle character of the generated terahertz fields. Additionally, large angular diffraction of the terahertz reduces the out-coupling efficiency of the terahertz fields which reduces the overall efficiency further. The simulations suggest that with lower OP input intensity, the terahertz electric field is closer to the single-cycle format along the x dimension and the terahertz beam size increases.

The CG and STC schemes form continuous TPF, where the PM condition is fulfilled along the entire transverse dimension. For the schemes related to beamlets (NLES, RES and MSPM), the entire beamlet-train forms the TPF with the required tilt angle. However, each individual beamlet itself has an offset with respect to the perfect TPF surface. Given a short interaction length, the discrete TPF schemes can not outperform the continuous TPF schemes in terms of efficiency. The MSPM scheme delivers the lowest efficiency and for large OP beam size, the efficiency is comparable to the RES scheme. We do not recommend MSPM scheme for small OP beam size. Among all 3 discrete TPF schemes, the NLES has the best performance in terms of efficiency and terahertz beam quality.

Schemes CG, NLES and RES, are applicable for a large range of parameters such as OP energy, bandwidth and beam size. Within these three schemes, the CG favors smaller interaction length (small beam size) and narrower OP bandwidth due to the large angular dispersion. NLES has a potential of delivering large and homogeneous terahertz beam because of the plane-parallel shape of the LN crystal and the smaller imaging errors in comparison to the CG scheme. Additionally, the generated terahertz spectrum does not depend on the OP beam size. The NLES and RES schemes require manufacturing μm sized structures, which is time consuming and prone to manufacturing errors.

Due to zero initial angular dispersion, the STC scheme delivers the highest conversion efficiency and spatially homogeneous few-cycle terahertz field. However, the OP pulse has to be broadband. Due to the spatial chirp, the bandwidth scales linearly with the OP beam size, making this scheme not applicable to large OP beam sizes.

Table 5: Comparisons of different schemes. The symbols ✓✓, ✓and ✗represent recommend, neutral and not recommend respectively.

	(a) CG	(b) NLES	(c) RES	(d) STC	(e) MSPM
THz quality	✗	✓✓	✓	✓✓	✗
σ'_x scalability	✓	✓✓	✓	✗	✓
parameter flexibility	✓✓	✓	✓✓	✓	✗
efficiency	✓✓	✓✓	✓	✓✓	✗

6 Comparison of LN and KTP using the conventional grating scheme

Potassium titanyl phosphate (KTP) is an inorganic compound with the formula $KTiOPO_4$. It can also be a candidate for terahertz generation. The advantage of this material is the high damage threshold ($\sim \times 3$ of LN)[79]. KTP has larger dispersion at the optical region compared to LN. This leads to less spectral broadening i.e less effective terahertz generation. The KTP absorption at terahertz frequencies and the refractive index at the terahertz and optical frequencies are shown in Fig. 33.

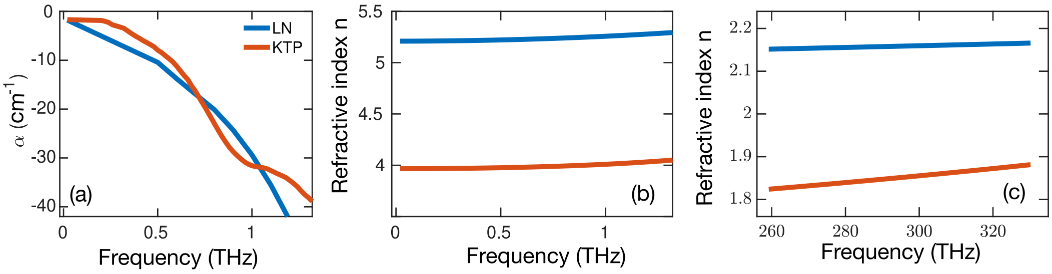

Figure 33: (a) and (b) represent the comparison of terahertz absorption and refractive index of LN and KTP respectively. The data of KTP is obtained from the work of JG. Huang et al.[80]. The refractive index at the optical frequency (~ 1 μm) is presented in (c)[81].

The simulation parameters are kept the same as for the LN. Different parameters are listed in Table 6. Please pay attention that due to the difference of the phase-matching angle, the magnification of the imaging system is not the same as LN.

Table 6: Simulation parameters

parameter name	value
f_2/f_1	0.71
phase matching angle γ	58.2°
$\chi^{(2)}$	109.6 pm/V[82]
n_2	2.3e-19 m^2/W[83]
THz absorption α (300 K, 0.3 THz)	3.2/cm[80]
band gap	3.52 eV[84]

The comparisons between KTP and LN are presented in Fig. 34. In Fig. 34(a), the terahertz spectral range extended over 1.5 THz is not reliable, since the refractive index and absorption is only valid up to 1.5 THz (see Fig. 33). Numerically the material properties over 1.5 THz are computed by linear interpolation of the data within 1.5 THz.

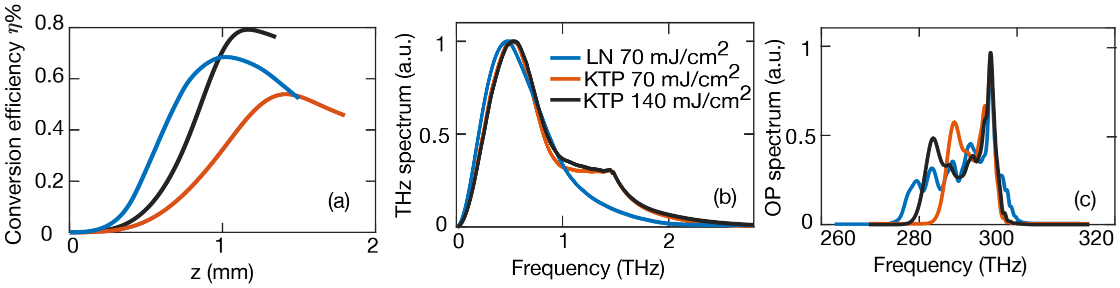

Figure 34: The comparison of the internal conversion efficiencies are presented in (a). (b) and (c) represent the terahertz spectrum and the OP output spectrum at the peak of each efficiency curve.

The comparisons of the electric fields are shown in Fig. 35. It can be seen that due to less angular dispersion, the terahertz electric fields generated by the KTP possess more homogeneous character along the x dimension. Besides, larger fluence leads to smaller terahertz beam size, which is consistent with the results in section 5.2.

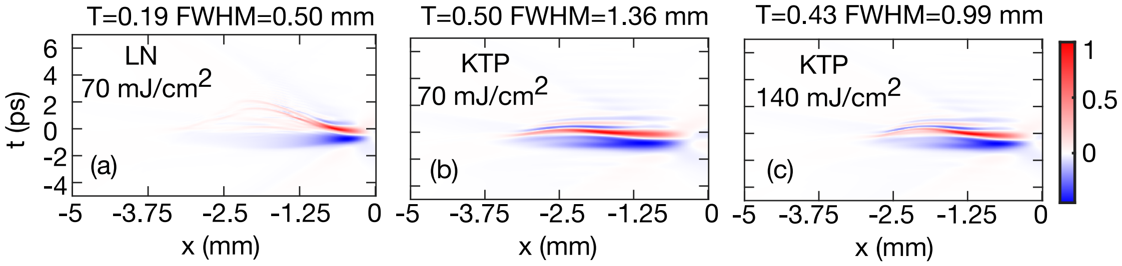

Figure 35: (a) represents the terahertz electric field generated by the LN. (b) and (c) represent the terahertz electric field generated by KTP with input pump fluence 70 mJ/cm^2 and 140 mJ/cm^2 respectively. The Fresnel transmission is represented by T and the FWHM indicates the output terahertz beam size.

Part III

Terahertz generation in periodically poled lithium niobate

7 Multi-cycle terahertz generation

Sections 7.1-7.10 are published in the work done by L. Wang et.al.[85].

7.1 Introduction

Multi-cycle terahertz has a wide range of applications, such as spectroscopy[10;11;12], semiconductor exciton excitation[13], spin dynamics control[6;86] and linear electron acceleration. These applications highly benefit from high energy terahertz sources[8;14;15]. In particular, applications like particle acceleration place steep requirements on a few millijoules of single/multi-cycle terahertz pulse energy to enable bunch manipulation in the relativistic regime. Such performance is largely contingent on increasing the terahertz generation efficiency towards the percent level and beyond.

Different approaches have addressed the generation of few-cycle terahertz pulses, including four wave mixing in ambient air[34], plasma driven effects in air[87], terahertz emission from photoconductive switches[88;89], tilted-pulse-fronts[59] and echelons[68;72;90]. In addition, there are techniques available for the generation of multi-cycle terahertz radiation. Quantum cascade lasers are attractive due to their compactness and production simplicity in its use in the spectral range > 1 THz despite their limited tunability[20;21;22]. Molecular gas lasers can provide high terahertz energies but are less tunable in terms of the generated terahertz frequency[23]. Free electron based terahertz sources are ideal in providing high energy multi-cycle terahertz pulses but are less accessible and are even more challenging for a compact implementation[91;92;93]. Laser based multi-cycle terahertz generation can leverage on developments in solid-state laser technology to enable compact coherent terahertz sources with high conversion efficiency at low terahertz frequency (<1 THz)[24;25;26]. This study revolves around the generation of high energy terahertz pulses in the multi-cycle (narrowband) regime.

Laser-driven terahertz generation utilizes the second order nonlinearity of the nonlinear material to perform difference frequency generation. GaAs, CdTe, InP[94;95;96] HMQ-TMS[97], $LiNbO_3$[98], GaP, ZnTe[99] and DAST[100;101] are nonlinear materials that have received significant attention. Multi-cycle terahertz generation in periodically poled Lithium Niobate (PPLN) was initially demonstrated by Lee et al.[98]. Recent research efforts focused on terahertz generation in PPLNs with various pump pulse formats such as chirp and delay, pulse-train and cascaded optical parametric amplification[24;65;102]. To our knowledge, the highest experimentally achieved conversion efficiency for multi-cycle terahertz generation in PPLN is around 0.15%[103;104].

Increasing the optical to terahertz generation/conversion efficiency in laser-based schemes is often hindered by several challenges. The first limitation is introduced by the Manley-Rowe relation[105] obtained after the assumption of single photon conversion. This limitation can be overcome by a cascaded second order process (repeated energy down-conversion of pump photons to terahertz photons)[102;106]. The damage threshold of the nonlinear crystal imposes another challenge. Large pump electric field strength induces optical breakdown and damage to the material, which also limits the achievable terahertz efficiency[107]. Another challenge is introduced by the terahertz absorption of the material. This challenge can be overcome by cryogenic cooling[108;109], since the temperature decrease impedes thermal phonon excitation and, therefore, considerably reduces the terahertz absorption. Additionally, it was found by Lee et al. that cooling of the nonlinear crystal increases the terahertz generation efficiency[110].

7.2 Phase matching

Phase matching ensures that a proper phase relationship between the interacting waves is maintained along the propagation direction. Only if that condition is fulfilled, an effective nonlinear interaction can be obtained. A conceptual illustration of the phase matching is shown in Fig. 36. Figure 36(a,b) represent the out-of-phase electric fields and the resulting total field respectively. Figure 36(c,d) represent the in-phase situation. It can be seen that, in the out-of-phase case, due to the destructive interference, the different electric fields cancel out each other, leading to a zero total field whereas in the in-phase case, an enhanced final field is obtained.

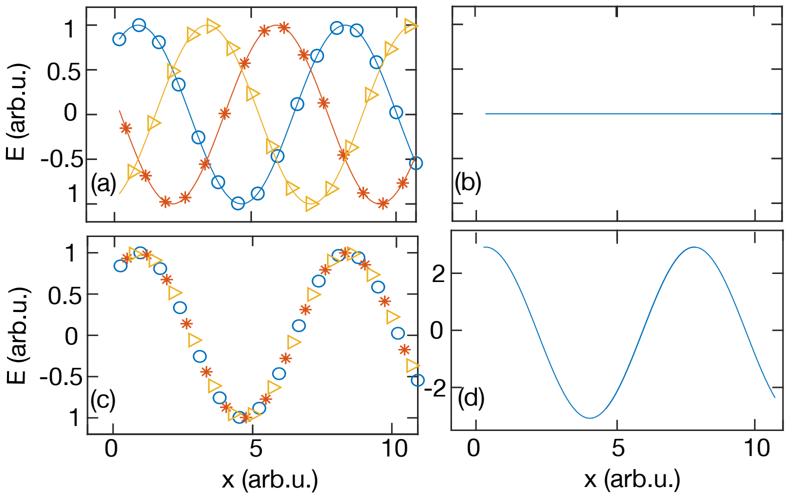

Figure 36: Illustration of the phase matching concept. (a) and (c) represent 3 out-of-phase and 3 in-phase electric fields respectively. (b) and (d) are the resulting total fields.

PPLN utilizes the quasi-phase-matching method where, along the propagation direction of the optical pump, the second nonlinear coefficient of the lithium niobate forms a periodic pattern by flipping the sign (see Fig. 37).

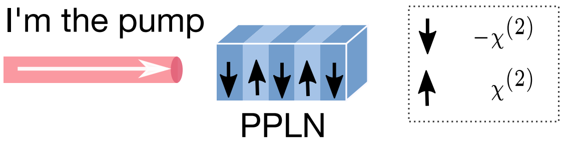

Figure 37: Schematic illustration of the PPLN, where χ^2 is the second order susceptibility of lithium niobate. The adjacent sections $\chi^{(2)}$ and $-\chi^{(2)}$ together form a period Λ ($\chi^{(2)}$ plus $-\chi^{(2)}$ is one period).

In PPLN, the pump pulse is chosen to be linearly polarized along the extraordinary optical axis of $LiNbO_3$ in order to maximize the effective second order nonlinear coefficient

$d_{33} = \frac{1}{2}\chi^{(2)}_{333} = -\frac{1}{4}n^4(\omega)\gamma_{333} = 168\,\mathrm{pm/V}$[24;65;111;112].

$$\begin{bmatrix} P_1^{NL(2)} \\ P_2^{NL(2)} \\ P_3^{NL(2)} \end{bmatrix} = 2\epsilon_0 \begin{bmatrix} 0 & 0 & 0 & 0 & d_{15} & -d_{22} \\ -d_{22} & d_{22} & 0 & d_{15} & 0 & 0 \\ d_{15} & d_{15} & d_{33} & 0 & 0 & 0 \end{bmatrix} \begin{bmatrix} |E_1|^2 \\ |E_2|^2 \\ |E_3|^2 \\ E_2E_3^* + E_2^*E_3 \\ E_1E_3^* + E_1^*E_3 \\ E_1E_2^* + E_1^*E_2 \end{bmatrix} \tag{87}$$

In Eq. (87), subscripts 1 and 2 represent the ordinary axes and 3 represents the extraordinary axis[47]. Axes 1 and 2 are identical at the first order ($n_{o1} = n_{o2}$), which is known as uniaxial birefringence. However, in the second order, the o axes are not identical. This explains why d_{ij} matrix elements are not identical on 1 and 2 axes. With the linearly polarized input pump pulse $\hat{\mathbf{E}} = (0, 0, E_3)$ along the extraordinary axis, the second order polarization term driving the terahertz field is also linearly polarized along the same direction ($P_3^{\mathrm{NL}(2)} = 2\epsilon_0 d_{33}|E_3|^2$).

The phase-matching condition shown in Eq. (88) ensures that the terahertz pulses generated at different positions of the PPLN crystal can add up in phase provided:

$$\begin{aligned} &\Omega[1/v_{\mathrm{THz}}(\Omega) - 1/v_{\mathrm{g}}(\omega)]\frac{\Lambda}{2} = \pi + 2\pi N \\ &N = 0, 1, 2, 3.... \end{aligned} \tag{88}$$

where Λ is the period of PPLN, Ω is the terahertz angular frequency, ω is the pump angular frequency, v_{THz} is the phase velocity of terahertz pulse and v_g is the group velocity of the pump pulse. Note that for a given PPLN structure, there is more than one terahertz frequency fulfilling the phase-matching condition ($\Omega_N = \Omega_0 \times (1 + 2N)$)

7.3 Coupled wave equations in cylindrical coordinate

I choose to perform calculations on a slice along the radial axis in cylindrical coordinates as shown in Fig. 38. For high energy terahertz generation, the usage of large crystals is mandatory due to the limited damage threshold of the nonlinear materials. Using the state-of-the-art fabrication technology, PPLN crystals as large as 1 cm × 1 cm transverse dimensions and few centimeters in length are realizable[113]. The propagation of the pump and terahertz beams in bulk PPLN crystals resemble the propagation of linearly polarized beams in a square waveguide. However, the waveguide dimensions are far larger than the wavelength of both pump and terahertz in the crystal. As a result, the effect of the waveguide boundaries become negligible.

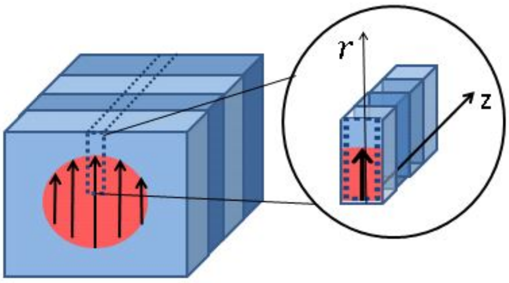

Figure 38: Schematic illustration of the simulated geometry: the dark thick arrows represent the polarization direction of both pump and terahertz beams. The polarization direction is aligned with the extraordinary optical axis of PPLN. The origin of the cylindrical coordinate is at the center of the beam. r and z represent the transverse and propagation directions, respectively.

Consequently, the entire problem reduces to solving the scalar coupled wave equations with the ansatz $E(\omega, r, z) = A(\omega, r, z)e^{-ik(\omega)z}$, considering the slowly varying amplitude approximation. The governing equations of the field amplitude of pump and terahertz beams read as:

$$\frac{\partial A_{\mathrm{op}}(\omega,r,z)}{\partial z} = \frac{-i}{2k(\omega)}\frac{1}{r}\frac{\partial}{\partial r}\left(r\frac{\partial A_{\mathrm{op}}(\omega,r,z)}{\partial r}\right) - \frac{i\varepsilon_0 n(\omega) n_2 \omega}{2}\mathscr{F}\{|A_{\mathrm{op}}(t,r,z)|^2 A_{\mathrm{op}}(t,r,z)\}$$
$$-\frac{i\omega\chi^{(2)}_{\mathrm{eff}}(z)}{2n(\omega)c}\int_{-\infty}^{\infty} A_{\mathrm{op}}(\omega+\Omega,r,z)A^*_{\mathrm{THz}}(\Omega,r,z)e^{i\triangle kz}d\Omega \tag{89}$$

$$\frac{\partial A_{\mathrm{THz}}(\Omega,r,z)}{\partial z} = \frac{-i}{2k(\Omega)}\frac{1}{r}\frac{\partial}{\partial r}\left(r\frac{\partial A_{\mathrm{THz}}(\Omega,r,z)}{\partial r}\right) - \frac{\alpha(\Omega)}{2}A_{\mathrm{THz}}(\Omega,r,z)$$
$$-\frac{i\Omega\chi^{(2)}_{\mathrm{eff}}(z)}{2n(\Omega)c}\int_{-\infty}^{\infty} A_{\mathrm{op}}(\omega+\Omega,r,z)A^*_{\mathrm{op}}(\omega,r,z)e^{i\triangle kz}d\omega \tag{90}$$

In Eqs. (89) and (90), A_{op} and A_{THz} stand for the electric field amplitude of the optical pump and the terahertz beam respectively; $\mathscr{F}$ denotes the Fourier transform operator; ω and Ω are the optical and terahertz angular frequencies respectively; k represents the wavenumber; α denotes terahertz absorption; n_2 represents the nonlinear refractive index and n represents the refractive index. The effective nonlinear coefficient is written as $\chi^{(2)}_{\text{eff}} = \chi^{(2)}_{333}(z)$ in the last terms on the right hand side of Eqs. (89) and (90). The term $e^{i\triangle kz} = e^{i(k(\Omega)+k(\omega)-k(\omega+\Omega))z}$ evaluates phase mismatch between the propagation of the terahertz beam and the optical pump. The term $e^{i\triangle kz}$ together with the term in the first order Fourier expansion series of $\chi^{(2)}_{333}(z)$, leads to the phase-matching condition[65].

On the right hand side of Eqs. (89) and (90), the first terms correspond to the transverse spatial dependence of the propagation, describing beam divergence due to diffraction. In Eq. (89), the second term describes the impact of SPM on the optical beam which is independent of the phase-matching condition. As one can see, I consider a frequency dependent SPM effect which implicitly includes the effect of self-steepening. This can be shown using the following derivation:

$$\begin{aligned}
&\omega_0 \mathscr{F}\left\{ |A_{\text{op}}(t,r,z)|^2 A_{\text{op}}(t,r,z) - \frac{i}{\omega_0} \frac{\partial |A_{\text{op}}(t,r,z)|^2 A_{\text{op}}(t,r,z)}{\partial t} \right\} \\
&= \omega_0 \mathscr{F}\{|A_{\text{op}}(t,r,z)|^2 A_{\text{op}}(t,r,z)\} + (\omega - \omega_0)\mathscr{F}\{|A_{\text{op}}(t,r,z)|^2 A_{\text{op}}(t,r,z)\} \\
&= \omega \mathscr{F}\{|A_p(t,r,z)|^2 A_{\text{op}}(t,r,z)\}.
\end{aligned}$$

where the first and second terms correspond to the SPM effect at ω_0 and self-steepening, respectively. Additionally, by considering radially dependent SPM, self-focusing is considered. The third term captures two important effects. One is the DFG term $A_{\text{op}}(\omega+\Omega)A^*_{\text{THz}}(\Omega)$ term which describes the frequency down-shift of the pump, and the other is the $A_{\text{op}}(\omega-\Omega)A_{\text{THz}}(\Omega)$ term which describes the back conversion from terahertz to the pump beam (sum-frequency generation)[114]. The second and third terms on the right hand side of Eq. (90) evaluate the effects of terahertz absorption and DFG processes respectively.

Our 2-D calculations in cylindrical coordinates allow for the possibility of including the spatial variation of the beam, diffraction and self-focusing. This can not be addressed by a 1-D calculation.

7.4 Numerical method simulation parameters

Various finite difference methods can be used for solving Eqs. (89) and (90). In this study, a split step Fourier method is used to compute the integral terms corresponding to the nonlinear polarization terms containing n_2 and $\chi^{(2)}_{\text{eff}}$. The second order derivative in the r direction is expressed by a conventional 3-point finite difference method as shown by Eq. (91) in Section (7.5). Ultimately, the values of A_{op} and A_{THz} are updated throughout the propagation distance z using the low-storage Runge-Kutta method[115]. The entire method leads to an explicit update algorithm along z rather than in time t. This is only valid when there is no reflection in the system (i.e only forward propagation along z is involved). The 3-point finite difference method takes advantage of the tridiagonal matrix of the discretization along the r direction, thus reducing computational cost. A combination of split step, explicit finite difference, and low-storage Runge-Kutta methods highly enhance the computational performance. Using other finite difference methods such as the Crank-Nicolson method is also possible. However, this implicit method necessitates the inversion of a finite difference matrix for each frequency and increases computational cost. Additionally, an angular spectrum method based on Hankel transformation[116] can be used but the approach suffers from a lack of the development of the fast Fourier transform (FFT) in Bessel series[117] and the boundary conditions are less straightforward to be implemented. Our calculation is performed in C++ with MPI and OpenMP for code parallelization. Details of the numerical method can be found in Section (7.5).

7.5 Finite difference method

The finite difference methodology for solving Eq. (89) is presented. Equation (90) can be solved by following the same procedure. By defining $r_j^+ = \frac{1}{2}(r_{j+1} + r_j)/(\triangle r^2 r_j)$, $r_j^- = \frac{1}{2}(r_{j-1} + r_j)/(\triangle r^2 r_j)$, where $\triangle r$ is the step size in the r dimension and r_j represents a mesh point at a specific radial position, one can obtain the discretized form of the second order derivative as shown in Eq. (91).

$$\frac{1}{r_j}\frac{\partial}{\partial r}\left(r_j\frac{\partial A_{\mathrm{op}}(\omega_m, r_j, z_k)}{\partial r}\right) = r_j^- A_{\mathrm{op}}(\omega_m, r_{j-1}, z_k) - (r_j^- + r_j^+)A_{\mathrm{op}}(\omega_m, r_j, z_k) + r_j^+ A_{\mathrm{op}}(\omega_m, r_{j+1}, z_k) \tag{91}$$

Equation (91) can be written in a matrix multiplication form as shown on the right hand side of the last column in Eq. (94) where the r_i related matrix is denoted as a tridiagonal matrix $\mathbf{M_R}$ as shown in Eq. (92).

$$\mathbf{M_R} = \begin{array}{cc} & \xleftrightarrow{\qquad\qquad N_r + 2 \qquad\qquad} \\ N_r \updownarrow & \begin{pmatrix} -r_1^- & r_1^+ + r_1^- & -r_1^+ & 0 & 0 & \dots & 0 \\ 0 & -r_2^- & r_2^+ + r_2^- & -r_2^+ & 0 & \dots & 0 \\ 0 & 0 & -r_3^- & r_3^+ + r_3^- & -r_3^+ & \dots & 0 \\ \vdots & \vdots & \vdots & \vdots & \ddots & \vdots & 0 \\ 0 & 0 & 0 & \dots & -r_{N_r}^- & r_{N_r}^+ + r_{N_r}^- & -r_{N_r+1}^+ \end{pmatrix} \end{array} \tag{92}$$

Equation (89) can be written as Eq. (93) where $P^{\mathrm{NL}}(\omega_m, r_j, z_k)$ represents all the second and third nonlinear polarization terms.

$$\frac{\partial A_{\mathrm{op}}(\omega_m, r_j, z_k)}{\partial z} = P^{\mathrm{NL}}(\omega_m, r_j, z_k) + \frac{i}{2k(\omega_m)}[-r_j^- A_{\mathrm{op}}(\omega_m, r_{j-1}, z_k) + (r_j^- + r_j^+)A_{\mathrm{op}}(\omega_m, r_j, z_k) - r_j^+ A_{\mathrm{op}}(\omega_m, r_{j+1}, z_k)] \tag{93}$$

Equation (93) can be written in matrix form as Eq. (94) where N_r, N_ω are the number of the mesh grids at r and ω dimension respectively. Each color of the corresponding column vector represents the coupled wave equation at a specific frequency ω_m. In Eq. (94), the 2-D matrix of angular frequency (ω) and radius (r) on the left hand side is updated by a low-storage Runge-Kutta method[115]. The electric field elements at the same position r_j with different frequencies are mixed by the nonlinear polarization P^{NL}. The electric field elements of the same frequency ω_m at different positions in r are mixed by $\mathbf{M_R}$ (e.g diffraction). The total number of the mesh points in r dimension is $N_r + 2$. The extra 2 points $A_{\mathrm{op}}(\omega, r_0, z), A_{\mathrm{op}}(\omega, r_{N_r+1}, z)$, marked with dashed boxes, are "ghost points". The "ghost points" together with the two columns marked by dashed lines in

$\mathbf{M_R}$ in Eq. 92 are used to construct boundary conditions.

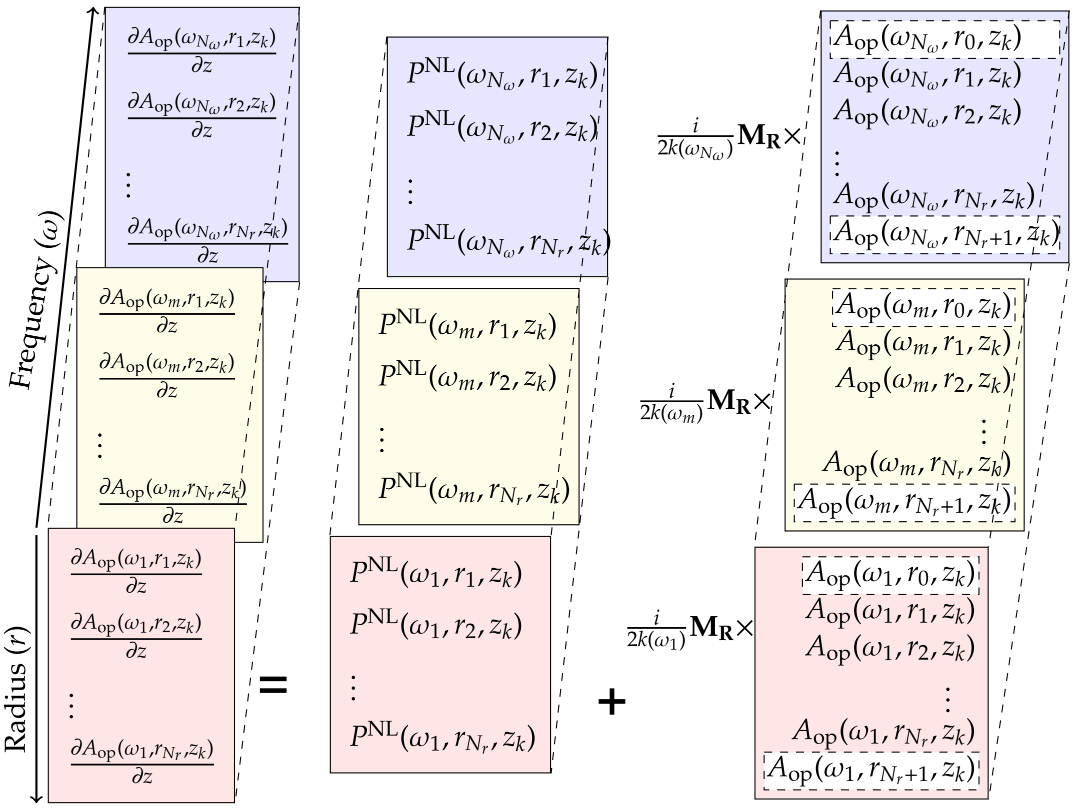

(94)

7.6 Boundary conditions

The boundary conditions are enforced to the solution by the elements in the dashed boxes in Eq. (94), and $\mathbf{M_R}$ matrix in Eq. (92). For the mesh points in r dimension, the $r = 0$ singularity is avoided by defining $r_0 = 3\Delta r$, and thus $r_1^- = \frac{1}{2}(r_0 + r_1)/(\Delta r^2 r_1)$. The "boundary condition" near r_1 is confined by the symmetry at the origin of the cylindrical coordinate itself (e.g $\frac{\partial A_{\text{op}}(\omega,r,z)}{\partial r}|_{r=r_1} = 0$). Thus,

$$A_{\text{op}}(\omega, r_0, z) = A_{\text{op}}(\omega, r_1, z) \tag{95}$$

For the boundary condition at r_{N_r}, three different conditions can be applied. Note that as shown in Fig. (38), in the calculated area the polarization of the field is perpendicular to the boundary. Of course with the same numerical method, any polarization at the boundary can be considered. However, the boundary condition has to be changed accordingly.

1. Dirichlet boundary:
   This condition represents the interface from PPLN crystal (n_{op}) to air (n). Due to Gauss's law in maxwell equation $\iint \overrightarrow{\mathbf{D}} \cdot \mathbf{d}\overrightarrow{\mathbf{S}} = 0$. One can get

   $$A_{\text{op}}(\omega, r_{N_r+1}, z) = A_{\text{op}}(\omega, r_{N_r}, z)\frac{n_{\text{op}}^2 r_{N_r}}{n^2 r_{N_r+1}} \tag{96}$$

   If the field polarization is parallel to the contact surface of the dielectric (PPLN) and the metal cladding outside the PPLN, one can also apply a reflective boundary condition.

   $$A_{\text{op}}(\omega, r_{N_r+1}, z) = 0. \tag{97}$$

   This is equivalent to the situation where electric field is reflected by a mirror.

2. Transparent boundary:[118]
   This boundary represents the situation where the boundary has no effect on the field as the field propagates through the calculation boundary. This kind of boundary is also equivalent to the situation when Eq. (89) and (90) are solved by angular spectrum method. The condition can be written as[118].

   $$A_{\text{op}}(\omega, r_{N_r+1}, z_{k+1}) \approx A_{\text{op}}(\omega, r_{N_r}, z_{k+1})\frac{A_{\text{op}}(\omega, r_{N_r+1}, z_k)}{A_{\text{op}}(\omega, r_{N_r}, z_k)} \tag{98}$$

7.7 Numerical error and efficiency estimation

In numerical calculations, generally two types of errors are studied. One is the round-off error. Due to the limited accuracy of how the computer store numbers, most non-integer numbers cannot be represented in a computer without committing an error[119]. The other is the Truncation error. This type of errors arise when an infinite process is replaced by a finite one, such as approximating an integral by a sum, approximating an ordinary differential equation by a finite difference method, and approximating a floating point number with a given significand[120].

In order to estimate the performance of the numerical package developed in this chapter, the numerical error and the efficiency are presented in Fig. 39. In Fig. 39(a) the relative error is defined as

$$\left|f_{\mathrm{num}} - f_0\right| / f_0$$

where f_0 is the analytical solution and f_{num} is the numerical solution. In Fig. 39(b), the time axis is defined as t/t_0 where t is the time consumed with a given number of cores and t_0 is the time consumed by minimum number of cores (5).

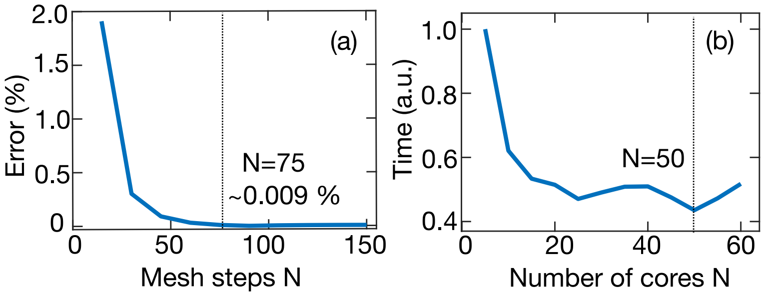

Figure 39: Numerical error and efficiency estimation. (a) shows numerical error versus the mesh step size. (b) shows the efficiency enhancement with respect to the number of cores used in the parallelization. The dashed vertical lines represent the choices used for following simulations.

7.8 Two-line input pump spectrum

Terahertz generation with pulse trains is effective in mitigating walk-off and yields high conversion efficiencies[65]. In the remainder of this thesis, the simulations are based on pump pulses consisting of two narrow spectral lines separated by the desired terahertz frequency ($\Omega_0 = 2\pi\times0.3$ THz). This forms a pulse train (beat note) with each sub-pulse separated by a time $2\pi/\Omega_0$, i.e. the terahertz electric field period. In this section, I base all simulations for terahertz generation centered at 0.3 THz due to its amenability for electron acceleration. The overarching conclusions may however be extended to other frequencies as well. The simulation parameters are tabulated in Table (7).

The refractive index and absorption (α) of terahertz radiation at 80 K and 0.3 THz are obtained from linear interpolation of the experimental data between temperatures 50 K

Table 7: Simulation parameters with two-lines input

Parameters	**Values**
n_2[121]	$1.25 \times 10^{-19}\,\mathrm{W/m^2}$
$\chi^{(2)}_{\mathrm{eff}} = \chi^{(2)}_{333}$ [24;65;111;112]	$2 \times 168\,\mathrm{pm/V}$
Super-Gaussian Order M	5
Ω_0	$2\pi \times 0.3\,\mathrm{THz}$
PPLN Period Λ	$374.1\,\mu\mathrm{m}$
$\alpha(\Omega_0)$[122]	$1.4\,/\mathrm{cm}$
Damage Fluence F_d[65]	$10\sqrt{\tau_{\mathrm{FWHM}}/(2 \times 10\,\mathrm{ns})}\,\mathrm{J/cm^2}$
Temperature	$75\,\mathrm{K}$
Input Pump Pulse Electric Field Format	
Two-lines frequencies $(\omega_0, \omega_0 + \Omega_0)$	$291.26\,\mathrm{THz}$, $291.56\,\mathrm{THz}$
$E(\omega) \propto e^{-(\omega-\omega_0)^2\tau^2_{\mathrm{FWHM}}/(8\ln 2)} + e^{-(\omega-\omega_0-\Omega_0)^2\tau^2_{\mathrm{FWHM}}/(8\ln 2)}$	
$E(t) \propto e^{i\omega_0 t} e^{-2\ln 2\left(t/\tau_{\mathrm{FWHM}}\right)^2}\left[1 + e^{i\Omega_0 t}\right]$	
$E(r) \propto e^{(-r^2/2\sigma^2)^M}$	

and 100 K from[122]. The material absorption at optical wavelengths, i.e. the pump absorption, is neglected and the refractive index is fitted to a Sellmeier equation[123]. I assume a super-Gaussian spatial distribution ($M = 5$) and a Gaussian temporal profile for the optical pump. This is also the case for high power lasers. Additionally, a super-Gaussian spatial distribution ensures that the generated terahertz radiation is homogeneous in the transverse r dimension and also minimizes the damage due to peak fluence of the pump compared to a Gaussian spatial profile. The input pump pulse energy, which follows from spatial and temporal integrations of the electric field

defined in Table. 1, is given by

$$\text{Energy} = \frac{2\pi\sigma^2\Gamma(\frac{M+1}{M})F_\text{d}}{2^{\frac{1}{M}}} \tag{99}$$

7.9 Terahertz efficiency in terms of pump pulse duration

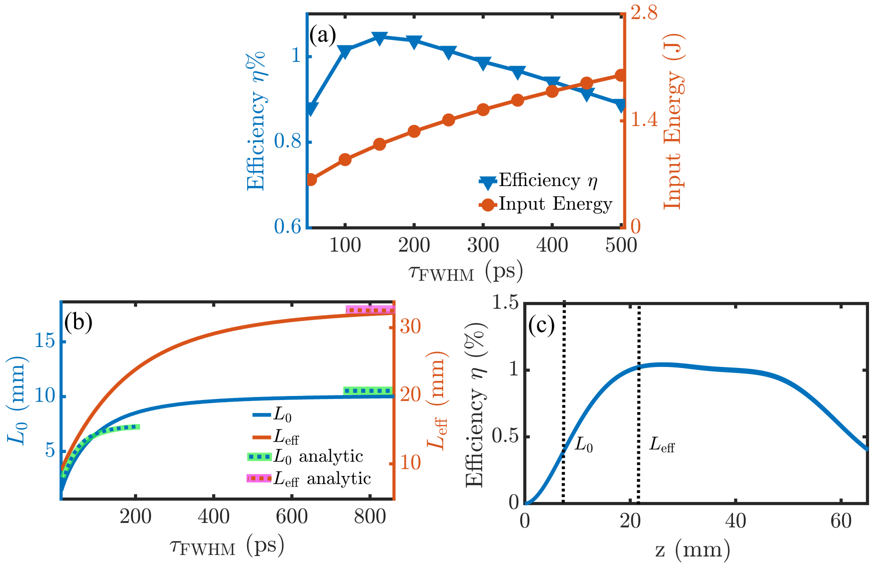

Figure 40: Numerical results of the terahertz generation in a single stage: (a) shows the conversion efficiency versus the pump pulse duration. The maximum efficiency $\eta = 1.05$ % is obtained at $\tau_\text{FWHM} = 150\,\text{ps}$. The input pump energy is calculated from Eq. (99) with the pump beam size $\sigma = 5\,\text{mm}$. (b) shows the L_0, L_eff versus pump pulse duration. (c) shows the terahertz efficiency versus the propagation distance for $\tau_\text{FWHM} = 150\,\text{ps}$, where the steepest efficiency increase rate (L_0) and effective length (L_eff) are labeled.

The crucial parameters in designing a complete terahertz source are the pulse duration of the pump and the necessary length of the PPLN crystal. As one can see in Eq. (99), longer pulse durations allow higher input energy, but simultaneously necessitate longer interaction length, which in turn intensifies the effects caused by terahertz absorption. The optimal pump pulse duration is found to be 150 ps with conversion efficiency $\eta = 1.05$ % as shown in Fig. 40(a,c). In order to define the optimal PPLN length L_eff, we introduce the length parameter L_0 where the efficiency increase is most rapid. This is obtained at $d^2\eta(z)/dz^2|_{z=L_0} = 0$. I define L_{eff} as:

$$\frac{1}{e}\frac{d\eta(z)}{dz}|_{z=L_0} = \frac{d\eta(z)}{dz}|_{z=L_{\text{eff}}}. \tag{100}$$

One should avoid choosing L_{eff} at $d\eta(z)/dz = 0$, because the plateau length in Fig. 40(c) increases with the increase of the pump pulse duration and $d\eta(z)/dz = 0$ occurs approximately in the middle of the plateau. Within the range of the plateau, the amount of generated terahertz radiation equals to the absorbed amount. Consequently, the optimal L_{eff} should be chosen at the onset of the plateau to avoid unnecessarily long crystals.

Since the effective length is related to the pump pulse duration, in order to get more insight into this problem, I begin with a 1-D undepleted model. Consequently, Eq. (90) can be written as Eq. (101).

$$\begin{aligned} A_{\text{THz}}(\Omega, z) = & \frac{-i\Omega\chi^{(2)}_{\text{eff}}}{\pi n(\Omega)c}\int_0^\infty A_{\text{op}}(\omega+\Omega, r, z)A^*_{\text{op}}(\omega, r, z)d\omega\left[\frac{\exp(i\delta z) - \exp(-\alpha(\Omega)z/2)}{\alpha(\Omega)/2 + i\delta}\right] \\ = & P^{\text{NL}}(\Omega)\left[\frac{\exp(i\delta z) - \exp(-\alpha(\Omega)z/2)}{\alpha(\Omega)/2 + i\delta}\right] \end{aligned} \tag{101}$$

where ,

$$\delta = [k(\Omega) + k(\omega) - k(\omega+\Omega) - \frac{2\pi}{\Lambda}] = [\frac{\Omega}{c}(n(\Omega) - n_{\text{g}}(\omega)) - \frac{2\pi}{\Lambda}] \approx \frac{(n(\Omega_0) - n_{\text{g}}(\omega_0))}{c\tau_{\text{FWHM}}}. \tag{102}$$

In order to study the distance L_0 and L_{eff}, I calculate the second order derivative of $|A_{\text{THz}}|^2$ which is proportional to the efficiency η. By calculating $d^2|A_{\text{THz}}(\Omega, z)|^2/d^2z = 0$, one can get

$$\exp(-\alpha z/2) = \left[\cos(\delta z)/2 + 2\delta\sin(\delta z)/\alpha - 2\delta^2\cos(\delta z)/\alpha^2\right] \tag{103}$$

$$\begin{cases} \text{for short pump pulse, } \delta/\alpha \gg 1,\ 2\delta\sin(\delta z)/\alpha = 2\cos(\delta z)\delta^2/\alpha^2 \\ \Rightarrow L_0 = \tan^{-1}(\delta/\alpha)/\delta, \\ \\ \text{for long pump pulse, } \delta/\alpha \ll 1,\ \exp(-\alpha z/2) = \cos(\delta z)/2 \approx 1/2 \\ \Rightarrow L_0 = 2\ln(2)/\alpha,\ L_{\text{eff}} = 2\ln(2/(1-\sqrt{1-e^{-1}}))/\alpha \end{cases}$$

L_0 and L_{eff} variations in terms of the pump pulse duration are depicted in Fig. 40(b) where the results of analytic calculations are compared against numerical results. In Fig. 40(c), a efficiency decrease can be observed for large propagation distance z. This is due to the fact that the long interaction leads to a large spectral broadening. Due to the dispersion, newly generated pump frequencies do not precisely certify the phase-matching condition. Absorption together with the not perfectly phase-matched pump spectrum leads to the efficiency decrease.

7.10 Effects of transverse spatial variations of pump

High power terahertz generation demands high power lasers which usually suffer from phase front distortions and intensity modulations. In the following section, I investigate the influence of the spatial variation of the pump pulse on the terahertz generation process.

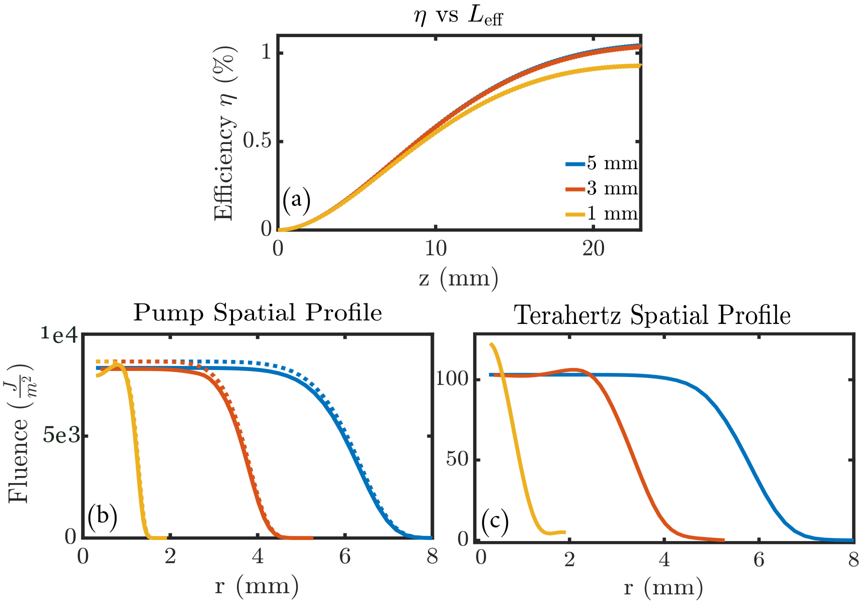

Figure 41: (a) shows the efficiency of terahertz generation versus propagation distance for various beam sizes. (b) shows the spatial profile of the input pump pulse (dashed lines) and output pump pulse (solid lines). (c) shows the output terahertz beam spatial profile. For different beam sizes, the peak fluence is kept constant. The output spatial profiles of both terahertz radiation and the pump are obtained at the end of the interaction length, i.e. $z = 25\,\text{mm}$.

Beam Size Dependence Here, I aim at exploring the dependence of the terahertz generation efficiency on the pump beam size. For this purpose, I perform simulations for a super-Gaussian ($M = 5$) pump beam with beam sizes $\sigma = 1\,\text{mm}$, $3\,\text{mm}$ and $5\,\text{mm}$, respectively. Figure 41 suggests that the terahertz beam size and spatial profile resemble the corresponding pump properties for large pump beam sizes.

It can be seen in Fig. 41(a) that the terahertz conversion efficiency is lower when $\sigma = 1\,\text{mm}$ compared to $\sigma = 3\,\text{mm}$ and $5\,\text{mm}$. The diffraction has a minor influence on the spatial profile of the pump pulse since the Rayleigh range ($\lambda \approx 1\,\mu\text{m}$) is about few tens of meters. In a super-Gaussian beam, smaller beam size leads to larger spatial phase gradient at the edge of the spatial profile. Therefore, as observed in Fig. 41(b), the self-focusing effect leads to the peak appearing at the edge of the 1 mm pump beam. The change of the spatial profiles of the terahertz beams in Fig. 41(c) is due to the diffraction of the super-Gaussian beam[124;125]. It can be seen that for a 1 mm terahertz beam, diffraction modifies the super-Gaussian profile to a Gaussian profile after 25 mm generation distance.

Influence of Pump Pulse Spatial Energy Fluctuation and Phase Fronts Variation The above results are obtained with perfect super-Gaussian pump spatial profiles and a flat spatial phase front. In order to examine the influence of spatial energy and phase front variations of the pump pulse on terahertz generation with the two-line pump spectrum, I studied 4 cases: (I) flat phase front with one of the pump spectral lines having a 5% modulation in the electric field strength. (II) flat phase front with both pump spectral lines having a 5% modulation in the electric field strength. (III) flat spatial profile with one of the pump spectral lines having modulation from $-\pi$ to π in the phase front. (IV) flat spatial profile with both of the pump spectrum lines having modulation from $-\pi$ to π in phase front.

In the following context, $E(\omega, r)$ denotes the electric field of the input pump pulse and $E_0(\omega, r)$ is the electric field with a perfect super-Gaussian spatial profile (σ=5 mm) and flat phase front. The interaction length is chosen to be $z = 25\,\text{mm}$ as in Fig. 41. $r_{\text{max}} = 8.5\,\text{mm}$ is the maximum distance of the calculated radial dimension.

Case I: One line with Cosine Electric Field Amplitude Modulation

$$\begin{cases} E(\omega, r) = E_0(\omega, r)(1 + 0.05\cos(2\pi \times 4r/r_{\text{max}})), & \omega \leq 2\pi \times 291.3\,\text{THz} \\ E(\omega, r) = E_0(\omega, r), & \omega > 2\pi \times 291.3\,\text{THz} \end{cases} \tag{104}$$

It can be seen in Fig. 42 that terahertz generation is not degraded by the intensity modulation in one of the spectral lines. Though the transverse intensity modulation can also induce spatial phase variations due to self-focusing, with our pump pulse parameters, the induced spatial phase variation is negligible.

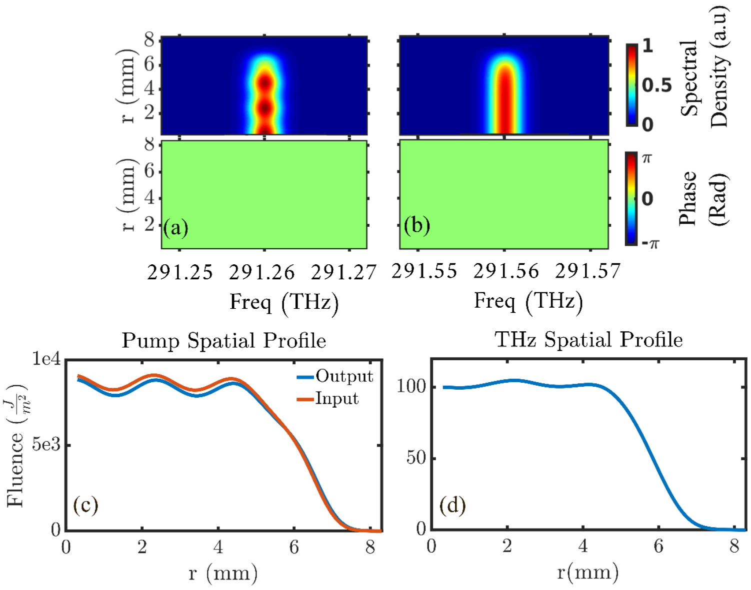

Figure 42: (a) and (b) show the spectral density (first row) and flat phase front (second row) of the input pump spectral lines. (c) shows the spatial profile of the input and output pump pulse. (d) shows the terahertz spatial profile.

Case II: Both lines with Cosine Electric Field Amplitude Modulation

$$E(\omega, r) = E_0(\omega, r)(1 + 0.05\cos(2\pi \times 4r/r_{\max})) \tag{105}$$

Fig. 43 suggests that the terahertz generation is not degraded when both lines are subjected to the same intensity modulation, which is expected from the Case I study.

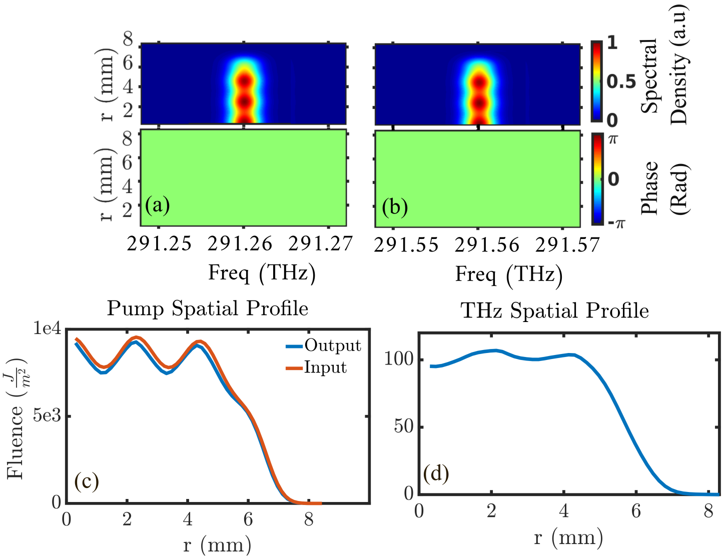

Figure 43: (a) and (b) show the spectral density (first row) and flat phase front (second row) of the input pump spectral lines. (c) shows the spatial profile of the input and output pump pulse. (d) shows the terahertz spatial profile.

Case III: Both lines with Cosine Phase Modulation

$$E(\omega, r) = E_0(\omega, r)e^{i\pi \cos(2\pi \times 4r/r_{\max})} \tag{106}$$

Fig. 44 suggests that if both of the pump lines are identically modulated in phase, the terahertz generation process is not degraded. The phase modulation induces self-focusing which can be observed in Fig. 44(c).

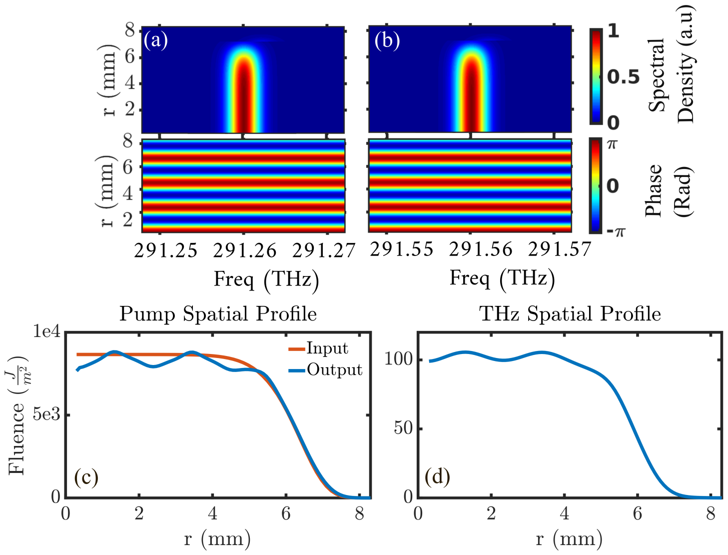

Figure 44: (a) and (b) show the spectral density (first row) and phase front (second row) of the input pump spectral lines. (c) shows the spatial profile of the input and output pump pulse. (d) shows the terahertz spatial profile.

Case IV: One line with Cosine Phase Modulation

$$\begin{cases} E(\omega, r) = E_0(\omega, r)e^{i\pi\cos(2\pi\times 4r/r_{\max})}, & \omega \leq 2\pi\times 291.3\,\text{THz} \\ E(\omega, r) = E_0(\omega, r), & \omega > 2\pi\times 291.3\,\text{THz} \end{cases} \tag{107}$$

Figure 45 indicates that a distortion in the phase front, not unusual for high power laser beams, strongly reduces the conversion efficiency. This is due to the nature of the difference frequency generation process, which transfers the phase difference between the two frequency lines of the optical pump to the terahertz beam at a thousand times longer wavelength. In turn, the modulated terahertz phase front suffers from strong diffraction, leading to destructive interference. Consequently, the terahertz conversion efficiency is greatly reduced and a strongly spatially modulated terahertz beam appears as shown in Fig. 45(d). The peaks in Fig. 45(c) are due to self-focusing, making it different from case III. In case III, since the phase fronts of both spectral lines are identical, the terahertz generated inherits a flat phase front. As a result, the cascaded frequencies newly generated in the optical region maintain the same phase front as the initial two-line spectra. However, in case IV since DFG creates a terahertz pulse with the phase difference of the pump spectral lines, the new pump frequency lines generated by the cascading process carry different phases. The later generated cascaded lines inherit multiple times of the original phase difference, forming an enormously curved phase front. Thus, strong self-focusing occurs.

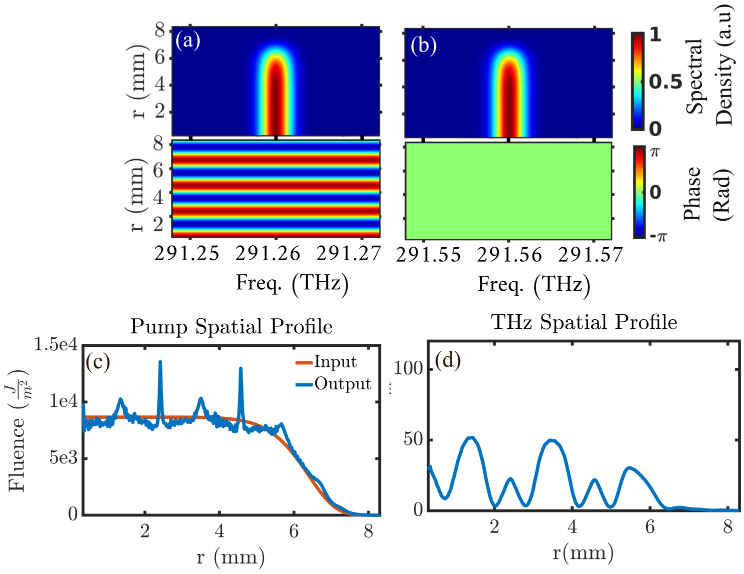

Figure 45: In (a,b) the first row shows the spatial profiles of the pump spectral lines and the second row represents the phase front of the corresponding spectral lines. (c) shows the pump input and output spatial profile. (d) shows the generated terahertz spatial profile.

7.11 High efficiency terahertz generation by pulse recycling

Previous work based on a 1D-propagation model[65], partially addressed the possibility of obtaining high efficiencies of several percent for optimal pump pulse formats. However, in practice, complex pump pulse formats are hard to engineer. Therefore, further innovations are necessary to achieve the desired percent level efficiencies. Here, I aim to alleviate these limitations by recycling the optical pump and separating the generated terahertz radiation in a staged approach, before significant terahertz absorption occurs. In this multi-stage architecture, consecutive stages utilize the same optical pump pulse. The terahertz pulse generated at each PPLN stage is then coupled out, circumventing the excessive terahertz absorption. A similar concept was experimentally tested by Chen et al.[126] with a two-stage system for single-cycle terahertz generation. However, in their system, the terahertz pulse generated in the first stage is also coupled into the second stage together with the pump pulse[126].

7.11.1 Terahertz efficiency enhancement with dispersion compensation

I suggest compensating the dispersion accumulated in the material of the pump pulse generated at the end of each stage before recycling it to the subsequent PPLN stage in order to enhance the conversion efficiency. In other words, before the pump pulse is recycled to stage N, an opposite dispersion is added to the pump pulse at the end of stage N-1 to cancel the dispersion obtained by propagation through the stage N-1. For the first and second stages, dispersion compensation can be realized by a prism or grating (i.e second and third order dispersion). For many stages, the cascading process broadens the spectrum drastically. Dispersion compensation for a large bandwidth beam can be challenging in practice since higher order dispersion needs to be taken into consideration. However, it still can be achieved with double chirped mirrors[127].

The simulation results comparing the terahertz spectra at the end of each stage with and without dispersion compensation are shown in Fig. 46(a,b). The resulting conversion efficiencies are shown in Fig. 46(c,d).

One can see that the terahertz conversion efficiency reduces subsequently after each stage without dispersion compensation. Since the terahertz generation broadens the pump spectrum via the cascading process, part of the broadened pump spectrum can not be phase matched for further cascading. In other words, different frequency elements in the pump spectrum pick up different phases due to dispersion in the PPLN via propagation. Consequently, the terahertz radiation generated by DFG from different spectral ranges of the pump pulse carries different phases, leading to partial destructive interference of the total generated terahertz radiation. Thus, the efficiency is degraded due to the dispersion. It can be seen in Fig. 46(b,d) that the efficiency can be significantly enhanced by dispersion compensation.

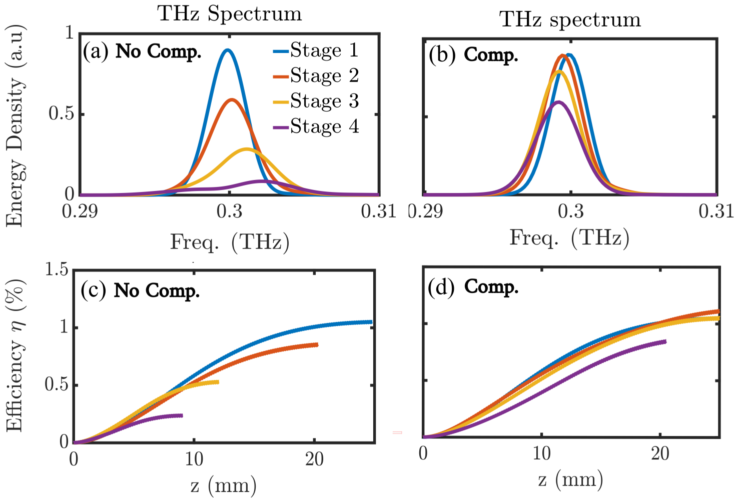

Figure 46: Comparison of a 4 stage system with input pump pulse parameters $\sigma = 5\,\text{mm}$, $\tau_{\text{FWHM}} = 150\,\text{ps}$. The effective length of each stage is chosen to be the distance where efficiency saturates. (a,c) depict the terahertz spectra generated after each stage and the conversion efficiency by recycling the pump pulse directly without dispersion compensation (No Comp.). (b,d) show the terahertz spectra and the conversion efficiency with pump pulse dispersion compensation (Comp.) after each stage.

7.11.2 Spectral dynamics of optical pump and terahertz pulses

Figure (47) depicts the temporal profile of the pump pulse with the short time Fourier transform (STFT) (i.e instantaneous spectrum) of the corresponding time range. The broadening of the pump pulse spectrum causes a reduction of the pulse duration, an increase in peak intensity and a drastic variation in the instantaneous spectrum of each sub-pulse (see Fig. 47(a,b)). The STFT in Fig. 47(b) indicates that the instantaneous spectrum in each sub-pulse forms a 'U' shape due to the cascading effect, leading to a drastic spectral variation in time. The maximum cascading (spectral down-shift) occurs where the highest peak intensity is present. The STFT in Fig. 47(c) suggests that the dispersion compensation alters the spectral distribution with respect to time. If a transform limited pump pulse, which has a uniform spectrum distributed over time, could be obtained after each stage, the terahertz efficiency could be greatly enhanced. However, the realization of such a process is challenging, since perfect compression of the 'U' shaped spectrum induced by SPM, the second order nonlinear effect, and dispersion, is not straightforward.

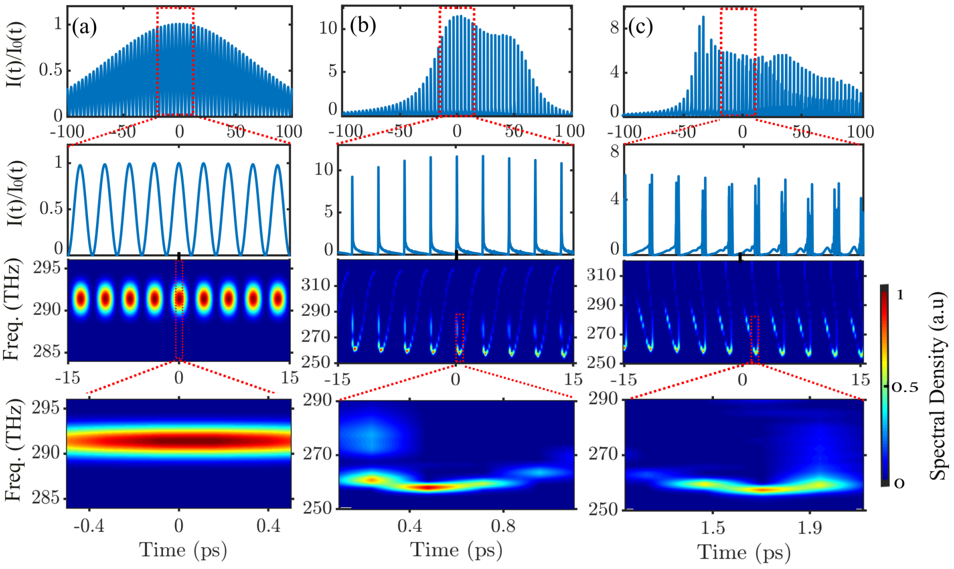

Figure 47: (a) shows the input pump pulse, (b) shows the output pump pulse after one 2.5 cm PPLN stage. (c) shows the output pump pulse after dispersion compensation by adding the opposite second order dispersion of Lithium Niobate at the pump center frequency (GDD= 6300 fs^2) to (b). The contour plot in the second and third rows are the short time Fourier transforms of the corresponding selected temporal range (indicated by the dotted red box).

Figure. 48 compares the spectral density (spatially dependent spectra in radial dimension r) of the terahertz generated at each stage for two cases with and without dispersion compensation. The terahertz beams generated with dispersion compensation follow a Gaussian-like spectrum, whereas those generated by direct pump pulse recycling have distorted spectral shapes, particularly in the last stage. This is due to the fact that the phase of the pump perturbed by dispersion influences the phase-matching condition of terahertz generation, and thus leads to a broader terahertz spectrum. Figure. 49 shows the comparison of the spectral density of the output optical pump at each stage without and with dispersion compensation. It can be seen that dispersion compensation boosts the cascading process and leads to greater pump spectral broadening. The results depicted in Fig. 46, Fig. 48 and Fig. 49 confirm that the terahertz conversion efficiency can be largely enhanced by pump pulse recycling with dispersion compensation.

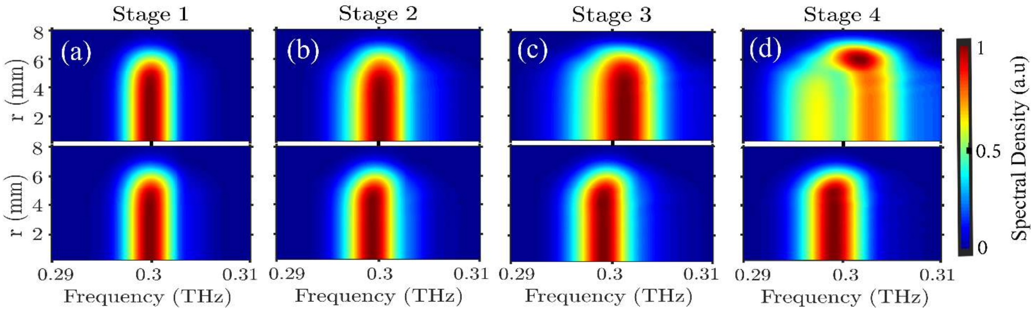

Figure 48: (a-d) show the terahertz spectral density generated by 4 consecutive stages respectively. The first and second rows show the terahertz spectra generated without and with dispersion compensation, respectively.

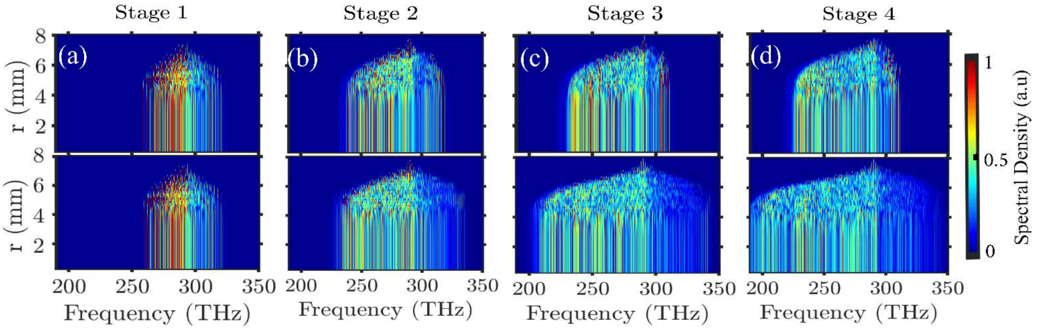

Figure 49: (a-d) represent pump pulse spectral density after each corresponding stage. The first and second rows show the pump pulse spectra at the output of each stage generated without and with dispersion compensation, respectively.

7.11.3 Quartz output coupler for beam separation

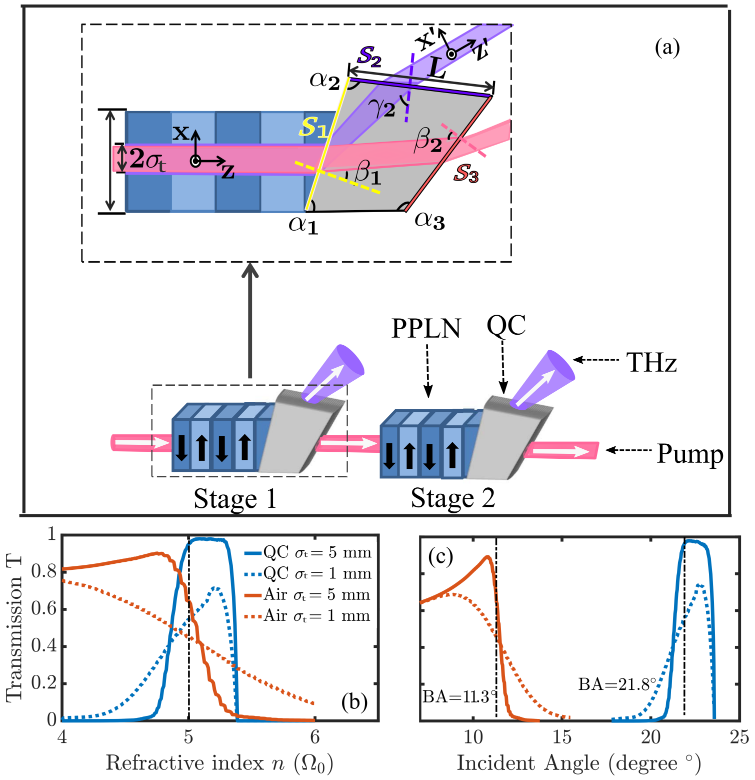

Figure 50: (a) Schematic illustration of the output coupler and the angle definitions. In (b) and (c), comparison of the terahertz energy transmission from PPLN to air for 'Air' and 'QC' cases are shown. Additionally, the transmission of the generated flat-top terahertz beam with different beam sizes $\sigma_t = 1$ mm (dashed lines) and $\sigma_t = 5$ mm (solid lines) are analyzed. (b) shows terahertz energy transmission versus the refractive index of the PPLN at the given Brewster angles (BA) at S_1 surface. The black dash-dotted line refers to the refractive index assumed for the calculation of Brewster's angles. (c) shows terahertz energy transmission versus the incident angle at surface S_1 with given refractive index where the black dash-dotted lines mark the BA at this refractive index.

Figure. 50(a) shows one possible arrangement of the multi-stage setup accounting for the subtlety of terahertz and optical beam separation. The output pump beam from the PPLN propagates at a certain angle with respect to the input pump pulse direction due to the refraction from the quartz coupler (QC). However, in the sketch, I do not depict this for simplicity of illustration. Incidence at Brewster angle plays a crucial role in this scheme in order to couple out and separate both pump and terahertz beams with high transmission efficiency from the PPLN to air ($n = 1$). Out-coupling of the terahertz beam from Lithium Niobate to air through a silicon coupler was first demonstrated experimentally and theoretically by Kawase et al.[128]. In this article, crystalline quartz is chosen as the material of the output coupler owing to its low absorption for terahertz radiation at 0.3 THz (0.01/cm)[129;130], large bandgap (12.5 eV)[131] which has lower nonlinearity and higher damage threshold compared to silicon or Lithium Niobate[52]. Additionally, the dispersion of quartz at both pump and terahertz frequencies is negligible for few centimeters of propagation[130;131]. I neglect the small influence of the quartz coupler on the optical pump and fully focus on the out-coupling of the terahertz radiation.

In Fig. 50(a), the inner angles of the bulk quartz coupler are represented by α_1, α_2, and α_3. This ensures that the terahertz beams experience Brewster incidence angles $\pi - \alpha_1$ and γ_2 at S_1 and S_2 surfaces, respectively. β_1 and β_2 are the output angles of the pump beam at the S_1 surface and the pump beam Brewster incidence angle at the S_3 surface, respectively. The refraction loss of the pump is negligible. S_3 can be chosen to be parallel to surface S_1 to further reduce angular deviation. Additionally, L (the length of the top edge of the quartz coupler) is the minimum distance that ensures sufficient spatial separation of pump and terahertz beams. Details of the equations used for calculating the involved angles can be found in Table 8, where $\sigma = 5\,\text{mm}$, $n_{\text{LN}}(\omega_0) = 2.1$, $n_{\text{Q}}(\omega_0) = 1.4$, $n_{\text{LN}}(\Omega_0) = 5$, $n_{\text{Q}}(\Omega_0) = 2$. The subscripts 'LN' and 'Q' correspond to PPLN and Quartz respectively.

Table 8: Quartz Coupler Parameters

Parameter	**Variable**	**Values**
β_1	$\sin^{-1}\left(\cos(\alpha_1)n_{\mathrm{LN}}(\omega_0)/n_{\mathrm{Q}}(\omega_0)\right)$	33.9°
β_2	$\tan^{-1}(1/n_{\mathrm{Q}}(\omega_0))$	35.5°
γ_2	$\tan^{-1}(1/n_{\mathrm{Q}}(\Omega_0))$	26.6°
α_1	$\tan^{-1}\left(n_{\mathrm{LN}}(\Omega_0)/n_{\mathrm{Q}}(\Omega_0)\right)$	68.2°
α_2	$\alpha_1 + \gamma_2$	94.8°
α_3	$\pi - \beta_1 + \beta_2 - \alpha_1$	113.4°
L	$2\sigma\cos(\beta_2)\cos(\alpha_1)/(\sin(\alpha_1 - \beta_1)\sin(\alpha_2))$	5.5 mm

Since the refractive index of the PPLN varies with temperature and manufacturing process, an output coupler with a reasonable tolerance is desired. In Fig. 50(b,c), comparison of two out-coupling cases 'Air' (red curves) and 'QC' (blue curves) is shown. In the case of 'Air' where no output coupler is utilized, the PPLN crystal is cut such that the terahertz pulse is incident at Brewster's angle ($\tan^{-1}(1/n_{\mathrm{LN}}(\Omega_0)) = \tan^{-1}(1/5) = 11.3°$) from PPLN to air directly. In the case of 'QC', the terahertz pulse is coupled out from the PPLN to air through the designed quartz coupler shown in Fig. 50(a) with Brewster incidence angle ($\tan^{-1}(n_{\mathrm{Q}}(\Omega_0)/n_{\mathrm{LN}}(\Omega_0)) = \tan^{-1}(2/5) = 21.8°$) on S_1 surface.

In both Fig. 50(b) and Fig. 50(c), the transmission window of the 'QC' case at $\sigma_{\mathrm{t}} = 5\,\mathrm{mm}$ (flat interval with terahertz energy transmission $T \approx 1$) is due to total internal reflection (TIR) at both the S_1 and S_2 surfaces. This window range reduces for the smaller terahertz beam size $\sigma_{\mathrm{t}} = 1\,\mathrm{mm}$ (i.e terahertz beam with larger angular divergence). The terahertz beam components with angular divergence larger than the TIR are filtered out, leading to lower energy transmission. This TIR induced transmission loss is particularly pronounced for the 'Air' case since the refractive index varies from $n_{\mathrm{LN}}(\Omega_0) = 5$ to $n_{\mathrm{Air}}(\Omega_0) = 1$. This large refractive index difference causes a sharp transmission drop at the incidence angle larger than Brewster angle. This explains why the transmission peak occurs at an angle smaller than Brewster's angle in the 'Air' case in Fig. 50(c). With larger beam size $\sigma_{\mathrm{t}} = 5\,\mathrm{mm}$, the transmission peak approaches the Brewster angle due to smaller angular divergence. It can be seen that from PPLN to air, the terahertz energy transmission at $\sigma_t = 1\,\text{mm}$ is around 45% and 55% for 'Air' case and 'QC' case respectively. The terahertz energy transmission at $\sigma_t = 5\,\text{mm}$ is around 63% and 96% for 'Air' case and 'QC' case respectively. With the given refractive index at the corresponding Brewster incident angle, a quartz coupler leads to higher transmission. More discussion can be found in section (7.11.4).

7.11.4 Terahertz spatial profile after quartz coupler

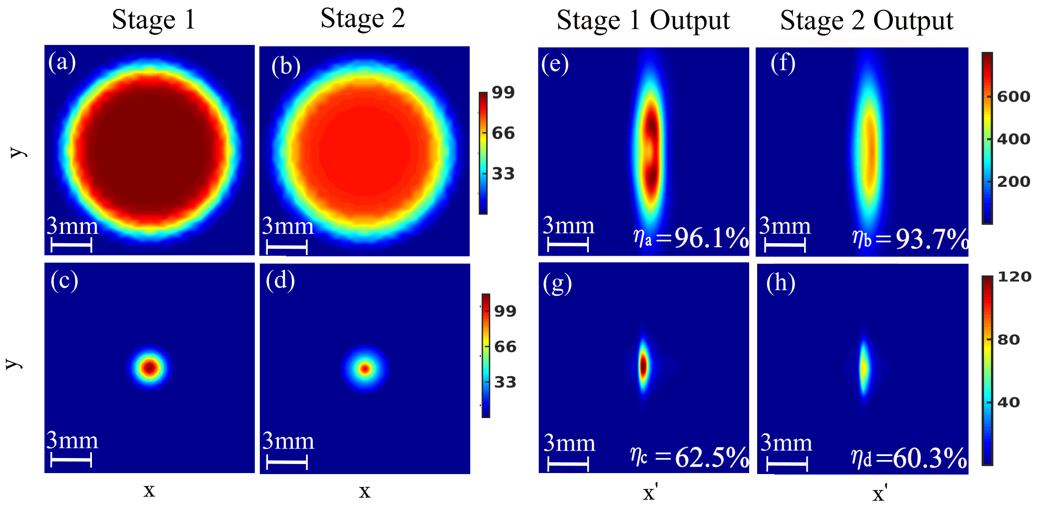

Figure 51: (a,b) and (c,d) represent terahetz spatial profiles in PPLN in $x - y$ coordinate before S_1 surface (see Fig. 50(a)) generated by a two-stage system with pump beam size $\sigma = 5\,\text{mm}$ and $\sigma = 1\,\text{mm}$ respectively. (e-h) represent coupled out terahertz spatial profiles of (a-d) after S_2 surface in $x' - y$ coordinate in the air. The color bar represents fluence in the unite of J/m^2. Each figure window size is 15 mm × 15 mm. Terahertz out-coupling efficiency from (a-d) to (e-h) is $\eta_a = 96.1\%, \eta_b = 93.7\%, \eta_c = 62.5\%, \eta_d = 60.3\%$ respectively.

The quartz coupler breaks the cylindrical symmetry of the PPLN. In order to calculate the terahertz spatial profile after the quartz coupler, I reconstruct the terahertz beam profiles in x-y coordinates from the numerical results in the cylindrical coordinates inside the PPLN before the incidence on the S_1 surface (see Fig. 50(a)). The refraction at the S_1, S_2 surfaces (see Fig. 50(a)) for p polarized light and the beam propagation in the quartz coupler is calculated by the angular spectrum method[132]. Figs. 51(a,b) and Figs. 51(c,d) correspond to terahertz spatial profiles generated with a pump beam size $\sigma = 5\,\text{mm}$ and $\sigma = 1\,\text{mm}$, respectively by a two-stage setup.

Note that with a pump beam size $\sigma = 5\,\text{mm}$, the terahertz spatial profile retains its flat top nature, whereas with $\sigma = 1\,\text{mm}$, the terahertz spatial profile reduces to a Gaussian as shown in Fig. (41). The corresponding transmitted spatial profiles after the S_2 surface in $x' - y$ coordinates in the air (see Fig. 50(a)) are shown in Fig. 51(e-h) with the terahertz out-coupling efficiency $\eta_\text{a} = 96.1\%, \eta_\text{b} = 93.7\%, \eta_\text{c} = 62.5\%, \eta_\text{d} = 60.3\%$ respectively. The influence of the S_1 and S_3 surfaces together with the propagation in the quartz coupler has a negligible effect on the pump spatial profile, i.e the spatial profile of the pump stays flat top but with a reduced size in the x' direction i.e $\sigma' = \sigma \tan(\beta_2)\cos(\beta_1)/\sin(\alpha_1) \approx 0.6\sigma$. The beam size of the terahertz radiation in the x' direction follows the same relation $\sigma'_\text{t} = \sigma_\text{t}\tan(\beta_2)/\tan(\alpha_1) \approx 0.2\sigma_\text{t}$. On the other hand, the refraction at S_1 and S_2 surfaces greatly changes the energy distribution of the flat top terahertz beams spatially (see Fig. 51(a,b,e,f)) while the Gaussian spatial profile remains unchanged (see Fig. 51(c,d,g,h)). The flat top function is a superposition of Hermite Gaussian modes in Cartesian coordinates. Thus, the final spatial profile of terahertz is a result of a superposition of all the Hermite Gaussian modes after refraction.

The terahertz beams coupled out by the QC could be combined by a power combiner with a specifically designed input coupler which matches the terahertz beam profile to the mode of the power combiner[133]. This investigation is beyond the scope of this article and will be presented in a separate study. For an ideal symmetric power combiner, the combination efficiency η_combine can be written as the following[134]:

$$\eta_\text{combine} = \frac{\int_{-\infty}^{\infty}\int_{-\infty}^{\infty} |\sum_{k=1}^{N_\text{T}} E_\text{k}(x,y,t)|^2 dxdydt}{N_\text{T}\int_{-\infty}^{\infty}\int_{-\infty}^{\infty} \sum_{k=1}^{N_\text{T}} |E_\text{k}(x,y,t)|^2 dxdydt} \tag{108}$$

where $E_\text{k}(x,y,t)$ is the terahertz electric field obtained from kth stage. The combination efficiency η_combine reaches the maximum when $E_1(x,y,t) = E_2(x,y,t) = ... = E_\text{N}(x,y,t)$, e.g terahertz outputs from each stage need to have identical spectrum, phase and amplitude[134]. This could be achieved by adjusting the length of each stage and the relative arrival time of the terahertz beams. With equation (108), the combination efficiency of the terahertz output beams are 93.0% (Fig. 51(e,f)) and 95.2% (Fig. 51(g,h)), respectively. This high combination efficiency is the result of similarity between terahertz beams generated in each stage. As a result, the final total efficiency η_{total} of a two stage system can be written in Eq. (109) where η_1, η_2 is the generation efficiency of the first and second stage respectively, $\eta_{\mathrm{a}}, \eta_{\mathrm{b}}$ is the out-coupling efficiency, from PPLN to the air with QC, of the first and second stage respectively and η_{combine} is the combination efficiency of the terahertz generated by the first and the second stage.

$$\eta_{\mathrm{total}} = \eta_{\mathrm{combine}} \times (\eta_1 \times \eta_{\mathrm{a}} + \eta_2 \times \eta_{\mathrm{b}}) \tag{109}$$

Using equation (109) and (99), a total terahertz energy 17.6 mJ with $\eta_{\mathrm{total}} = 1.6\%$ can be achieved with a two stage system using pump beams of size $\sigma = 5\,\mathrm{mm}$ and input pump energy 1.1 J.

7.12 Comparison with the experimental data

In this section, the numerical results are compared against the experimental results. Due to the collinear phase matching nature and the symmetry of the input pump pulse. The numerical results here is based on the 1D+1 (z,t) calculation.

In the experiment, the pump source is a home-built 2-lines system which is capable to deliver 250 ps pulses with 20 mJ energy at a repetition rate of 10 Hz. The 2-lines are made of one stable laser centered at 1030.365 nm and a commercial single-frequency laser tunable from 990 nm to 1080 nm (Toptica Inc.). They are combined, chopped and pre-amplified in an all-fiber structure front-end, and future boosted through a Regen amplifier together with a 4-pass amplifier. The duration of the flat-top pulse is adjustable from 250 ps to several ns in a step of 250 ps with an electro-optic modulator. In our experiment, the wavelength of the tunable laser was initially set around 1031.37 nm, so that the frequency difference between the two lines is 0.3 THz (400 μm poling period). Two periodically poled 5 mol.% MgO doped congruent z-cut periodically poled lithium niobate crystals (MgO:PPLN) with 9 mm and 40 mm length, respectively, were used. The crystals are not AR-coated and each has a cross section of 4x4 mm^2. To reduce the terahertz absorption, the PPLN is cryogenically cooled to 77 K during the experiment.

The chamber pressure level is lower than 10-6 mbar. The THz emission is collected via two 2-inch off-axis parabolic mirrors (OAP), one of which has a hole of 3-mm diameter to separate the infrared (IR) and THz beams. The generated terahertz pulse is detected by a pyroelectric Joulemeter (Gentec-EO, SDX-1152) with a polyethylene (PE) cover. A 8-mm thick Teflon plate was positioned in between the 2 OPA to stop the residual IR beam as well as the parasitic second harmonic generation. The IR beam going through the hole is partially sent to an optical spectrum analyzer to monitor the pump spectrum shaped by the DFG process.

It can be seen that at low input fluence with interaction length 10 mm (Fig. 52(a)), the simulation results matches very well with the experimental data. However for the 40 mm interaction length, the simulation results deviates with respect to the experimental data at high pump fluence (Fig. 52(b)). This saturation effect shown in the experimental data at high fluence can be caused by the ionization which is not included in the simulation.

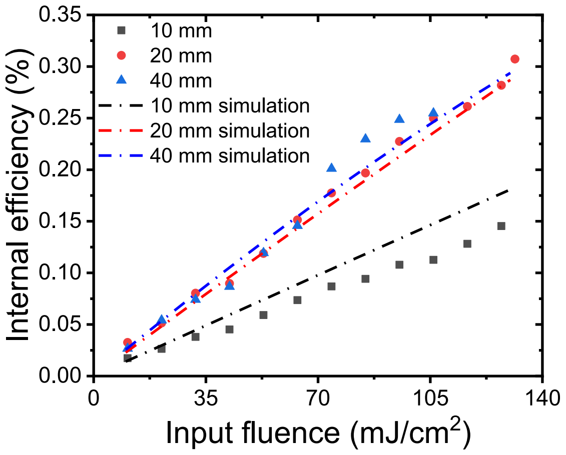

Figure 52: Experimental data from W. Tian et.al.[135]. The simulation results are compared against experimental data for 3 different PPLN lengthes.

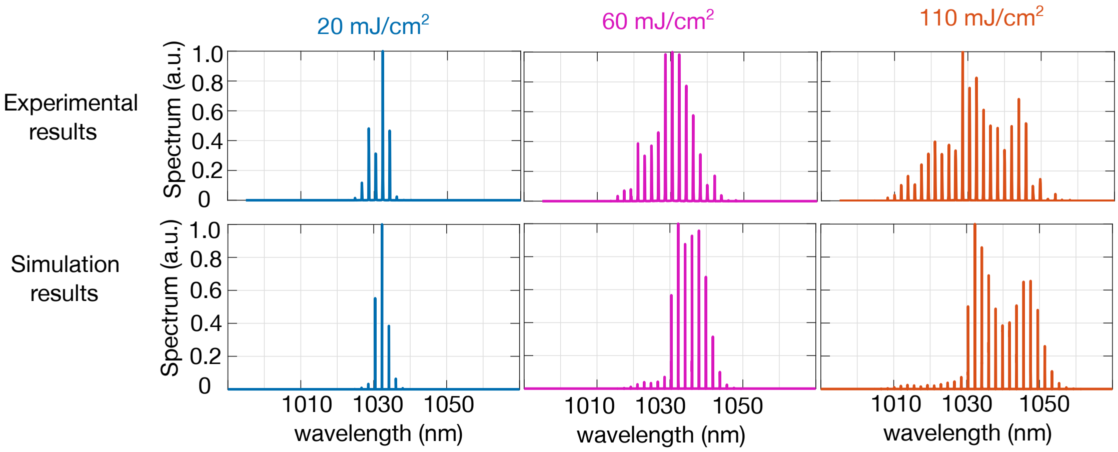

Figure 53: Comparison of the experimental data and simulation results for 3 different input pump fluence. Experimental data from W. Tian et.al.[135].

8 Chirp and Delay

Apart from the multi-cycle terahertz generating using the two-line configuration discussed in Section 7.8, another possibility is the chirp and delay configuration. The chirp and delay method is accomplished by mixing two linearly chirped (second order dispersion) optical pulses with a variable time delay and is first proposed by A. S. Weling[136]. Later on, the experiment is performed by F. Ahr and ∼ 0.1% conversion efficiency is achieved[103]. However, since the optical pump pulse is highly chirped, the terahertz generation process is extremely sensitive to the time delay. Additionally, higher order dispersions need to be avoided since they lead to nonlinear frequency distribution in time. However, in the experiment, it is challenging to completely eliminate the higher order dispersions. The work carried out by S. W. Jolly et. al. proposes a method of tuning the relative spectral phase of the pump pulses and reached the state-of-art terahertz energy of 0.6 mJ.

8.1 Delay Calculation

In this chapter, the author derive the analytical form of the phase matching time delay taking into account the second and third order dispersions. The comparisons of the simulation and the experimental data are presented. To begin with, if the second order dispersion is considered, one can write the input pump electric field as

$$E(\omega) = \exp[-\Delta\omega^2\tau^2/4]\exp[-i(\omega_0 t + \frac{\phi_2}{2}\Delta\omega^2)] \tag{110}$$

where $\Delta\omega = \omega - \omega_0$. By Fourier transform Eq. (110), one obtains Eq.(111).

$$\begin{aligned} E(t) &= \int_{-\infty}^{\infty} d\omega\ \exp[-\Delta\omega^2\tau^2/4]\exp[-i(\omega_0 t + \frac{\phi_2}{2}\Delta\omega^2)]\exp[i\omega t] \\ &= \int_{-\infty}^{\infty} d\Delta\omega\ \exp[i\Delta\omega t - (i\frac{\phi_2}{2} + \frac{\tau^2}{4})\Delta\omega^2] \\ &= \sqrt{\pi/(\tau^2/4 + i\phi_2/2)}\exp[-t^2\tau^2/(4\phi_2^2 + \tau^4)]\exp[it^2\phi_2/(2\phi_2^2 + \tau^4/2)] \end{aligned} \tag{111}$$

The last exponential term in Eq. (111) represents the time dependent phase. Since the derivative of the phase in time domain represents the instantaneous frequency, one can obtain Eq. (112).

$$\Delta\omega = t\phi_2/(\phi_2^2 + \tau^4/4) \tag{112}$$

It can be seen from Eq. (112) that the instantaneous frequency is linearly dependent on time (linear chirp). If $\phi_2 \gg \tau^2$, $\Delta\omega = t/\phi_2$. This means that with a given bandwidth, larger second order dispersion leads to smaller frequency separation in time, since the pulse duration is longer. If $\phi_2 = 0$, $\Delta\omega = 0$, Eq. (112) reduces to the transform limited case. If the third order dispersion is considered, one can write the electric field as the following

$$E(\omega) = \exp[-\Delta\omega^2\tau^2/4]\exp\left[-i(\omega_0 t + \frac{\phi_2}{2}\Delta\omega^2 + \frac{\phi_3}{6}\Delta\omega^3)\right]. \tag{113}$$

The corresponding electric field in time domain is

$$\begin{aligned} E(t) &= \int_{-\infty}^{\infty} d\omega\ \exp[-\Delta\omega^2\tau^2/4]\exp\left[-i(\omega_0 t + \frac{\phi_2}{2}\Delta\omega^2 + \frac{\phi_3}{6}\Delta\omega^3)\right]\exp[i\omega t] \\ &= \int_{-\infty}^{\infty} d\Delta\omega\ \exp[-\Delta\omega^2\tau^2/4]\exp\left[i(\Delta\omega t - \frac{\phi_2}{2}\Delta\omega^2 - \frac{\phi_3}{6}\Delta\omega^3)\right] \\ &= \int_{-\infty}^{\infty} d\Delta\omega\ \exp\left[i\Delta\omega t - i(\frac{\phi_2}{2} - i\frac{\tau^2}{4})\Delta\omega^2 - i\frac{\phi_3}{6}\Delta\omega^3\right] \end{aligned} \tag{114}$$

It is challenging to analytically solve the third order in Fourier transform. As a result, a special function need to be used. For a third degree polynomials $ax^3 + bx^2 + cx$, in order to remove the second order term bx^2, one can perform a variable substitution as $v = x + b/3a$. By setting $v = \Delta\omega + 2(\phi_2/2 - i\tau^2/4)/\phi_3$, Eq. (114), one can get[137]

$$\begin{aligned} E(t) \quad &= \exp\left\{-i\frac{(\phi_2/2 - i\tau^2/4)}{\phi_3/2}\left[t + \frac{2}{3}\frac{(\phi_2/2 - i\tau^2/4)^2}{\phi_3/2}\right]\right\} \\ &\times \int_{-\infty}^{\infty} dv\ \exp\left\{iv\left[t + \frac{(\phi_2/2 - i\tau^2/4)^2}{\phi_3/2}\right] - iv^3\frac{\phi_3}{6}\right\} \\ &= \exp\left\{-i\frac{(\phi_2/2 - i\tau^2/4)}{\phi_3/2}\left[t + \frac{2}{3}\frac{(\phi_2/2 - i\tau^2/4)^2}{\phi_3/2}\right]\right\}\mathrm{Ai}\,(z) \end{aligned} \tag{115}$$

where Ai(z) represents the Airy function and

$$z = -\left(\frac{2}{\phi_3}\right)^{\frac{1}{3}}\left[t + \frac{(\phi_2/2 - i\tau^2/4)^2}{\phi_3/2}\right].$$

In the general experiment, GDD $\sim 100 \times \mathrm{ps}^2$, TOD $\sim 1 \times \mathrm{ps}^3$ and $\tau \approx 1$ps. For terahertz generation, the $t \approx \Omega\phi_2$. As a result, $t/\phi_3^{1/3} \approx 1$ and $|\phi_2| \gg |\phi_3|^{2/3}$. These two conditions leads to $|z| \to \infty$. It is useful to approximate the Ariy function by the limit

$$\lim_{|z|\to\infty} \mathrm{Ai}(z) \approx (1/2\pi^{1/2}z^{1/4})\exp[-\frac{2}{3}z^{3/2}]$$

By setting $a = (\phi_2/2 - i\tau^2/4)^2/(\phi_3/2)$ one can further simplify Eq. (115) and obtain time dependent frequency in Eq. (116)

$$i\frac{d\,\mathrm{phase}}{dt} = -i\frac{(\phi_2/2 - i\tau^2/4)}{\phi_3/2} + \left(\frac{2}{\phi_3}\right)^{1/3} z^{1/2} = i\left[-\frac{(\phi_2/2 - i\tau^2/4)}{\phi_3/2} + \left(\frac{2}{\phi_3}\right)^{1/2} \sqrt{a}(1 + t/a)^{1/2}\right] \tag{116}$$

By performing the Taylor expansion, one can get

$$\begin{aligned} \frac{d\,\mathrm{phase}}{dt} \quad &= -\frac{(\phi_2/2 - i\tau^2/4)}{\phi_3/2} + \frac{\phi_2/2 - i\tau^2/4}{\phi_3/2}(1 + \frac{1}{2}t/a + \frac{1}{8}t^2/a^2) \\ &= \frac{t/2}{\phi_2/2 - i\tau^2/4} + \frac{t^2\phi_3}{16(\phi_2/2 - i\tau^2/4)^3} \end{aligned}$$

Consequently,

$$\omega - \omega_0 = \frac{t\phi_2}{\phi_2^2 + \tau^4/4} + \frac{t^2\phi_3(\phi_2^3/2 - 3\phi_2\tau^4/8)}{(\phi_2^2 + \tau^4/4)^3}$$

If $\phi_2 \gg \tau^2$, one can further simplify the question and obtain the following results

$$\omega - \omega_0 = \frac{t}{\phi_2} + \frac{t^2\phi_3}{2\phi_2^3}$$

In order to find the optimal delay t_0 with a given target terahertz frequency Ω, one can write the polarization term for the terahertz generation as

$$\begin{aligned}
P^{(2)}_{\mathrm{THz}} = \quad & \chi^{(2)}\frac{\Omega^2 E_0^2}{c^2}\int E(\omega+\Omega)E^*(\omega)\exp\left[i\Delta k(\Omega)z\right]d\omega \\
& = \chi^{(2)}\frac{\Omega^2}{c^2}\int \exp\left[\frac{-(\Delta\omega+\Omega)^2\tau^2}{4}\right]\exp\left[-i(\Delta\omega t_0 + \frac{\phi_2}{2}(\Delta\omega+\Omega)^2 + \frac{\phi_3}{6}(\Delta\omega+\Omega)^3)\right] \\
& \times\exp\left[\frac{-\Delta\omega^2\tau^2}{4}\right]\exp\left[-i(\frac{\phi_2}{2}\Delta\omega^2 + \frac{\phi_3}{6}\Delta\omega^3)\right]\exp\left[i\Delta k(\Omega)z\right]d\omega \\
& = \chi^{(2)}\frac{\Omega^2 E_0^2}{c^2}\int \exp\left[-\Delta\omega^2(\frac{\tau^2}{2} + i\frac{\Omega\phi_3}{2})\right]\exp\left[-\frac{\Delta\omega}{2}\left(\frac{\tau^2\Omega}{2} + i\frac{\Omega^2\phi_3}{2} + i\phi_2\Omega + it_0\right)\right] \\
& \times\exp\left[-\Omega^2\left(\frac{\tau^2}{4} + i\frac{\phi_2}{2}\right)\right]\exp\left[i\Delta k(\Omega)z\right]d\Delta\omega \\
& = \chi^{(2)}\frac{\Omega^2 E_0^2\sqrt{2\pi}}{c^2\sqrt{\tau^2 + i\Omega\phi_3}}\exp\left[-\frac{\Omega^2\tau^2}{8} - i\frac{\phi_3\Omega^3}{24} + \frac{i\Omega}{2}t_0 - \frac{(\phi_2\Omega + t_0)^2}{2\tau^2 + i2\Omega\phi_3}\right]\exp\left[i\Delta k(\Omega)z\right]
\end{aligned}$$

As a result, one can get Eq. (117) where L is the interaction length.

$$|E_{\mathrm{THz}}|^2 = \frac{(\chi^{(2)})^2\Omega^2 E_0^4 L^2\pi}{2c^2 n_t^2(\tau^2 + \Omega\phi_3)}\exp\left(\frac{-\Omega^2\tau^2}{4}\right)\exp\left[\frac{-\tau^2(\phi_2\Omega + t_0)^2}{\tau^4 + \Omega^2\phi_3^2}\right]\mathrm{sinc}\left[\frac{\Delta k(\Omega)}{2L}\right]^2. \tag{117}$$

Equation (117) suggests that in order to obtain the maximum generated terahertz field i.e. the phase matching delay, the condition $t_0 = -\Omega\phi_2$ has to be satisfied. Note that this condition is the same as when the ϕ_3 is not presented. Additionally, it can also be seen that with respect to the increase of the ϕ_3, the maximum efficiency reduces but the efficiency is less sensitive with respect to the delay (i.e. the phase matching range with respect to the delay increases). It can be understood in the following way. The ϕ_2 causes a linear instantaneous frequency distribution with respect to time (see Fig. 54). If the ϕ_3 is not present, there is only one specific time delay which satisfies the phase matching condition and at this time delay, the entire pulse in time contributes to the generation of the desired terahertz frequency. Given a different delay, the terahertz generated is centered at a different frequency and is filtered out by the phase matching bandwidth of the PPLN, causing a very sensitive relation of the efficiency with respect to the delay. However, if the ϕ_3 is present, the instantaneous frequency is not linear. Only a small section of the pulse in time can contribute to the targeted terahertz radiation. Regardless of the delay, since each part of the OP phase match different terahertz frequencies, there is always a few amount of the generated terahertz fields fall into the phase matching bandwidth, leading to a less sensitive efficiency change with respect to the delay.

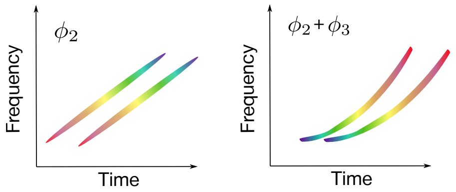

Figure 54: Illustration of the instantaneous frequency with respect to time with only the second order dispersion (ϕ_2 left) and with the second plus third order dispersion ($\phi_2 + \phi_3$ right).

The comparison of the simulation and the experimental data can be found in Fig. 55, where the simulation parameters are listed in Table 9. The experimental data in Fig. 55 are obtained from Halil Olgun. Due to the poor organization of him, the entire comparison between the experiment and the theory is not complete. In case of any discrepancy related to Fig. 55, please blame it on Halil Olgun.

Table 9: Simulation parameters with chirp&delay input

Parameters	**Values**
phase-matching frequency Ω_0	$2\pi \times 0.53$ THz
input energy	19 mJ
ϕ_2	-229.3 ps^2
Φ_3	5.26 ps^3

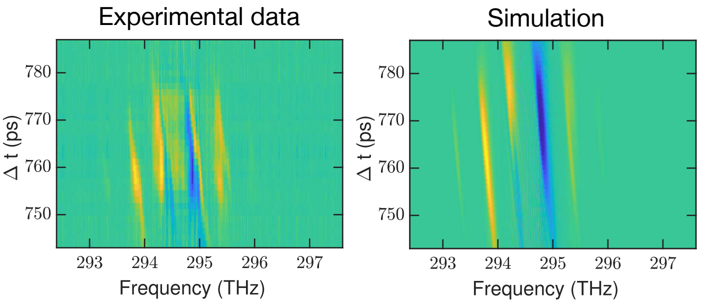

Figure 55: The scan of the output OP spectrum with respect to the relative delay (Δt) is presented. The optimal delay $t_0 = \phi_2 \times \Omega_0 = 770$ps and the relative delay $\Delta t = t - t_0$. The left and the right show the experimental data and the simulation respectively.

Part IV

Conclusion and future work

9 Conclusion

For few-cycle terahertz pulses, the spatial dependence of the terahertz electric field properties generated in a tilted-pulse-front setup are studies. By comparing the 1D+1, 2D+1 and 3D+1 numerical models, it is found that the 1D+1 calculation cannot capture certain key features of the terahertz generation process. Additionally, the 3D+1 calculation shows that within the OP beam size range $\sigma_y = [0.5, 4.5]$ mm, diffraction in the dimension perpendicular to the pulse-front-tilt plane does not have much influence on the terahertz generation process. For those cases, the 2D calculation (x-z coordinates) is a good approximation.

Perpendicular to the pulse front tilt plane, in y-direction, the terahertz beam waist relates to the OP waist with $\sigma_y/\sqrt{2}$, which is as expected for the second order nonlinear process. However, in the x dimension, the OP beam size does not have a large impact on the generated terahertz beam size. The terahertz pulses are generated close to the apex of the crystal and the single-cycle region is located close to the vicinity of the crystal apex. Thereby, large OP beam sizes lead to a reduced percentage of single-cycle content of the generated terahertz pulses. Attention must be paid to the fact that the terahertz generated farther from the apex of the crystal, which can possess a significant fraction of the total generated terahertz energy, suffers from poor electric field quality and temporal chirp.

In order to maximize the single-cycle content, the OP beam size along the x dimension should be kept reasonably small, while the size along the y dimension can be used to enlarge the pump beam if necessary. Another option is to reduce the OP input fluence. These findings are of particular relevance to carrier-envelope-phase sensitive terahertz applications and strong filed terahertz physics.

Different TPF schemes are presented and analyzed. With lower OP input intensity, two effects are found. One is that the terahertz electric field shows more single-cycle property along the x dimension. The other is that the generated terahertz beam size increases. These two effects lead to less out-coupling loss. For small OP beam size ($\sigma'_x = 0.5$ mm), the output terahertz beamsize decreases with increasing initial angular dispersion, i.e. STC > RES > CG.

Schemes CG, NLES and RES, are applicable for a large parameter ranges such as OP energy, bandwidth and beam size. Within these three schemes, the CG favors smaller interaction length, narrower bandwidth and smaller beam size due to the large angular dispersion. NLES has a potential of delivering large and homogeneous terahertz beam size because of the plan-parallel shape of the LN crystal and the smaller imaging errors in comparison of the CG scheme. Additionally, the generated terahertz spectrum is also not related to the OP beam size. However, once the structure is produced, the interaction length is fixed, making this scheme less flexible.

In the CG scheme, the entire pulse-front-tile forms a smooth and continuous surface, which perfectly full-fill the PM condition, whereas the situation for the schemes related to beamlets (NLES, RES and MSPM), is different. Since m can only be integers, the entire trend (envelope) of the beamlets satisfies the PM condition while each individual beamlet itself has an offset with respect to the perfect pulse-front-tilt surface.

Due to the zero initial angular dispersion, this scheme could generated spatially homogeneous few-cycle terahertz pulse with highest conversion efficiency. However, the OP pulse has to be broadband. Due to the spatial chirp, the bandwidth scales linearly with the OP beam size, making this scheme not applicable for large OP beam sizes.

The MSPM scheme delivers the lowest efficiency . For large OP beam size, the efficiency is comparable to RES scheme. We do not recommend MSPM scheme for small OP beam size.

For multi-cycle terahertz generation, a scheme using a consecutive arrangement of PPLN crystals (multi-stage system) is presented. For this purpose, a 2-D numerical scheme assuming cylindrical symmetry is developed. The simulation includes the effects of DFG, SPM, self-focusing, beam diffraction, dispersion and terahertz absorption.

For a single stage, the optimal pump beam pulse duration for a 2-line pump spectrum configuration is 150 ps with effective length 25 mm and conversion efficiency η = 1.05%. With this pump pulse configuration, the terahertz spatial profile resembles the pump when the pump waist $\sigma \geq 3$ mm. Additionally, it is found that the intensity profile modulation has negligible influence on the terahertz generation efficiency, whereas a distortion in phase front strongly reduces the conversion efficiency. This suggests that care must be taken in circumventing phase induced efficiency deterioration for high energy terahertz generation.

For a multi-stage system, it is found that by recycling the pump pulse with dispersion compensation, the efficiency can be greatly enhanced. Subsequently, a quartz output coupler for separating the terahertz beam and optical pump with high terahertz transmission is designed.

Specifically, for a two stage system, the generation of a terahertz pulse of 17.6 mJ energy with total conversion efficiency η_{total} = 1.6% at 0.3 THz for a 1.1 J input pump energy, is predicted. The generation efficiencies are $\eta_1 = 1.0\%, \eta_2 = 0.8\%$, the out-coupling efficiencies are $\eta_a = 96.1\%, \eta_b = 93.7\%$ and combination efficiency is $\eta_{\text{combine}} = 93.0\%$.

10 Future work

The two numerical packages for few-cycle and multi-cycle terahertz generations can be updated and modified in future work. Other nonlinear materials can be easily investigated and implemented by changing material property functions. The damage and ionization effects are not included at the current stage of work. Terahertz generation with OP at 2 μm or even 10 μm can be another interesting field to explore due to the higher quantum efficiency at the longer wavelength. Higher-order nonlinear effects such as self-phase-modulation and high-harmonic-generation at the terahertz frequency range could also be investigated.

11 Beautiful mistake

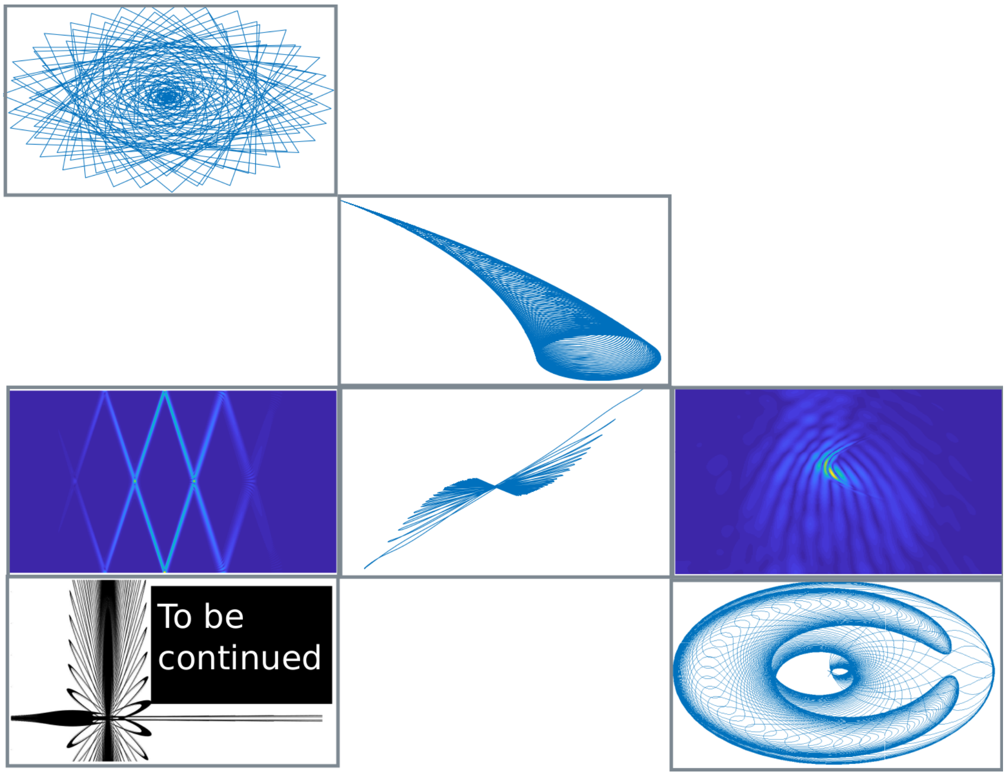

This is a small exhibition of the beautiful pictures that I created by accident over the years. Funny enough that this level of beauty only appears when I have numerical errors in my code. The correct calculations never succeed in impressing me by the form of the output. This is where the section title "beautiful mistake" comes from. These lovely pictures are surprises during my research. Though "incorrect" scientifically speaking, I still couldn't have the heart to throw them away. If someday, you see similar pictures somewhere else, don't be too shocked. It might be just me, failing to make my path to become a professor and consequently decide to venture to art-related fields (kidding! I certainly will be a PROFESSOR!). If you have reached this section, that means more or less you have read through my thesis (I hope?). I do hope that you enjoy the explorations in physics as much as I do. In the world full of unsolved equations and puzzles, the satisfactory of knowing a little bit more serves as the torchlight through my journey with physics. I curiously walk through this journey with all my love and passion.

References

[1] A. Svetlitza, M. Slavenko, T. Blank, I. Brouk, S. Stolyarova, and Y. Nemirovsky, "Thz measurements and calibration based on a blackbody source," *IEEE Transactions on Terahertz Science and Technology*, vol. 4, no. 3, pp. 347–359, 2014.

[2] A. Rostami, H. Rasooli, and H. Baghban, *Terahertz technology: fundamentals and applications*. Springer Science & Business Media, 2010, vol. 77.

[3] M. Lang and A. Deninger, "Laser-based terahertz generation & applications," 2012, company: Toptica Photonics AG, Gräfelfing, Germany accessed: 18.11.2019. [Online]. Available: https://www.toptica.com/fileadmin/Editors_English/12_literature/03_terahertz/toptica_laser-based_terahertz_generation_and_applications.pdf

[4] J. Federici and L. Moeller, "Review of terahertz and subterahertz wireless communications," *Journal of Applied Physics*, vol. 107, no. 11, p. 6, 2010.

[5] A. Davies, E. H. Linfield, and M. B. Johnston, "The development of terahertz sources and their applications," *Physics in Medicine & Biology*, vol. 47, no. 21, p. 3679, 2002.

[6] T. Kampfrath, A. Sell, G. Klatt, A. Pashkin, S. Mährlein, T. Dekorsy, M. Wolf, M. Fiebig, A. Leitenstorfer, and R. Huber, "Coherent terahertz control of antiferromagnetic spin waves," *Nature Photonics*, vol. 5, no. 1, pp. 31–34, 2011.

[7] O. Schubert, M. Hohenleutner, F. Langer, B. Urbanek, C. Lange, U. Huttner, D. Golde, T. Meier, M. Kira, S. W. Koch *et al.*, "Sub-cycle control of terahertz high-harmonic generation by dynamical bloch oscillations," *Nature Photonics*, vol. 8, no. 2, p. 119, 2014.

[8] D. Zhang, A. Fallahi, M. Hemmer, X. Wu, M. Fakhari, Y. Hua, H. Cankaya, A.-L. Calendron, L. E. Zapata, N. H. Matlis *et al.*, "Segmented terahertz electron accelerator and manipulator (steam)," *Nature photonics*, p. 1, 2018.

[9] H. Bakker, S. Hunsche, and H. Kurz, "Observation of thz phonon-polariton beats in LiTaO3," *Physical review letters*, vol. 69, no. 19, p. 2823, 1992.

[10] A. Markelz, A. Roitberg, and E. J. Heilweil, "Pulsed terahertz spectroscopy of dna, bovine serum albumin and collagen between 0.1 and 2.0 thz," *Chemical Physics Letters*, vol. 320, no. 1, pp. 42–48, 2000.

[11] M. Nagel, P. Haring Bolivar, M. Brucherseifer, H. Kurz, A. Bosserhoff, and R. Büttner, "Integrated thz technology for label-free genetic diagnostics," *Applied Physics Letters*, vol. 80, no. 1, pp. 154–156, 2002.

[12] K. Young, Q. Wen, S. Hanany, H. Imada, J. Koch, T. Matsumura, O. Suttmann, and V. Schütz, "Broadband millimeter-wave anti-reflection coatings on silicon using pyramidal sub-wavelength structures," *J. Appl. Phys*, vol. 121, no. 21, p. 213103, 2017.

[13] M. Teich, M. Wagner, H. Schneider, and M. Helm, "Semiconductor quantum well excitons in strong, narrowband terahertz fields," *New Journal of Physics*, vol. 15, no. 6, p. 065007, 2013.

[14] E. A. Nanni, W. R. Huang, K.-H. Hong, K. Ravi, A. Fallahi, G. Moriena, R. D. Miller, and F. X. Kärtner, "Terahertz-driven linear electron acceleration," *Nature communications*, vol. 6, p. 8486, 2015.

[15] L. J. Wong, A. Fallahi, and F. X. Kärtner, "Compact electron acceleration and bunch compression in thz waveguides," *Optics express*, vol. 21, no. 8, pp. 9792–9806, 2013.

[16] P. Tan, J. Huang, K. Liu, Y. Xiong, and M. Fan, "Terahertz radiation sources based on free electron lasers and their applications," *Science China Information Sciences*, vol. 55, no. 1, pp. 1–15, 2012.

[17] M. Y. Glyavin, A. G. Luchinin, and G. Y. Golubiatnikov, "Generation of 1.5-kw, 1-thz coherent radiation from a gyrotron with a pulsed magnetic field," *Physical review letters*, vol. 100, no. 1, p. 015101, 2008.

[18] V. Bratman, Y. K. Kalynov, and V. Manuilov, "Large-orbit gyrotron operation in the terahertz frequency range," *Physical review letters*, vol. 102, no. 24, p. 245101, 2009.

[19] V. Bratman, A. Bogdashov, G. Denisov, M. Y. Glyavin, Y. K. Kalynov, A. Luchinin, V. Manuilov, V. Zapevalov, N. Zavolsky, and V. Zorin, "Gyrotron

development for high power thz technologies at iap ras," *Journal of Infrared, Millimeter, and Terahertz Waves*, vol. 33, no. 7, pp. 715–723, 2012.

[20] K. Vijayraghavan, Y. Jiang, M. Jang, A. Jiang, K. Choutagunta, A. Vizbaras, F. Demmerle, G. Boehm, M. C. Amann, and M. A. Belkin, "Broadly tunable terahertz generation in mid-infrared quantum cascade lasers," *Nat. Commun*, vol. 4, p. 2021, 2013.

[21] B. S. Williams, "Terahertz quantum-cascade lasers," *Nature photonics*, vol. 1, no. 9, pp. 517–525, 2007.

[22] M. A. Belkin, F. Capasso, A. Belyanin, D. L. Sivco, A. Y. Cho, D. C. Oakley, C. J. Vineis, and G. W. Turner, "Terahertz quantum-cascade-laser source based on intracavity difference-frequency generation," *Nature Photonics*, vol. 1, no. 5, pp. 288–292, 2007.

[23] Y.-S. Lee, *Principles of terahertz science and technology*. Springer Science & Business Media, 2009, vol. 170.

[24] K. L. Vodopyanov, "Optical generation of narrow-band terahertz packets in periodically-inverted electro-optic crystals: conversion efficiency and optimal laser pulse format," *Optics Express*, vol. 14, no. 6, pp. 2263–2276, 2006.

[25] Z. Chen, X. Zhou, C. A. Werley, and K. A. Nelson, "Generation of high power tunable multicycle teraherz pulses," *Appl. Phys. Lett*, vol. 99, no. 7, p. 071102, 2011.

[26] M. Tonouchi, "Cutting-edge terahertz technology," *Nat. Photonics*, vol. 1, no. 2, p. 97, 2007.

[27] H. Gebbie, N. Stone, and F. Findlay, "A stimulated emission source at 0.34 millimetre wave-length," *Nature*, vol. 202, no. 4933, p. 685, 1964.

[28] A. Crocker, "Stimulated emission in the far infra-red," 1964.

[29] E. Budiarto, J. Margolies, S. Jeong, J. Son, and J. Bokor, "High-intensity terahertz pulses at 1-khz repetition rate," *IEEE Journal of Quantum Electronics*, vol. 32, no. 10, pp. 1839–1846, 1996.

[30] D. You, R. Jones, P. Bucksbaum, and D. Dykaar, “Generation of high-power sub-single-cycle 500-fs electromagnetic pulses,” *Optics letters*, vol. 18, no. 4, pp. 290–292, 1993.

[31] P. C. Upadhya, W. Fan, A. Burnett, J. Cunningham, A. G. Davies, E. H. Linfield, J. Lloyd-Hughes, E. Castro-Camus, M. B. Johnston, and H. Beere, “Excitation-density-dependent generation of broadband terahertz radiation in an asymmetrically excited photoconductive antenna,” *Optics letters*, vol. 32, no. 16, pp. 2297–2299, 2007.

[32] N. M. Burford and M. O. El-Shenawee, “Review of terahertz photoconductive antenna technology,” *Optical Engineering*, vol. 56, no. 1, p. 010901, 2017.

[33] H. Hamster, A. Sullivan, S. Gordon, W. White, and R. Falcone, “Subpicosecond, electromagnetic pulses from intense laser-plasma interaction,” *Physical review letters*, vol. 71, no. 17, p. 2725, 1993.

[34] X. Xie, J. Dai, and X.-C. Zhang, “Coherent control of thz wave generation in ambient air,” *Physical Review Letters*, vol. 96, no. 7, p. 075005, 2006.

[35] Y. Minami, T. Kurihara, K. Yamaguchi, M. Nakajima, and T. Suemoto, “High-power thz wave generation in plasma induced by polarization adjusted two-color laser pulses,” *Applied Physics Letters*, vol. 102, no. 4, p. 041105, 2013.

[36] Y. S. You, T. I. Oh, and K.-Y. Kim, “Mechanism of elliptically polarized terahertz generation in two-color laser filamentation,” *Optics letters*, vol. 38, no. 7, pp. 1034–1036, 2013.

[37] V. Andreeva, O. Kosareva, N. Panov, D. Shipilo, P. Solyankin, M. Esaulkov, P. G. de Alaiza Martínez, A. Shkurinov, V. Makarov, L. Bergé *et al.*, “Ultrabroad terahertz spectrum generation from an air-based filament plasma,” *Physical review letters*, vol. 116, no. 6, p. 063902, 2016.

[38] T. Idehara and S. P. Sabchevski, “Gyrotrons for high-power terahertz science and technology at fir uf,” *Journal of Infrared, Millimeter, and Terahertz Waves*, vol. 38, no. 1, pp. 62–86, 2017.

[39] D. Auston, K. Cheung, and P. Smith, “Picosecond photoconducting hertzian dipoles,” *Applied physics letters*, vol. 45, no. 3, pp. 284–286, 1984.

[40] D. Dufour, L. Marchese, M. Terroux, H. Oulachgar, F. Généreux, M. Doucet, L. Mercier, B. Tremblay, C. Alain, P. Beaupré *et al.*, "Review of terahertz technology development at ino," *Journal of Infrared, Millimeter, and Terahertz Waves*, vol. 36, no. 10, pp. 922–946, 2015.

[41] F. Kärtner, F. Ahr, A.-L. Calendron, H. Çankaya, S. Carbajo, G. Chang, G. Cirmi, K. Dörner, U. Dorda, A. Fallahi *et al.*, "Axsis: Exploring the frontiers in attosecond x-ray science, imaging and spectroscopy," *Nuclear Instruments and Methods in Physics Research Section A: Accelerators, Spectrometers, Detectors and Associated Equipment*, vol. 829, pp. 24–29, 2016.

[42] R. Hellwarth, "Third-order optical susceptibilities of liquids and solids," *Progress in Quantum Electronics*, vol. 5, pp. 1–68, 1977.

[43] P. N. Butcher, *Nonlinear Optical Phenomena*. Ohio State University, 1965.

[44] C. Garrett, "Nonlinear optics, anharmonic oscillators, and pyroelectricity," *IEEE Journal of Quantum Electronics*, vol. 4, no. 3, pp. 70–84, 1968.

[45] D. H. Auston and M. C. Nuss, "Electrooptical generation and detection of femtosecond electrical transients," *IEEE Journal of quantum electronics*, vol. 24, no. 2, pp. 184–197, 1988.

[46] J. AS BARKER and R. Loudon, "Response functions in the theory of raman scattering by vibrational and polariton modes in dielectric crystals," *Reviews of Modern Physics*, vol. 44, no. 1, p. 18, 1972.

[47] R. W. Boyd, *Nonlinear optics*. Academic press, 2003.

[48] M. Schall, H. Helm, and S. Keiding, "Far infrared properties of electro-optic crystals measured by thz time-domain spectroscopy," *International journal of infrared and millimeter waves*, vol. 20, no. 4, pp. 595–604, 1999.

[49] S. S. Sussman, "Tunable light scattering from transverse optical modes in lithium niobate," STANFORD UNIV CA MICROWAVE LAB, Tech. Rep., 1970.

[50] A. Barker Jr and R. Loudon, "Dielectric properties and optical phonons in linb o 3," *Physical Review*, vol. 158, no. 2, p. 433, 1967.

[51] M. Unferdorben, Z. Szaller, I. Hajdara, J. Hebling, and L. Pálfalvi, “Measurement of refractive index and absorption coefficient of congruent and stoichiometric lithium niobate in the terahertz range,” *Journal of Infrared, Millimeter, and Terahertz Waves*, vol. 36, no. 12, pp. 1203–1209, 2015.

[52] I. Shoji, T. Kondo, A. Kitamoto, M. Shirane, and R. Ito, “Absolute scale of second-order nonlinear-optical coefficients,” *JOSA B*, vol. 14, no. 9, pp. 2268–2294, 1997.

[53] K. J. Blow and D. Wood, “Theoretical description of transient stimulated raman scattering in optical fibers,” *IEEE Journal of Quantum Electronics*, vol. 25, no. 12, pp. 2665–2673, 1989.

[54] G. P. Agrawal, “Nonlinear fiber optics: its history and recent progress,” *Journal of the Optical Society of America B*, vol. 28, no. 12, pp. A1–A10, 2011.

[55] O. E. Martinez, “Pulse distortions in tilted pulse schemes for ultrashort pulses,” *Optics communications*, vol. 59, no. 3, pp. 229–232, 1986.

[56] ——, “Grating and prism compressors in the case of finite beam size,” *JOSA B*, vol. 3, no. 7, pp. 929–934, 1986.

[57] L. Wang, T. Kroh, N. H. Matlis, and F. X. Kärtner, “Full 3d+1 modelling of tilted-pulse-front setups for single-cycle terahertz generation,” *Journal of the Optical Society of America B*, vol. 37, no. 3, 2020. [Online]. Available: https://doi.org/10.1364/JOSAB.379142

[58] M. Hemmer, G. Cirmi, K. Ravi, F. Reichert, F. Ahr, L. Zapata, O. Mücke, A.-L. Calendron, H. Çankaya, D. Schimpf *et al.*, “Cascaded interactions mediated by terahertz radiation,” *Optics express*, vol. 26, no. 10, pp. 12 536–12 546, 2018.

[59] J. Hebling, G. Almasi, I. Z. Kozma, and J. Kuhl, “Velocity matching by pulse front tilting for large-area thz-pulse generation,” *Optics Express*, vol. 10, no. 21, pp. 1161–1166, 2002.

[60] J. A. Fülöp, Z. Ollmann, C. Lombosi, C. Skrobol, S. Klingebiel, L. Pálfalvi, F. Krausz, S. Karsch, and J. Hebling, “Efficient generation of thz pulses with 0.4 mj energy,” *Optics express*, vol. 22, no. 17, pp. 20 155–20 163, 2014.

[61] L. Tokodi, J. Hebling, and L. Pálfalvi, "Optimization of the tilted-pulse-front terahertz excitation setup containing telescope," *Journal of Infrared, Millimeter, and Terahertz Waves*, vol. 38, no. 1, pp. 22–32, 2017.

[62] J. Fülöp, L. Pálfalvi, G. Almási, and J. Hebling, "Design of high-energy terahertz sources based on optical rectification," *Optics express*, vol. 18, no. 12, pp. 12 311–12 327, 2010.

[63] O. E. Martinez, "Matrix formalism for pulse compressors," *IEEE journal of quantum electronics*, vol. 24, no. 12, pp. 2530–2536, 1988.

[64] K. Ravi and F. Kärtner, "Analysis of terahertz generation using tilted pulse fronts," *Optics express*, vol. 27, no. 3, pp. 3496–3517, 2019.

[65] K. Ravi, D. N. Schimpf, and F. X. Kärtner, "Pulse sequences for efficient multi-cycle terahertz generation in periodically poled lithium niobate," *Optics express*, vol. 24, no. 22, pp. 25 582–25 607, 2016.

[66] J. Fülöp, L. Pálfalvi, S. Klingebiel, G. Almási, F. Krausz, S. Karsch, and J. Hebling, "Generation of sub-mj terahertz pulses by optical rectification," *Optics letters*, vol. 37, no. 4, pp. 557–559, 2012.

[67] C. Lombosi, G. Polónyi, M. Mechler, Z. Ollmann, J. Hebling, and J. Fülöp, "Nonlinear distortion of intense thz beams," *New Journal of Physics*, vol. 17, no. 8, p. 083041, 2015.

[68] L. Pálfalvi, G. Tóth, L. Tokodi, Z. Márton, J. A. Fülöp, G. Almási, and J. Hebling, "Numerical investigation of a scalable setup for efficient terahertz generation using a segmented tilted-pulse-front excitation," *Optics express*, vol. 25, no. 24, pp. 29 560–29 573, 2017.

[69] L. Wang, G. Tóth, J. Hebling, and F. Kärtner, "Tilted-pulse-front schemes for terahertz generation," *arXiv preprint arXiv:2001.09291*, 2020.

[70] J. Hebling, "Derivation of the pulse front tilt caused by angular dispersion," *Optical and Quantum Electronics*, vol. 28, no. 12, pp. 1759–1763, 1996.

[71] S. Akturk, X. Gu, E. Zeek, and R. Trebino, "Pulse-front tilt caused by spatial and temporal chirp," *Optics express*, vol. 12, no. 19, pp. 4399–4410, 2004.

[72] B. K. Ofori-Okai, P. Sivarajah, W. R. Huang, and K. A. Nelson, “THz generation using a reflective stair-step echelon,” *Opt. Express*, vol. 24, no. 5, pp. 5057–5068, 2016.

[73] Y. Avetisyan, A. Makaryan, V. Tadevosyan, and M. Tonouchi, “Design of a multistep phase mask for high-energy terahertz pulse generation by optical rectification,” *Journal of Infrared, Millimeter, and Terahertz Waves*, vol. 38, no. 12, pp. 1439–1447, 2017.

[74] P. S. Nugraha, G. Krizsán, C. Lombosi, L. Pálfalvi, G. Tóth, G. Almási, J. A. Fülöp, and J. Hebling, “Demonstration of a tilted-pulse-front pumped plane-parallel slab terahertz source,” *Optics letters*, vol. 44, no. 4, pp. 1023–1026, 2019.

[75] M. Bakunov, S. Bodrov, and M. Tsarev, “Terahertz emission from a laser pulse with tilted front: Phase-matching versus cherenkov effect,” *Journal of Applied Physics*, vol. 104, no. 7, p. 073105, 2008.

[76] M. I. Bakunov, S. B. Bodrov, and E. A. Mashkovich, “Terahertz generation with tilted-front laser pulses: dynamic theory for low-absorbing crystals,” *JOSA B*, vol. 28, no. 7, pp. 1724–1734, 2011.

[77] K. Ravi, W. R. Huang, S. Carbajo, E. A. Nanni, D. N. Schimpf, E. P. Ippen, and F. X. Kärtner, “Theory of terahertz generation by optical rectification using tilted-pulse-fronts,” *Optics express*, vol. 23, no. 4, pp. 5253–5276, 2015.

[78] M. Feit and J. Fleck, “Light propagation in graded-index optical fibers,” *Applied optics*, vol. 17, no. 24, pp. 3990–3998, 1978.

[79] M.-H. Wu, Y.-C. Chiu, T.-D. Wang, G. Zhao, A. Zukauskas, F. Laurell, and Y.-C. Huang, “Terahertz parametric generation and amplification from potassium titanyl phosphate in comparison with lithium niobate and lithium tantalate,” *Optics express*, vol. 24, no. 23, pp. 25 964–25 973, 2016.

[80] J. Huang, Z. Huang, N. Nikolaev, A. Mamrashev, V. Antsygin, O. Potaturkin, A. Meshalkin, A. Kaplun, G. Lanskii, Y. M. Andreev *et al.*, “Phase matching in rt ktp crystal for down-conversion into the thz range,” *Laser Physics Letters*, vol. 15, no. 7, p. 075401, 2018.

[81] K. Kato and E. Takaoka, “Sellmeier and thermo-optic dispersion formulas for ktp,” *Applied optics*, vol. 41, no. 24, pp. 5040–5044, 2002.

[82] J. D. Bierlein and H. Vanherzeele, “Potassium titanyl phosphate: properties and new applications,” *JOSA B*, vol. 6, no. 4, pp. 622–633, 1989.

[83] R. Adair, L. Chase, and S. A. Payne, “Nonlinear refractive index of optical crystals,” *Physical Review B*, vol. 39, no. 5, p. 3337, 1989.

[84] F. Yang, L. Huang, X. Zhao, L. Huang, D. Gao, J. Bi, X. Wang, and G. Zou, “An energy band engineering design to enlarge the band gap of ktiopo 4 (ktp)-type sulfates via aliovalent substitution,” *Journal of Materials Chemistry C*, vol. 7, no. 26, pp. 8131–8138, 2019.

[85] L. Wang, A. Fallahi, K. Ravi, and F. Kärtner, “High efficiency terahertz generation in a multi-stage system,” *Optics express*, vol. 26, no. 23, pp. 29 744–29 768, 2018.

[86] T. Kubacka, J. Johnson, M. Hoffmann, C. Vicario, S. De Jong, P. Beaud, S. Grübel, S.-W. Huang, L. Huber, L. Patthey *et al.*, “Large-amplitude spin dynamics driven by a thz pulse in resonance with an electromagnon,” *Science*, p. 1242862, 2014.

[87] M. Kress, T. Löffler, S. Eden, M. Thomson, and H. G. Roskos, “Terahertz-pulse generation by photoionization of air with laser pulses composed of both fundamental and second-harmonic waves,” *Optics Letters*, vol. 29, no. 10, pp. 1120–1122, 2004.

[88] P. U. Jepsen, R. H. Jacobsen, and S. Keiding, “Generation and detection of terahertz pulses from biased semiconductor antennas,” *JOSA B*, vol. 13, no. 11, pp. 2424–2436, 1996.

[89] A. Dreyhaupt, S. Winnerl, T. Dekorsy, and M. Helm, “High-intensity terahertz radiation from a microstructured large-area photoconductor,” *Applied Physics Letters*, vol. 86, no. 12, p. 121114, 2005.

[90] K. Ravi, B. Ofori-Okai, P. Sivarajah, W. Huang, F. Kaertner, and K. Nelson, “Broadband terahertz generation with a stair-step echelon,” in *CLEO: Science and Innovations*. Optical Society of America, 2017, pp. STu3J–1.

[91] C. P. Hauri, "Intense laser-based THz sources for XFEL experiments," in *Lasers and Electro-Optics (CLEO), 2017 Conference on*. IEEE, 2017, pp. 1–2.

[92] FLASH, "Flash parameters 2017." 2017, [Online; accessed 18-04-2018]. [Online]. Available: https://flash.desy.de/

[93] Z. Wu, A. S. Fisher, M. C. Hoffmann, S. Bonetti, D. Higley, and H. Durr, "THz light source at slac facet user facility," in *Infrared, Millimeter, and Terahertz waves (IRMMW-THz), 2014 39th International Conference on*. IEEE, 2014, pp. 1–2.

[94] K. Vodopyanov, M. Fejer, X. Yu, J. Harris, Y.-S. Lee, W. C. Hurlbut, V. Kozlov, D. Bliss, and C. Lynch, "Terahertz-wave generation in quasi-phase-matched gaas," *Appl. Phys. Lett*, vol. 89, no. 14, p. 141119, 2006.

[95] A. Rice, Y. Jin, X. Ma, X.-C. Zhang, D. Bliss, J. Larkin, and M. Alexander, "Terahertz optical rectification from< 110> zinc-blende crystals," *Appl. Phys. Lett*, vol. 64, no. 11, pp. 1324–1326, 1994.

[96] K. L. Vodopyanov, "Optical THz-wave generation with periodically-inverted gaas," *Laser & Photonics Reviews*, vol. 2, no. 1-2, pp. 11–25, 2008.

[97] J. Lu, H. Y. Hwang, X. Li, S.-H. Lee, O.-P. Kwon, and K. A. Nelson, "Tunable multi-cycle THz generation in organic crystal hmq-tms," *Opt. Express*, vol. 23, no. 17, pp. 22 723–22 729, 2015.

[98] Y.-S. Lee, T. Meade, V. Perlin, H. Winful, T. Norris, and A. Galvanauskas, "Generation of narrow-band terahertz radiation via optical rectification of femtosecond pulses in periodically poled lithium niobate," *Appl. Phys. Lett*, vol. 76, no. 18, pp. 2505–2507, 2000.

[99] D. Dietze, K. Unterrainer, and J. Darmo, "Dynamically phase-matched terahertz generation," *Opt. Lett.*, vol. 37, no. 6, pp. 1047–1049, 2012.

[100] K. Kawase, T. Hatanaka, H. Takahashi, K. Nakamura, T. Taniuchi, and H. Ito, "Tunable terahertz-wave generation from dast crystal by dual signal-wave parametric oscillation of periodically poled lithium niobate," *Opt. Lett.*, vol. 25, no. 23, pp. 1714–1716, 2000.

[101] A. Schneider, M. Neis, M. Stillhart, B. Ruiz, R. U. Khan, and P. Günter, “Generation of terahertz pulses through optical rectification in organic dast crystals: theory and experiment,” *JOSA B*, vol. 23, no. 9, pp. 1822–1835, 2006.

[102] G. Cirmi, M. Hemmer, K. Ravi, F. Reichert, L. E. Zapata, A.-L. Calendron, H. Çankaya, F. Ahr, O. D. Mücke, N. H. Matlis, and F. X. Kärtner, “Cascaded second-order processes for the efficient generation of narrowband terahertz radiation,” *J. Phys. B*, vol. 50, no. 4, p. 044002, 2017.

[103] F. Ahr, S. W. Jolly, N. H. Matlis, S. Carbajo, T. Kroh, K. Ravi, D. N. Schimpf, J. Schulte, H. Ishizuki, T. Taira *et al.*, “Narrowband terahertz generation with chirped-and-delayed laser pulses in periodically poled lithium niobate,” *Optics letters*, vol. 42, no. 11, pp. 2118–2121, 2017.

[104] S. W. Jolly, N. H. Matlis, F. Ahr, V. Leroux, T. Eichner, A.-L. Calendron, H. Ishizuki, T. Taira, F. X. Kärtner, and A. R. Maier, “Spectral phase control of interfering chirped pulses for high-energy narrowband terahertz generation,” *Nature communications*, vol. 10, no. 1, p. 2591, 2019.

[105] J. Manley and H. Rowe, “Some general properties of nonlinear elements-part i. general energy relations,” *Proceedings of the IRE*, vol. 44, no. 7, pp. 904–913, 1956.

[106] M. Cronin-Golomb, “Cascaded nonlinear difference-frequency generation of enhanced terahertz wave production,” *Opt. Lett.*, vol. 29, no. 17, pp. 2046–2048, 2004.

[107] M. C. Hoffmann, K.-L. Yeh, J. Hebling, and K. A. Nelson, “Efficient terahertz generation by optical rectification at 1035 nm,” *Opt. Express*, vol. 15, no. 18, pp. 11 706–11 713, 2007.

[108] J.-i. Shikata, M. Sato, T. Taniuchi, H. Ito, and K. Kawase, “Enhancement of terahertz-wave output from $LiNbO_3$ optical parametric oscillators by cryogenic cooling,” *Opt. Lett.*, vol. 24, no. 4, pp. 202–204, 1999.

[109] S.-W. Huang, E. Granados, W. R. Huang, K.-H. Hong, L. E. Zapata, and F. X. Kärtner, “High conversion efficiency, high energy terahertz pulses by optical rectification in cryogenically cooled lithium niobate,” *Opt. Lett.*, vol. 38, no. 5, pp. 796–798, 2013.

[110] Y.-S. Lee, T. Meade, M. DeCamp, T. Norris, and A. Galvanauskas, "Temperature dependence of narrow-band terahertz generation from periodically poled lithium niobate," *Appl. Phys. Lett*, vol. 77, no. 9, pp. 1244–1246, 2000.

[111] R. Weis and T. Gaylord, "Lithium niobate: summary of physical properties and crystal structure," *Applied Physics A: Materials Science & Processing*, vol. 37, no. 4, pp. 191–203, 1985.

[112] J. Hebling, K.-L. Yeh, M. C. Hoffmann, B. Bartal, and K. A. Nelson, "Generation of high-power terahertz pulses by tilted-pulse-front excitation and their application possibilities," *JOSA B*, vol. 25, no. 7, pp. B6–B19, 2008.

[113] H. Ishizuki and T. Taira, "Half-joule output optical-parametric oscillation by using 10-mm-thick periodically poled mg-doped congruent $LiNbO_3$," *Opt. Express*, vol. 20, no. 18, pp. 20 002–20 010, 2012.

[114] K. Ravi *et al.*, "Theory of terahertz generation by optical rectification," Ph.D. dissertation, Massachusetts Institute of Technology, 2014.

[115] J. Williamson, "Low-storage runge-kutta schemes," *Journal of Computational Physics*, vol. 35, no. 1, pp. 48–56,55, 1980.

[116] A. Siegman, "Quasi fast Hankel transform," *Opt. Lett.*, vol. 1, no. 1, pp. 13–15, 1977.

[117] M. Cree and P. Bones, "Algorithms to numerically evaluate the Hankel transform," *Computers & Mathematics with Applications*, vol. 26, no. 1, pp. 1–12, 1993.

[118] G. R. Hadley, "Transparent boundary condition for the beam propagation method," *IEEE Journal of Quantum Electronics*, vol. 28, no. 1, pp. 363–370, 1992.

[119] K. M. Mørken, "Chapter 5: Computer arithmetic and round-off errors," 2010. [Online]. Available: https://www.uio.no/studier/emner/matnat/math/MAT-INF1100/h10/kompendiet/kap5.pdf

[120] "Round-off/truncation errors & numerical cancellation," 2003. [Online]. Available: http://home.iitk.ac.in/~pranab/ESO208/rajesh/03-04/Errors.pdf

[121] R. DeSalvo, A. A. Said, D. J. Hagan, E. W. Van Stryland, and M. Sheik-Bahae, "Infrared to ultraviolet measurements of two-photon absorption and n_2 in wide bandgap solids," *IEEE J. Quantum Electron*, vol. 32, no. 8, pp. 1324–1333, 1996.

[122] X. Wu, C. Zhou, W. R. Huang, F. Ahr, and F. X. Kärtner, "Temperature dependent refractive index and absorption coefficient of congruent lithium niobate crystals in the terahertz range," *Optics express*, vol. 23, no. 23, pp. 29 729–29 737, 2015.

[123] D. H. Jundt, "Temperature-dependent sellmeier equation for the index of refraction, n e, in congruent lithium niobate," *Opt. Lett.*, vol. 22, no. 20, pp. 1553–1555, 1997.

[124] A. Parent, M. Morin, and P. Lavigne, "Propagation of super-gaussian field distributions," *Optical and quantum electronics*, vol. 24, no. 9, pp. S1071–S1079, 1992.

[125] A. Chafiq, Z. Hricha, and A. Belafhal, "Flat-topped mathieu-gauss beam and its transformation by paraxial optical systems," *Optics communications*, vol. 278, no. 1, pp. 142–146, 2007.

[126] C.-W. Chen, Y.-S. Lin, J. Y. Huang, C.-S. Chang, C.-L. Pan, L. Yan, and C.-K. Lee, "Generation and spectral manipulation of coherent terahertz radiation with two-stage optical rectification," *Opt. Express*, vol. 16, no. 18, pp. 14 294–14 303, 2008.

[127] F. Kärtner, N. Matuschek, T. Schibli, U. Keller, H. Haus, C. Heine, R. Morf, V. Scheuer, M. Tilsch, and T. Tschudi, "Design and fabrication of double-chirped mirrors," *Opt. Lett.*, vol. 22, no. 11, pp. 831–833, 1997.

[128] K. Kawase, M. Sato, K. Nakamura, T. Taniuchi, and H. Ito, "Unidirectional radiation of widely tunable THz wave using a prism coupler under noncollinear phase matching condition," *Appl. Phys. Lett*, vol. 71, no. 6, pp. 753–755, 1997.

[129] M. Naftaly and R. E. Miles, "Terahertz time-domain spectroscopy for material characterization," *Proceedings of the IEEE*, vol. 95, no. 8, pp. 1658–1665, 2007.

[130] D. Grischkowsky, S. Keiding, M. Van Exter, and C. Fattinger, "Far-infrared time-domain spectroscopy with terahertz beams of dielectrics and semiconductors," *JOSA B*, vol. 7, no. 10, pp. 2006–2015, 1990.

[131] G. Ghosh, “Dispersion-equation coefficients for the refractive index and birefringence of calcite and quartz crystals,” *Opt. Commun*, vol. 163, no. 1, pp. 95–102, 1999.

[132] J. W. Goodman, *Introduction to Fourier optics*. Roberts and Company Publishers, 2005.

[133] N. I. Landy and W. J. Padilla, “Guiding light with conformal transformations,” *Opt. Express*, vol. 17, no. 17, pp. 14 872–14 879, 2009.

[134] M. Gupta, “Power combining efficiency and its optimisation,” in *IEE Proceedings H (Microwaves, Antennas and Propagation)*, vol. 139, no. 3. IET, 1992, pp. 233–238.

[135] W. Tian, L. Wang, O. Halil, and et.al., “Efficient multi-cycle terahertz generation based on a multi-lines source,” in proceeding.

[136] A. Weling, B. Hu, N. Froberg, and D. Auston, “Generation of tunable narrow-band thz radiation from large aperture photoconducting antennas,” *Applied physics letters*, vol. 64, no. 2, pp. 137–139, 1994.

[137] J. McMullen, “Chirped-pulse compression in strongly dispersive media,” *JOSA*, vol. 67, no. 11, pp. 1575–1578, 1977.

[138] R. V. Aguilar, A. Stier, W. Liu, L. Bilbro, D. George, N. Bansal, L. Wu, J. Cerne, A. Markelz, S. Oh *et al.*, “Terahertz response and colossal kerr rotation from the surface states of the topological insulator bi 2 se 3,” *Physical review letters*, vol. 108, no. 8, p. 087403, 2012.

[139] J. Hebling, A. Stepanov, G. Almási, B. Bartal, and J. Kuhl, “Tunable thz pulse generation by optical rectification of ultrashort laser pulses with tilted pulse fronts,” *Applied Physics B*, vol. 78, no. 5, pp. 593–599, 2004.

[140] E. Liang, Y. Liang, Y. Zhao, J. Liu, and Y. Jiang, “Low-frequency phonon modes and negative thermal expansion in a (mo4) 2 (a= zr, hf and m= w, mo) by raman and terahertz time-domain spectroscopy,” *The Journal of Physical Chemistry A*, vol. 112, no. 49, pp. 12 582–12 587, 2008.

[141] Y. Avetisyan, A. Makaryan, V. Tadevosyan, and M. Tonouchi, “Design of a multistep phase mask for high-energy terahertz pulse generation by optical

rectification," *Journal of Infrared, Millimeter, and Terahertz Waves*, vol. 38, no. 12, pp. 1439–1447, 2017.

[142] L. Pálfalvi, J. Fülöp, G. Almási, and J. Hebling, "Novel setups for extremely high power single-cycle terahertz pulse generation by optical rectification," *Applied Physics Letters*, vol. 92, no. 17, p. 171107, 2008.

[143] T. Hammond, "Spatio–temporal coupling to create sub-femtosecond pulses," *Journal of Optics*, vol. 19, no. 11, p. 114002, 2017.

[144] R. Datta, C. Munson, M. Niemack, J. McMahon, J. Britton, E. J. Wollack, J. Beall, M. Devlin, J. Fowler, P. Gallardo *et al.*, "Large-aperture wide-bandwidth antireflection-coated silicon lenses for millimeter wavelengths," *Applied optics*, vol. 52, no. 36, pp. 8747–8758, 2013.

[145] H.-T. Chen, J. Zhou, J. F. O'Hara, and A. J. Taylor, "A numerical investigation of metamaterial antireflection coatings," *Int. J. Terahertz Sci. Technol*, vol. 3, no. 2, pp. 66–73, 2010.

[146] J. F. Federici, B. Schulkin, F. Huang, D. Gary, R. Barat, F. Oliveira, and D. Zimdars, "Thz imaging and sensing for security applications—explosives, weapons and drugs," *Semiconductor Science and Technology*, vol. 20, no. 7, p. S266, 2005.

[147] G. Boyd and M. Pollack, "Microwave nonlinearities in anisotropic dielectrics and their relation to optical and electro-optical nonlinearities," *Physical Review B*, vol. 7, no. 12, p. 5345, 1973.

[148] K. Ravi, W. R. Huang, S. Carbajo, X. Wu, and F. Kärtner, "Limitations to thz generation by optical rectification using tilted pulse fronts," *Optics express*, vol. 22, no. 17, pp. 20 239–20 251, 2014.

[149] L. E. Myers and W. R. Bosenberg, "Periodically poled lithium niobate and quasi-phase-matched optical parametric oscillators," *IEEE Journal of Quantum Electronics*, vol. 33, no. 10, pp. 1663–1672, 1997.

[150] J.-P. Meyn and M. Fejer, "Tunable ultraviolet radiation by second-harmonic generation in periodically poled lithium tantalate," *Optics letters*, vol. 22, no. 16, pp. 1214–1216, 1997.

[151] P. Hertel, "Dielectric waveguides," Sep,2009, accessed:2017-7-20. [Online]. Available: http://www.home.uni-osnabrueck.de/phertel/aps/Dielectric_Waveguides.pdf

[152] "Chapter 3 heat conduction in cylindrical and spherical coordinates," http://www.ewp.rpi.edu/hartford/~ernesto/S2006/CHT/Notes/ch03.pdf, accessed: 2017-02-2.

[153] M. Niemz, "Threshold dependence of laser-induced optical breakdown on pulse duration," *Applied physics letters*, vol. 66, no. 10, pp. 1181–1183, 1995.

[154] L. Yu, M. Huang, M. Chen, W. Chen, W. Huang, and Z. Zhu, "Quasi-discrete Hankel transform," *Opt. Lett.*, vol. 23, no. 6, pp. 409–411, 1998.

[155] XFEL, "Properties of the x-ray laser flashes," 2017, [Online; accessed 18-04-2018]. [Online]. Available: https://www.xfel.eu/facility/overview/facts_amp_figures/index_eng.html

[156] ——, "Fxe instrument parameters for early user operation," 2017, [Online; accessed 18-04-2018]. [Online]. Available: https://www.xfel.eu/sites/sites_custom/site_xfel/content/e35165/e46561/e46879/e60140/e60141/xfel_file60142/FXE_specs_2017-10-10_eng.pdf

[157] LCLS, "Lcls parameters – update december 2017 — general sase parametersa," 2017, [Online; accessed 18-04-2018]. [Online]. Available: https://portal.slac.stanford.edu/sites/lclscore_public/Accelerator_Physics_Published_Documents/LCLS-parameters-3-22-17.pdf

[158] M. C. Kemp, "Millimetre wave and terahertz technology for detection of concealed threats-a review," in *Infrared and Millimeter Waves, 2007 and the 2007 15th International Conference on Terahertz Electronics. IRMMW-THz. Joint 32nd International Conference on.* IEEE, 2007, pp. 647–648.

[159] J.-H. Jeong, B.-J. Kang, J.-S. Kim, M. Jazbinsek, S.-H. Lee, S.-C. Lee, I.-H. Baek, H. Yun, J. Kim, Y. S. Lee *et al.*, "High-power broadband organic THz generator," *Scientific reports*, vol. 3, p. 3200, 2013.

[160] C. Weiss, G. Torosyan, Y. Avetisyan, and R. Beigang, “Generation of tunable narrow-band surface-emitted terahertz radiation in periodically poled lithium niobate,” *Opt. Lett.*, vol. 26, no. 8, pp. 563–565, 2001.

[161] Wikipedia contributors, “Terahertz radiation — Wikipedia, the free encyclopedia,” 2018, [Online; accessed 11-April-2018]. [Online]. Available: https://en.wikipedia.org/w/index.php?title=Terahertz_radiation&oldid=828150221

[162] U. Schwarz and M. Maier, “Asymmetric raman lines caused by an anharmonic lattice potential in lithium niobate,” *Physical Review B*, vol. 55, no. 17, p. 11041, 1997.